Microscopical and Sub-microscopical Characterization of a Heavy Plate made of a Micro-alloyed HSLA Steel

Peter Felfer

September 29, 2008

Affidavit

I declare in lieu of oath that I wrote this thesis and performed the associated research myself, using only literature cited in this volume.

Peter Felfer, Leoben September 2008

Acknowledgements

First of all, I want to express my gratidute to Dr. Harald Leitner for his scientific guidance and helpful advice. Moreover, I want to gratefully express my thanks for giving me the freedom and support to realize my own ideas. This also applies for Dr. Rainer Grill and Rupert Egger of voestalpine, who gave me a free hand to an extent that is exceptional for an industrial partner.

In equal measure, I want to thank the PhD students, especially Michael Schober, Ronald Schnitzer and Erich Stergar for their support during the atom probe measurements, their unfiltered honest and critical assessment and many fruitful discussions.

My sincerest gratitude is to Dr. Krysztina Spiradek and her group at ARC Seibersdorf, who did excellent work on the TEM and gave me the chance to try out new techniques, using their FIB system. Special thanks for the sample preparation also go to Mr. Wolfgang Phillip Thomma of the Erich Schmidt Institute, god of the ion beam, in spite of the fact that he burned me unprovoked.

Last but not least of the people directly involved in this work, I want to thank my father for helping me fabricating all the equipment necessary. We spent endless hours in front of the CNC milling machine, but it was worth the effort.

My personal appreciation is to my family who always supportet me, particularly my sister, being my personal psychologist and my mother for always

supporting me a bit more. Further I want to thank my friends who always overlooked if I could not stop talking about atoms or other strange things nobody is interrested in. Thanks to my best friend Robert Wolf for digging me out of avalanches occasionally, without that this work would not have been possible either.

Contents

3DAP	3 Dimensional Atom Probe
BF	Bright Field
CCT	Continuos Cooling Transformation
CVN	Charpy V-Notch
DBTT	Ductile to Brittle Transition Temperature
DF	Dark Field
DIC	Direct Intense Cooling
ED	Electron Diffraction
EDX	Energy Dispersive X-ray detection
FEG	Field Emission Gun
FIM	Field Ion Microscope
FWHM	Full Width Half Maximum
GB	Grain Boundary
HFP	HF in Peroxide
HRTEM	High Resolution Transmission Electron Microscope
HSLA	High Strength Low Alloy
L	Longitudinal
LEAP	Local Electrode Atom Probe
LM	Light Microscope
MA	Martensitic Austenitic
N	Normalized
PaA	Pancaked - Annealed
PaQ	Pancaked - Quenched
PoA	Polygonal - Annealed
PoQ	Polygonal - Quenched
PTT	Precipitation Time Temperature
SAD	Selected Area Diffraction
SEM	Scanning Electron Microscope
SIM	Scanning Ion Microscope
T	Transverse
TEM	Transmission Electron Microscope
TTT	Time Temperature Transformation
UTS	Ultimate Tensile Strength
XRD	X-Ray Diffraction
YR	Yield Ratio
YS	Yield Strength
ZV	Tensile Test

Table 1: Used Abbreviations

Abstract

In this diploma thesis, the microstructure and the atomic assembly of a micro-alloyed HSLA trial heavy plate has been investigated and related to the materials mechanical properties. This has been conducted in thermo-mechanical rolling condition and four additional heat treatment conditions. The aim was to find the influence of austenite conditioning ("pancaking"), annealing (precipitation hardening, etc.) and "normalizing" (slow air cooling) on the materials properties and microstructure.

The micro- and sub-micro structures have been investigated using optical microscopy (LM), electron microscopy (SEM, TEM, HRTEM) and atom probe analysis (3DAP). An etchant that is suitable for distinguishing the individual constituents in the optical microscope has been found. Atom probe analysis revealed the local enrichment and general distribution of the chemical elements in shipping condition. The behavior of various elements during annealing has been investigated.

The evolution of precipitations during annealing has been traced by X-ray diffraction (XRD).

The chemical composition of the middle segregation zone has been studied using a laser assisted local electrode atom probe (LEAP), a method for site-specific preparation in steel materials has been developed for this purpose.

The measured mechanical properties have been compared to the corresponding values, calculated based on microstructural features.

Keywords: HSLA; heavy plate; micro-alloy; electron microscopy; atom probe; phase characterization; segregation; precipitation; vanadium carbide; separations; middle segregation; site-specific sample preparation; local electrode atom probe;

Zusammenfassung

In der vorliegenden Diplomarbeit wurde die Mikrostruktur eines mikrolegierten HSLA Versuchs-Grobblechs und dessen Struktur bis hin zur atomaren Größenordnung untersucht und mit den mechanischen Kennwerten verglichen. Dies wurde im thermo-mechanisch behandelten Zustand und vier weiteren Vergleichzuständen durchgeführt um die Auswirkungen von Austenitverformung ("pancaking"), Anlassen (Ausscheidungsvorgänge, etc.) und "Normalisieren" (Abkühlung an Luft) zu beschreiben.

Die Mikro- und Submikrostrukturen wurden mit Hilfe von Lichtmikroskop (LM), Elektronenmikroskop (SEM, TEM, HRTEM) und Atomsonde (3DAP) charakterisiert. Ein Ätzverfahren zur Kontrastierung der Gefügebestandteile im Lichtmikroskop wurde ermittelt. Mittels Atomsonde wurde die örtliche Anreicherung von Bor im Lieferzustand gemessen und die Verteilung der weiteren Elemente bestimmt. Die lokale Anreicherung verschiedener Elemente während des Anlassens wurde ebenfalls beobachtet.

Die Entwicklung von Ausscheidungen mit der Anlasstemperatur wurde mit Hilfe von Röntgenbeugung (XRD) verfolgt.

Die chemische Zusammensetzung der Mittenseigerungszone wurde mittels Laserunterstützter Lokalelektrodenatomsonde (LEAP) gemessen, eine Methode zur Zielpräparation von Atomsondenproben wurde zu diesem Zweck entwickelt.

Die gemessenen mechanischen Kennwerte wurden mit Werten, berechnet aus der Mikrostruktur, verglichen.

Schlagwörter: HSLA; Grobblech; mikrolegieren; Elektronenmikroskopie; Atomsonde; Phasencharakterisierung; Seigerung; Ausscheidungen; Vanadiumkarbid; Separations; Mittenseigerung; Zielpräparation Atomsonde; Lokalelektrodenatomsonde;

Chapter 1

Introduction

1.1 Technical Motivation

In the past, the development of microalloyed heavy plates has been relying mainly on experience and laboratory trials. The stage of development has already become very sophisticated, using these empirical methods. Yield strengths of 1000MPa have already been achieved at fracture elongations of up to 15%. Whatsoever, methods based on variation of processing parameters and chemical composition can just give hints of the mechanisms behind. It is therefore essential to get an insight of the events in the material that are the origin of the materials properties, in order to further push the envelope. With modern techniques in materials science, such as TEM and the atom probe, it is possible to trace the materials constitution down to the atomic level and so answer questions that have been discussed in the literature since these materials have been around.

These empirically developed materials further give extraordinary challenges to the developer, since plenty of structures from the macro to the atomic scale are present, where a lot of the interactions and effects are not understood to the present day. It can not be assumed that all effects will

be fully investigated ever, but by the advent of more and more sophisticated characterization methods we face a quite exciting coming time.

In the case of the investigated trial plate of voestalpine, the topics of interest were the identification of the individual phases and their distribution in the material, the change due to heat treatments and the impact on the mechanical properties.

1.2 Economic Motivation

Behind every technical question that is asked, should stand an economic one. Heavy plates are widely used for bridges, cranes and pipelines, where the challenge has always been the development of higher-strength, better-toughness plates, still maintaining weldability, while the cost, driven by the alloying elements has to be kept low. This gives the task to the technician, to design a material, that is as low in carbon (weldability) and alloying elements (price) as possible. Using modern scientific methods it is possible to directly observe the effect of different elements and treatments to the steel, enabling the developer to judge, weather an alloying element can be added, removed or replaced by a more cost-effective one.

For voestalpine, heavy plates represent 12% of the total sales (in metric to), leading to a turnover of 800Mio EUR. This shows the immense impact, even small steps forward have. These steels are also processed within the voestalpine group, further adding to the turnover. So, heavy plates are one of the backbones of the company, being also a strategic material within a steel group, since they do not demand complicated cold rolling plants or coating production lines.

1.3 Conceptual Formulation of the Tasks

Investigation of a high-tensile carbon steel, minimum yield strength of 960MPa, with lowered carbon-equivalent and particular low carbon content, in different material and heat treatment conditions, by various metallographic methods. Measurement of correlations between structural parameters (e.g. precipitation state) and mechanical - technological parameters. The confidential information and results that are exchanged in the course of the thesis, as well as the exchanged information beyond it that are in relation to new developments underlay secrecy.

1.4 Concept of a Micro-alloyed HSLA heavy plate

The classical approach to deliver structural steels with a tensile strength as high as possible has always been the addition of C and alloying elements, mainly Mn. Since this is limited by the weldability of structural steels, that can not be guaranteed above a C content of 0,2% or a carbon equivalent CEV of 0,82 (as stated in DIN EN 10025 for the class S960Q), the steel companies have started to search other possibility to raise the strength of the structural steels as early as in the 1960s, to still maintain weldability [BdH83]. Basically, the main increase in strength has been achieved in the 1970s and 1980s, but modern metallurgical possibilities and advanced process routes still push the envelope. Especially, better inclusion control has led to good low-temperature toughness and high fracture elongations.

It has been found that there are alloying elements that are as effective as C, in hardening steel materials, when given in combination with a thermo-mechanical treatment (fig. 1.1). This has made it possible to raise the yield strength of structural steels from 500MPa in the late 70s to around 1000MPa

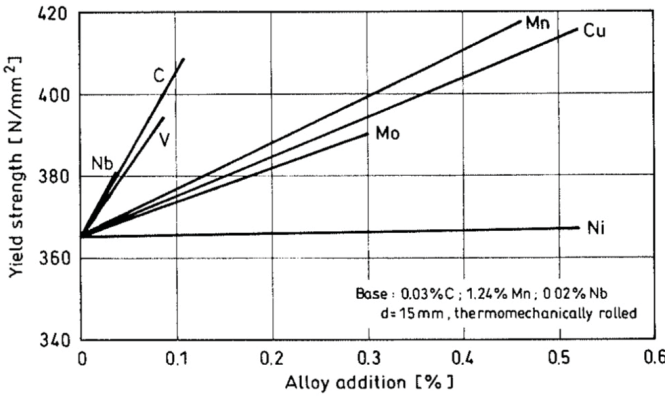

Figure 1.1: Influence of alloy addition on yield strength of thermomechanically rolled steels [KDMS92].

and above nowadays.

The process route for microalloyed heavy plates begins with the setting of the chemical composition in the steel plant. To combine high strength with high toughness it is essential to reduce the content of S, N and P by degassing, basically, to deliver a steel that is as clean as possible at a reasonable cost level. Further, the segregation of the microalloying elements has to be kept low, depleted zones are detrimental.

After the block storage, the slabs are reheated in a pusher type furnace, the rolling begins at a temperature of around 1000°C, where a fine austenite structure is obtained by recrystallization, down to a specific reduction. The plate is then air cooled down to a temperature as low as 850°C - 780°C, where the rolling is finished. Schematically, this is shown in fig. 1.2, TM stands for thermomechanic rolling. The benefit is, that during cooling, and during rolling, fine (Ti,Nb)(C,N) are precipitated inside the material, that pin the structure to some extent, inhibiting recrystallization and grain growth. This is called austenite conditioning or simply pancaking. This

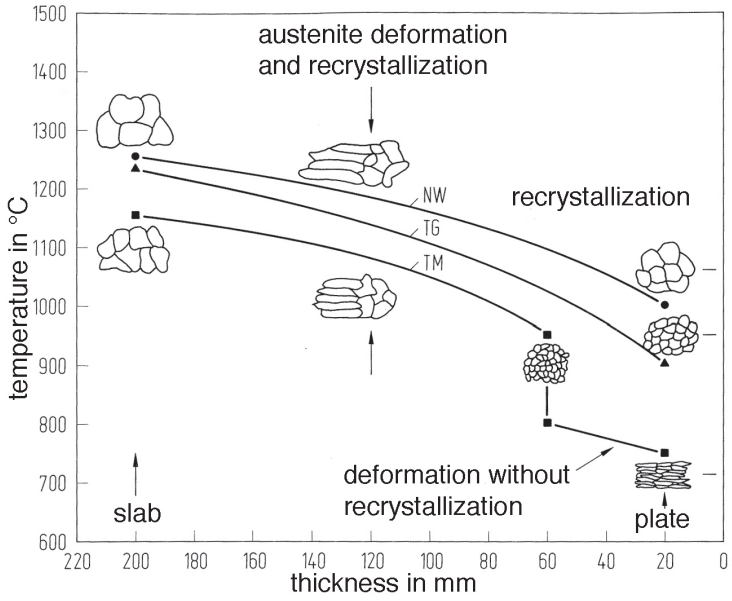

Figure 1.2: Influence of rolling on the grain size of heavy plates (normalizing (NW), temperature controlled (TG) and thermo-mechanical (TM) [BdH83].

heavily deformed, fine austenite is then transformed into a ferritic/pearlitic or bainitic/martensitic structure. The latter giving the higher strength. For highest strength, the heavy plates are also alloyed with elements that form precipitates at lower temperatures, to provide precipitation hardening. This is quite similar to the process of secondary hardening, that is observed in tool steels. Such elements can be V or Mo, that have widely been in use for decades, while Cu hardened steels have established in the mid 80's.

Chapter 2

Theoretical Background

2.1 Strengthening Mechanisms in Steels

To identify the mechanisms that provide the strength to the steel, we first have to say what is defined as "failure" for the material in question. In the case of structural steels, the material has failed if it fractures, or if undesired deformations occur as a response to applied tensions. Fig. 2.1 shows the relation between the elongation of a metallic sample and the applied tension.

Usually for technical and measurement reasons, a plastic deformation over 0,2% is defined as undesired, the tension where this is reached is called $R_{P0,2}$ or yield strength YS. Lower plastic deformations are very difficult to measure, the ideal proportional tension R_P would be at a point, where not a single grain has experienced deformation. Plastic deformation is the failure mode at room temperature. If we go lower in temperature, steels (and other metals with bcc lattice) show the phenomenon that they do not show plastic deformation before they fracture. This entails that virtually no work is required to fracture the metal.

$$\sigma = C \cdot \varphi^n \tag{2.1}$$

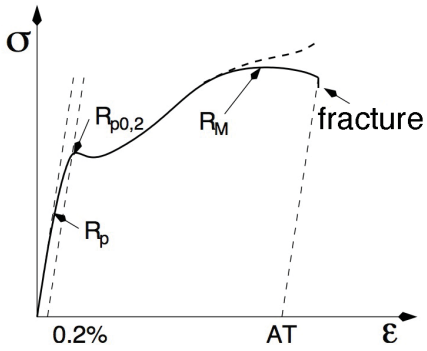

Figure 2.1: Schematic stress strain curve with yield point, after [SF]

For a lot of metals, the stress - strain relation can phenomenologically be described by Ludwiks equation (2.1), where C is a constant, and n is the work hardening exponent. The true strain φ is defined as the natural logarithm of the ratio between the original and the deformed dimension ($\varphi = ln(l/l_0)$).

2.1.1 Plasticity in Steels caused by Dislocation Movement

The plasticity of metals and a lot of other crystalline materials can at ambient temperature be referred to the behavior of specific crystal defects in the steel. If a (poly)crystalline material wants to deform, usually "line - defects", called dislocations, must be moved within the material. From an atomic scaled point of view, a dislocation is an additional crystallographic half-plane, inserted into a crystal lattice, as schematically displayed in fig. 2.2. What defines the properties of the dislocation is not the insertion of the half-plane itself, it is in fact the stress field that is present at the end of the inserted half-plane. If the deformation is said to be macroscopic, these defects have to propagate all through the material.

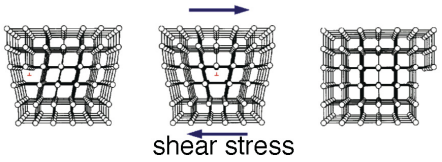

Figure 2.2: Sketch of a dislocation in a crystal lattice, moving by shear stress [Kie08].

Dislocation Interactions

In an ideal crystal, a dislocation just has to overcome the potential between two positions, where every position is equally stable divided by a vector called b (burgers vector). A metal with low defect density starts to plastically deform at very low stresses. An α-iron single-crystal with very low dislocation density would start to deform at a lattice friction stress of $65MPa$ [TP86].

If there are other defects in the material, the dislocation interacts with the defects resulting in retracting forces to the motion. These defects can be point defects, line defects, interfaces or defects with spatial expansion. Responsible for this is the stress field that defines a dislocation. It sums up with the stress field around the defect, resulting in attracting or repulsing forces, both hindering the motion of the dislocation. It is so possible, to raise the stress, necessary to deform a metal to much higher values. Since for structural steels, this is the "yield" we get out of the material, this stress is called yield stress (YS). The highest value that theoretically can be achieved is the so-called theoretical strength, which is the value, where whole crystallographic planes would start to slip against each other. This can be measured in thin fiber crystals, that are too small that dislocations can form inside.

The excess energy above the thermal energy that is input by stress to the dislocations becomes manifest in the dislocations curvature. This is because a dislocation has an energy that is largely defined by its length. So it behaves

somewhat like a tiny rubberband. The different (continuously distributed) energy states caused by constitutional fluctuations are present in the dislocation, with a spatial and time density distribution following the equipartition theorem (equ. 2.2), where H is the Hamilton function of the system and p_i are the individual generalized momenta and q_i the generalized coordinates (referring to the energy states of the dislocation) in phase space.

$$< \frac{\partial H}{\partial p(q)_i} \cdot p(q)_i >= kT \tag{2.2}$$

The energy per length of a dislocation is $\approx 0,5Gb^2$, where the shear modulus G of ferrite is $8,03 \cdot 10^4 MPa$ with a burgers vector of $0,25nm$ [TP86]. Fluctuations in the dislocation's constitution, that are of the order of kT are for bcc crystals the ease of the overcome of the lattice friction stress and the introduction of dislocation splitting, according to the stacking fault energy that is rather high in bcc crystals. The ductile to brittle transition temperature (DBTT) for example, is caused by the immobilization of screw dislocations by splitting that has to be overcome by thermal activation.

2.1.2 Solid Solution Strengthening (Point Defects)

Solid solution strengthening is caused by the occurrence of stress fields around point defects in crystalline materials. This retracts the motion of the dislocations. This can be foreign atoms or vacancies, the lack of an atom on a lattice position. The effect of an element is higher, the higher the misfit to the lattice resulting in a larger strain field. The class of foreign atoms further subdivides into atoms that lie on lattice positions (substitutional) or those who lie in between (interstitial).

Around substitutional point defects we find stress fields that have spherical symmetry. This also means that they have no shear strain around them. Thus the interaction between this defects and the dislocation goes down to

zero, if the dislocation is a screw dislocation. The stress field around interstitial atoms in bcc iron has no spherical symmetry. This is the reason why the effect of interstitial elements is much higher than the one of substitutional elements. Interstitial elements of importance for steels are C and N.

In general, the effect of point defects is described by Fleischer‘s equation (equ. 2.3, [Fle63]), where c is the concentration of the foreign atom in atomic percent and n is an exponent.

$$\Delta\sigma \propto c^n \tag{2.3}$$

If the average inter-distance of the foreign atom sets the effect, n is 1/2, or $\Delta\sigma \propto \sqrt{c}$. This is a good approach if the concentration of the defect is low, as it is for a lot of materials. Low means that the strain fields around the defects do not interact significantly, or chemically spoken, the concentration equals the activity.

2.1.3 Precipitate/Dispersion Strengthening (Point - like Defects)

The effect of precipitates is locally quite similar to the one of point defects. The difference is that it is not a single atom that inhibits the motion, but fine distributed second phases. If the precipitation is ”small” the dislocation feels resistance but is able to pass through the particle, if it is bigger, the dislocation has to circumvent. The maximum drag per particle is obtained if the tension necessary is equal for both mechanisms. The particle inter-distance then defines the total strengthening, manifest in the volume fraction of the particle forming phase.

The main difference to solute strengthening is that the angle the dislocation forms around a single obstacle is much higher, as the object is much bigger. It can be so high that the dislocation interacts with itself (circumventing). This is the reason why the strengthening by an object that forms

low angle dislocation distortions and one that forms a high angle distortion can not be summed up linearly.

If the particles are circumvented, the raise in strength is given by equ. 2.4, meaning the effect decreases at constant volume fraction by $1/r_p$. In equ. 2.4 [Got04] k is a constant, G is the shear modulus of the precipitation, b the burgers vector of the dislocation, f the volume fraction and r_p is the particles radius.

$$\Delta\sigma = kGb\frac{\sqrt{f}}{r_p} \tag{2.4}$$

For cutting, the expression that gives the raise in yield strength is equ. 2.5 [Got04], where α is a numerical constant and γ_s is the interfacial energy. Hence, at a constant volume, the effect grows with particle size by $\sqrt{r_p}$. Equ. 2.5 implies that the particle interdistance is much higher than the particle size.

$$\Delta\sigma = \frac{\alpha}{G \cdot b^2}\gamma_s^{3/2}\sqrt{r_p f} \tag{2.5}$$

If this is the case, the cutting eases the passing of following dislocations through the precipitation. As a result, the metal does not follow Ludwik‘s equation any more, it shows a plateau after the plastic deformation starts.

2.1.4 Work Hardening (Line Defects)

Dislocations are also hindered in their motion by other dislocations, the amount of the retraction is again defined by the distance between the obstacles. It is important to mention that the resulting burgers vector of the point of intersection depends on the burgers vectors of the individual dislocations, sometimes resulting in immobile burgers vectors. Since all the different possible reactions can be referred to as sampled equally at different dislocation densities in thick materials, just the inter-distance can be taken to express the raise in yield strength, what results in equ. 2.6. Here, K_{WH}

is the work-hardening constant and ρ is the dislocation density.

$$\Delta\sigma = K_{WH} \cdot \sqrt{\rho} \tag{2.6}$$

The reason why it is called work hardening is that that during plastic deformation the amount of dislocations in the metal goes up by magnitudes, meaning this effect gets more dominant the more we deform the metal. The effect is of course the same, if the dislocation density has been obtained by some other mechanism.

Martensitic and bainitic transformations can also result in high dislocation densities in the material, since the misfit of the shear deformation has to be compensated by plastic deformation.

2.1.5 Strengthening via Grain Refinement (Interfaces)

If dislocations meet an interface in a polycrystalline material, they can get piled up, if the grain size is large enough. If the dislocations cannot overcome the tension necessary to activate dislocation sources in the next grain and only macroscopic deformations are interesting, this causes an excess tension that adds to the other terms giving the yield strength. The effect is higher the more interfaces we have and the more stable the interface is. This is expressed in the Hall - Petch relation [Pet53] (equ. 2.7), where K_y is the grain boundary drag and d is the grain size. This is the most important model for grain boundary drag with dislocation pile ups.

$$\Delta\sigma = K_y \cdot d^{-1/2} \tag{2.7}$$

The stronger dependence is the case of iron is the one on the grain size d.

The contribution of each interface is regarded in the constant K_y, the grain boundary drag. It is largely modified by the interface‘s chemistry and

the occurrence of grain boundary films. The Hall - Petch ansatz for the grain boundary drag mainly takes the crystallographic properties of the grain into account, leading to the equation 2.8, where σ_c is the critical tension, where the grain boundary drag is overcome, if r is the distance to the neighboring dislocation source.

$$K_y = \sigma_c \cdot \sqrt{r} \tag{2.8}$$

This still leaves the atomic origin of the drag unknown. An approach that takes the local chemistry into account is the one by Gouzou [Gou64]. Gouzou relates the grain boundary drag to the local occurrence of solute atoms, in particular C, N and B. They are said to retract dislocations, present at the grain boundary, from being emitted into the grain.

$$K_y = \frac{1,244}{\eta \cdot b \cdot \sin 2\Theta} \cdot \sum_{i=B,C,N} w_i \cdot \sqrt{c_i} \tag{2.9}$$

This gives equation 2.9 . The first term‘s denominator gives the sample‘s elongation per dislocation step, if a dislocation of length d moves a distance of η d with an angle of Θ with respect to the direction of the tension. The length of each dislocation step is given by the Burgers vector b. The second one sums up the effect of the individual elements, in particular B, C and N, w_i is the work per atom to overcome the drag and c_i the atomic density. For Bainitic laths with carbon on the interface, this is probably the better expression to describe the grain boundary strengthening, if segregations are present.

As the structures get finer and finer, some of the mechanisms that usually define the behavior of the dislocations, can not take place within the material. For steels, it has been observed that, if the structural size goes below $1\mu m$ and the grain boundaries are sufficiently strong, the yield stress goes with the inverse of the grain size, $\sigma_y \propto 1/d$. This is the so-called Langford -

Cohen relation [LC69]. It states that, since the grain size is very small, the probability to find a dislocation source in the neighboring grain is very small. Yielding is then determined by the stress necessary to expand a dislocation loop across a slip plane. This model has successfully been applied to bainitic and martensitic structures as well as heavily cold-deformed iron [Bha01].

The beneficial thing about the grain refinement is that it not only raises the yield strength, but also increases the toughness. The reason for that is that the probability to find a grain with a slip system that can be activated in the vicinity is much higher in fine grained than in coarse grained microstructures. So the need for plastic accommodation in the material are smaller, once the grain boundary drag is overcome. This does not apply any more, if the grain size is below a certain value, because the dislocations get trapped at the interfaces and no work hardening is possible any more [Bha08]. The subsequent plastic instability leads to very low fracture elongations [TM02].

2.1.6 Strengthening by the Presence of a Second Phase (3 - Dimensional Defects)

Models that want to predict the total strength from the strength of individual phases are often already continuum mechanical models. In the easiest form it is just a linear combination of the individual strengths. This makes sense if there are just negligible residual micro-stresses. But this already disregards elastic constraints.

Ultimately, the reason for raise in yield strength by a second phase are the constraints the stronger phase sets to the weaker one. This is similar to why it is possible to build strong joints with glues that are as a bulk material much weaker than the material to join together [YB94]. From this theory, equ. 2.10 can be derived. It gives the raise in yield strength of the weaker phase $\sigma_{B'}$ from its stand-alone strength σ_B over its volume fraction

V_B, provided by a hard second phase with a strength of σ_M.

$$\sigma_{B\prime} \approx \sigma_B(0,65e^{-3,3V_B} + 0,98) \leqslant \sigma_M \tag{2.10}$$

In principle, this effect is bigger, the thinner the weaker material is. Thus, equ. 2.10 does not strictly apply any more, if there are two different constituents of the harder phase.

For technical materials, the situation is unfortunately very complex, since the individual phases or constituents do not just interact with their mechanical properties, they also interact during the evolution of the microstructure. For lower bainite/martensite mixtures, this has been investigated by Young et al. [YB94]. They found that there is a maximum in yield strength at a bainitic volume fraction of $\approx 0,3$ (fig. 2.3). The maximum is located, where the strength of the martensite, that is enriched in carbon by the presence of bainite, equals the strength of the constrained bainite.

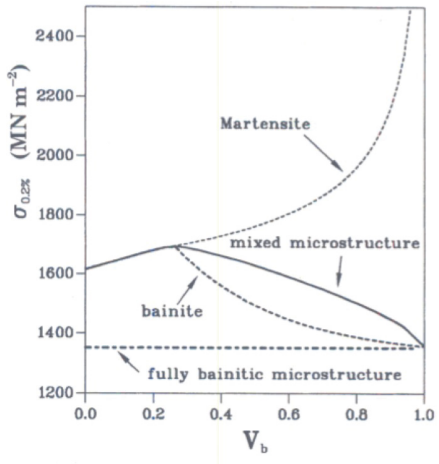

Figure 2.3: Illustration of contribution of martensite/lower bainite volume fraction to mixture strength [YB94]

2.1.7 An Ansatz for the Strength of Bainite and Martensite

Linearly combining the individual contributions, an equation, like in the form published by Bhadeshia [Bha01], valid for bainite, is obtained (equ. 2.11). Here, σ_{Fe} is the strength of pure annealed iron, σ_{ss}^{i} is the solid solution strengthening by the substitutional element i, σ_C is the strengthening by C in solid solution and k_ϵ is the lath boundary drag ($115MPa/m$ after [Bha01]). The dislocation's mean free path $\bar{L_3}$ is twice the lath thickness, k_p ($0,52V_\Theta MPa/m$, where V_Θ is the cementite volume fraction, after [DGN82]) is the constant that reflects the contribution of the cementite particles with interdistance Δ. The dislocation hardening is described by the constant C_{10} ($\approx 7,34MPa$ after [KW63]) times the square root of the dislocation density ρ_d.

$$\sigma = \sigma_{Fe} + \sum_i \sigma_{ss}^{i} + \sigma_C + k_\epsilon \cdot (\bar{L_3})^{-1} + k_p \cdot \Delta^{-1} + C_{10} \cdot \sqrt{\rho_d} \qquad (2.11)$$

Here, the Langford-Cohen relation is used to describe the influence of the lath boundaries.

Measured Data for the Strength of Low Carbon HSLA Steels

Empirically seen, the strength of the bainite in steels with comparable composition is widely dependent on the cooling rate and transformation temperature, as investigations by Cizek et al. show (fig. 2.4) [CWD+02]. The measured hardness increased steadily up to a cooling rate of 100°C/s, the uppermost cooling rate that has been achieved. The hardness against the transformation start temperature shows the same picture. The lower the transformation temperature, the higher the hardness.

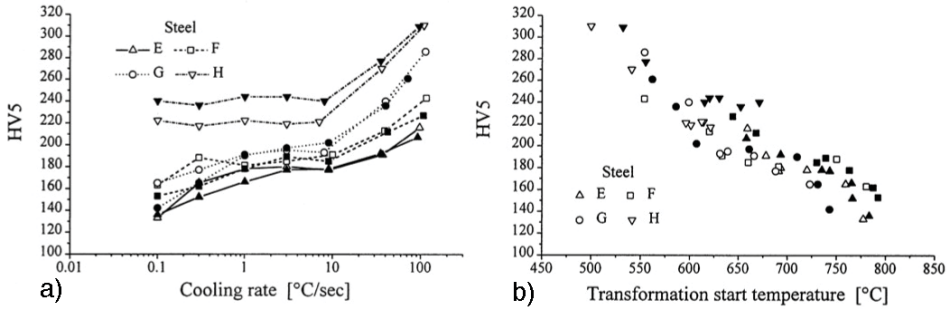

Figure 2.4: Hardness of low carbon steels after continuos cooling in dependency of the cooling rate (a) and the transformation temperature (b). Open symbols refer to recrystallized austenite, filled symbols to conditioned austenitic structures [CWD+02]. The chemical compositions are displayed in table 2.1

Steel	C	Si	Mn	P	S	Mo	Nb	Ti	B (ppm)
E	0.046	0.212	1.64	0.024	0.009	0.045	0.029	0.015	<1
F	0.043	0.210	1.67	0.018	0.011	0.260	0.022	0.016	<1
G	0.043	0.200	1.68	0.019	0.012	0.004	0.021	0.017	20
H	0.044	0.220	1.73	0.019	0.010	0.260	0.022	0.017	19

Table 2.1: Chemical compositions of the steels investigated in [CWD+02]

2.2 Displacive Transformations and the T_0 Concept

It is well known that in solids, transformations from one phase into another can occur either by diffusion or by a displacive mechanism. A combination of both is also possible if there are species present with very different diffusion coefficients (e.g subsitutionals and interstitials). It is possible to derive the conditions for displacive transformations from equilibrium thermodynamics, since the parent phase transforms into a product of the same chemical composition. This temperature, commonly known as T_0, below which there is a driving force for displacive transformations, is usually not displayed in phase diagrams. A graphical display of this condition for ferrous alloys is given in fig. 2.5. The T_0 concentration is located where the free energy curves of ferrite and austenite cross. The free energy curve of ferrite is further raised by additional strain energy. This lowers the possible transformation temperature further, leading to a temperature referred to as $T_0\prime$.

In ferrous alloys, the most common displacive transformations, that are possible are shear transformations. For these transformations it is known, that they have reaction fronts, that are able to move almost with the speed of sound. This gives a strict condition to this interface. Since interfaces can be described in terms of dislocations, it is clear, that only one set of dislocations must be able to describe the interface, because otherwise the dislocations would interact, producing non-glissile dislocation steps. This means the crystallographic orientation relationship has to leave at least one line invariant (unrotated and undistorted). This condition also entails that the interface is a very low energy interface, since obviously high coherency is present. The typical energy is 1J/mol [Bha01].

The dominating term in these transformations is the strain energy. Typical strains observed in ferrous alloys are shears in the range of of 0,22 and

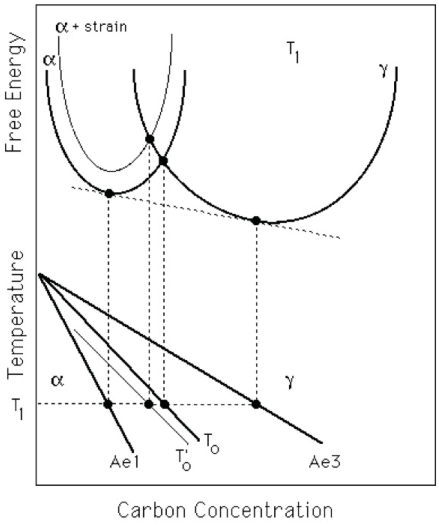

Figure 2.5: Illustration of the T_0 condition on the phase diagram. $T_0\prime$ includes the raise in free energy of the ferrite by strain

dilatations in the range of of 0,03. If we compare that with typical elastic strains of steels (0,005 for 1000MPa) there is a difference of three magnitudes. To minimize the strain energy, the product phase grows in a plate shape. The strain energy E_s is then given by equ. 2.12. Here, t/l is the thickness to length ratio of the product, G the shear modulus of the matrix, s the shear and d the dilatation. Typical strain energies in steels are in the range of 600J/mol. [Bha02]

$$E_s = \frac{t}{l} G(s^2 + d^2) \tag{2.12}$$

2.3 Martensite

2.3.1 The Martensitic Transformation

If we transform a steel at a temperature, where no diffusion is possible at all, the $\gamma \rightarrow \alpha$ transformation takes place by a displacive mechanism, called martensitic transformation. The critical cooling rate where this takes place is defined by the content of alloying elements, mainly C and to a minor extent (in comparison to C) Cr, Mo and nearly all other alloying elements.

Martensite is formed by shear deformation of the fcc γ iron into the bcc α iron. The diffusionless nature of the transformation entails that the chemical composition of the formed phase is identical to the parent phase, while the crystallography of the transformation demand certain reproducible orientation relationships between the parent and the product phase. For low carbon steels, often an orientation relationship close to the Kurdjumov - Sachs relationship is observed. This means that $\{111\}_A // \{110\}_M$ and $< 110 >_A // < 111 >_M$, meaning the close-packed planes are parallel as well as the close-packed directions. This is just an approximation since this relationship would not give line-invariant strain, in fact, the orientation relation also involves a rigid-body rotation. The overall transformation does not just have line-invariant strain, but plane invariant strain. This necessitates plastic accommodation of the martensite during its formation, leading to irrational habit planes. This plastic accommodation constraint can either be fulfilled by twinning or slipping. The latter is observed in low-carbon steels (relatively high transformation temperature).

The athermal nature of the transformation causes that the volume fraction of martensite formed by supercooling is just dependent on the undercooling and explicitly not on time. The volume fraction of martensite formed is dependent on the number of nuclei that can be activated by the undercooling below a certain temperature M_s(the martensite start temperature).

This leads to equ. 2.13 [Bha02], where $V_{\alpha'}$ is the martensite volume fraction, β is a constant and M_s is the martensite start temperature.

$$1 - V_{\alpha'} = e^{-\beta(M_s - T)} \text{.....} \beta \simeq 0,011 \tag{2.13}$$

2.3.2 The Strength of Low Carbon Martensite

In comparison to austenite of the same chemical composition, martensite in carbon steels shows a much higher hardness. This can not be explained by the shear transformation alone, since the increase in hardness is not observed in a lot of other metallic systems that show martensitic transformations. The strength obtained in the end depends on the obstacles for dislocations present, a lot of which can be found in a martensitic microstructure.

The most important fact hereby is, that the dissolved carbon strongly distorts the lattice of the martensite, since it is a forced supersaturation, obtained by the sudden change in solubility during the transformation from fcc to bcc. In fcc iron, the carbon isotropically expands the lattice, while in bcc iron, it does not. In fcc iron, C introduces a tetragonal distortion to the lattice. This is the reason why the interaction with dislocations of the carbon in solution is much higher in martensite than in austenite. Further strong contributions come from interfaces, namely twins, lath boundaries and sometimes subgrain boundaries.

2.3.3 Annealing of Martensite

The tempering of martensite takes place in four overlapping stages:

Stage 1 up to 250°C, the hexagonal ϵ carbide is precipitated, partial loss of the tetragonality, in low carbon steels (<0,2wt%) carbon segregation.

Stage 2 200°C to 300°C, decomposition of the retained austenite.

Stage 3 200°C to 350°C, replacement of the ϵ carbide by cementite, full loss of tetragonality.

Stage 4 >350°C, spherodization and coarsening of cementite, recrystallization of ferrite.

The reaction, observed in the third stage of tempering leads to the precipitation of cementite in a well defined orientation relationship. Three variants exist with respect to the ferrite lattice, differing from the lower bainite, where just one orientation is observed. In low carbon steels, these structures are observed even without tempering, resulting from carbide precipitation during quenching. During tempering, the cementite preferably nucleates at the ϵ carbide/matrix interfaces, gradually incorporating the ϵ carbide. [Bha01]

2.4 Bainite

2.4.1 The Bainite Reaction

In between the transformations $\gamma \rightarrow \alpha$ and the martensitic transformation yet another transformation exists, characterized by the fact that the bcc iron crystal has acicular shape, with fine carbides intercalated in the lath shaped crystals (lower bainite), or in between the crystals (upper bainite). Forms of bainite where no carbides are observed are also possible. Here, the distinction from low carbon martensite can get very tricky to pointless.

The transformation from γ into bainite is fairly complex, since the exact mechanism is dependent on the local carbon content, the content of other alloying elements, the cooling rate and the temperature where the bainite forms. What is seen as the reason for that is that diffusion driven transformations and shear transformations can occur parallel as well as coupled. This allows a lot of different mechanisms. In general, bainite consists of iron

carbide and ferrite, just like pearlite, but size, form and distribution can change significantly. This is why bainite is not a uniform microstructure, several different variations exist, as mentioned above.

Schematically, the transformation from γ into bainite starts with "slow"[1] shear transformation of the γ-crystal into a strongly supersaturated lath shaped bcc crystal. Hence, the bainitic ferrite has a crystallographic relationship to the parent crystal. It should be denoted that habit planes observed for bainite and martensite are different and also strongly differ for bainite formed at different temperatures, as shown by Greninger and Troiano [GT40]. This is displayed in fig. 2.6. As in the case of martensite, the habit planes are irrational, since plane-invariant strain is to be achieved by plastic accommodation.

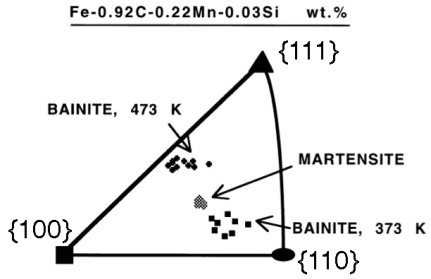

Figure 2.6: Results by Greninger and Troiano, showing the change in habit planes for different transformation mechanisms

This shear transformation, accompanied by plastic accommodation produces a high dislocation density ρ_d within both, the bainitic ferrite and the remaining austenite, which is widely dependent on the transformation temperature T. This has been investigated by Takahashi and Bhadeshia [TB90] resulting in an empirical equation (equ.. 2.14), based on data on isothermal

[1]Slow in comparison to martensitic transformations

transformations from 570K - 920K, displayed in fig. 2.7. It has to be emphasized that there is a wide scattering of the measured dislocation densities, making real quantification difficult.

$$\log \rho_d = 9,2840 + \frac{688073}{T} + \frac{1780360}{T^2} \tag{2.14}$$

The reason for the allowance of plastic accommodation is here the higher

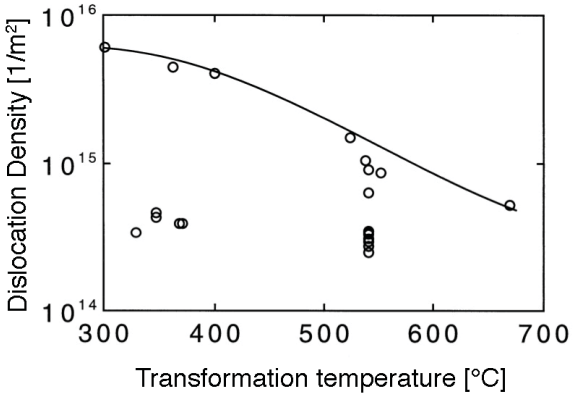

Figure 2.7: Dislocation density of martensite, bainite, acicular ferrite and Widmanstaetten ferrite as a function of the transformation temperature [Bha01]

temperature at which bainite forms. The strength of the austenite is lower then, promoting plastic accommodation. This is the reason, why bainite platelets grow to a finite size of $\approx 10\mu m$, since the high dislocation density produced interacts with the reaction front. The thickness/length of the platelets is given by the strain energy constraints. It has been found, using neural network models [Bha98], that the biggest influence on the bainite platelet size is the strength of the austenite, followed by the driving force of the reaction. If the austenite grain size is smaller than the expected length of the platelets, the austenite grain boundaries are not crossed by the growing

platelet. Data on the effect of the thickness of the platelets by this mechanism has not been found, but it can be expected that shorter platelets are also thinner, though minor changes in the aspect ratio might occur.

After the crystal has a bcc structure, the diffusion rate of C goes up rapidly and the C is able to abandon the ferrite quite fast. This fact, in combination with the T_0 concept causes a behavior that is called "the incomplete reaction phenomenon" [Bha81b, HBS82], meaning that the reaction will stop if the concentration of the remaining austenite reaches the T_0 concentration. This subsequent supersaturation of carbon in the adjacent austenite can (in low carbon steels) lead to the precipitation of cementite or the stabilization of the austenite [PBMB04]. If carbides are formed, the carbides have one orientation with respect to the ferrite.

The growth of the individual laths is proportional to time until it is finished, since just the region locally around the lath is influenced by the transformation.

The mechanism of the $\gamma \rightarrow \alpha$ transformation is martensite like, manifest in a relief that is formed on the surface and oriented growth of the laths in relation to the γ crystal. The difference is that in martensitic reactions, the relief contains just steps caused by martensite laths, whereas in bainitic reactions both the bainite and the austenite are deformed [SB96]. The carbide precipitation and segregation mechanism to the lath boundaries, in contrast, is diffusion controlled.

Further important is the fact that if the carbide is formed above $\approx 300°C$, the carbide formed is the rhomboedric Fe_3C that is the equilibrium carbide, below, it is usually the hexagonal ϵ-carbide, other carbides have also been reported [Bha01, p.85]. The lower the forming temperature of the bainite, the finer the carbides are, leading to higher hardness. But in the uppermost bainite regime, the carbides are even coarser than in the lowest pearlite regime, what can lead to even lower hardness than that of the lower pearlite.

The Distribution of the Elements

As the kinetics of bainite formation imply, there is diffusion going on during the reaction. It is generally agreed that a characteristic of the bainite reaction is the sole diffusion of interstitial elements[2] as already early (imaging) atom probe research confirmed [Bha81a, HBS82, SSB90]. From this follows that iron carbides are the only carbides to be observed in untempered bainite.

2.4.2 The Strength of Bainite

If we want to get an impression of the amounts in which the different strengthening mechanisms contribute to the strength, we have to consider the individual structural sizes and the volume fractions of the constituents of the bainite. [Bha01, p.293] Fig. 2.8 illustrates the values of the individual terms of an Fe-0,2C-3Mn-2Si fully bainitic microstructure, calculated by equ. 2.11. It has to be denoted that especially the ratio of lath boundary strengthening to dislocation strengthening can vary in a wide range (e.g. compare [Bha92, p.293] and [Bha01, p.287]).

The plates of the bainitic ferrite are typically $10\mu m$ in length[3] and about 200nm thick. Dislocations have a very small mean free path[4] and the probability to find a dislocation source in a neighboring grain is very small. The exact mechanisms of the strengthening are an object of discussion, to combine the model of Gouzou with the Langford-Cohen relation is a good approach if interfacial segregations are present.

What divides the bainite in the first place from the martensite is its dissolved C-content, that is lower, but in comparison to polygonal ferrite still higher, even in annealed condition. It is remarkable that, in spite of that, the dislocations still seem to be mobile, since no sharp yielding point is observed.

[2] the diffusion rate of C is 8 magnitudes higher that those of the substitutional elements

[3] If the γ grain-size is not smaller

[4] The mean free path for dislocations in laths is approx. twice the lath thickness

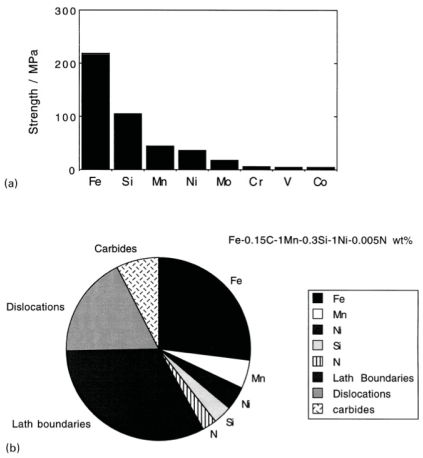

Figure 2.8: Tensile yield strength of bainite at 25°C, solid solution effect per $wt\%$ (a) and estimated contributions [Bha01]

This stands in contrast to recent atom probe research, where the trapping of solute atoms by dislocations in bainite has been observed [CM07]. It should be mentioned that cementite precipitates in a rather coarse form compared to other carbides. Interlath carbides do not contribute to the strength.

A further contribution, that is not to be neglected, is also given by the concentration of dissolved atoms, that are to follow Fleischer's equation (2.3).

The γ grain size is not known to have any effect on the bainite strength itself. It's contribution is indirect, effecting the transformation.

2.5 Precipitation Sequences and their Effect on the Material Properties

One of the most important aspects in the production of microalloyed HSLA steels are the precipitations formed inside the material. There are mainly

two types present: one type that formes at high temperatures during rolling and one that forms during cooling or a tempering treatment typically below 600°C.

2.5.1 The Precipitation of Vanadium Carbides during Annealing

Vanadium is a very strong carbide former even if very little of it is contained in a steel. In ferrous alloys, V forms the fcc VC, whose composition is often not stoichiometric, being closer to V_4C_3. For most steels, this is the only vanadium carbide observed.

Vanadium carbides form as small platelets, typically with a length of around 5nm and a thickness of 1nm initially. They show the Baker-Nutting relationship with respect to the ferrite crystal ($\{100\}_{VC}//\{110\}_{\alpha}$). The observed nucleation sites are dislocations inside the ferrite grain. In the early stages of the precipitation, the particles are coherent with the matrix, with a misfit of around 3%. Above a temperature of 700°C the VC begins to coarsen rapidly [BH06, p.199].

The secondary hardening peak caused by V is located at around 360°C for short annealing periods. A graphical display of this tempering curve is displayed in fig. 2.9 [Bha01].

Strengthening by the Precipitation of Vanadium Carbides

In the case of strengthening by vanadium carbides, if the size and volume fraction of the vanadium carbides are known, the yield strength increase can be calculated using a theory developed by Melander [Mel77]. A graphical display of this was published by Todd and Li [TP86] and can be seen in fig. 2.10. Using this, the overall hardening potential by VC precipitation could further be estimated by thermodynamic calculations giving the volume

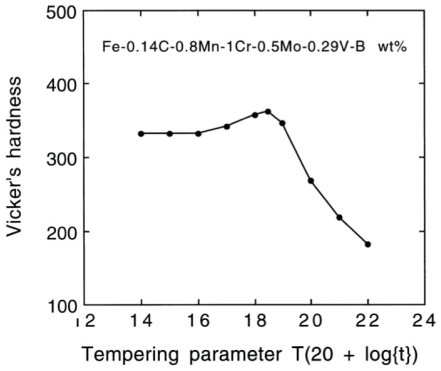

Figure 2.9: Illustration of the secondary hardening peak in a vanadium containing steel [Bha01]

fraction, maybe backed by TEM investigations of the particle size, and/or scattering methods.

2.5.2 The Precipitation of Ti/Nb Carbo-Nitrides at high Temperatures

In the case of thermomechanical processed steels containing Ti and Nb, (Ti,Nb)(C,N) particles inhibit recrystallization up to high temperatures. These particles are seen as a regular solution between the binary constituents.

fig. 2.11 shows a recrystallization diagram for a microalloyed steel at high temperatures. It can be seen that a very fine austenite grain size can be obtained if the strain, induced by rolling is high enough. It also has to be emphasized that if the material recrystallizes after every pass, the dislocations introduced by the rolling are erased. This means, the dislocation density goes down rapidly from around $10^{16}/m^2$ to $10^{12}/m^2$ [OH92].

Since the precipitation of these particles occurs via nucleation and growth, a distinct critical nucleus size has to be overcome, until the nucleus is stable.

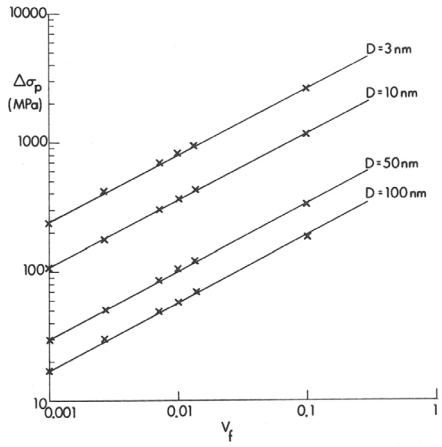

Figure 2.10: Yield strength increase in bcc iron caused by VC precipitation (calculated using Melander's theory)

This is caused by the fact that the interface grows with the second power of the radius, while the volume grows with the third power. The volume energy ΔG_v is the driving force behind the precipitation, while interfacial energy γ_s is the energetic cost to pay. A further energetic cost to pay is the strain field, the particles have around them. This is a term that often can not be neglected in solids, but plays a minor role if the precipitates are formed at high temperatures.

The interfacial energy in particular is the reason, why precipitates preferably nucleate at sites, where the lattice is already disordered or interfaces are present, like grain boundaries and dislocations. At these sites, the kinetic is also enhanced, since diffusion is faster. Fig. 2.12 displays the critical radius of a (Ti,Nb)(C,N) particle for different sites in austenite during cooling from 1300°C to 950°C. For the purpose of recrystallization inhibition, only the particles present at the former austenite grain boundaries are active.

A change in temperature also brings a change in composition of the

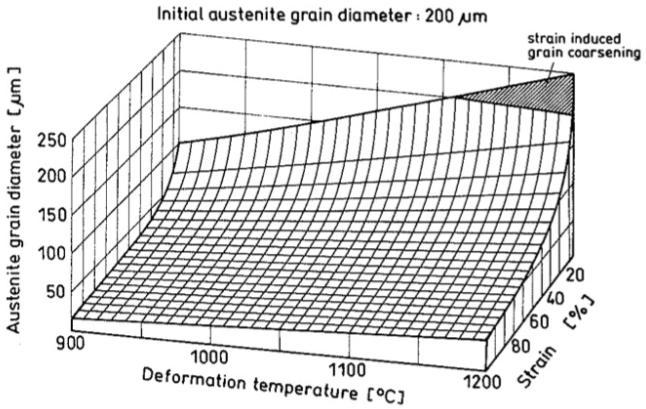

Figure 2.11: Recrystallization diagram for a Nb alloyed steel [KDMS92]

particles. Specifically, if formed at high temperatures, maybe even in the liquid phase, the particles exhibit a Nb/(Ti+Nb) ratio of 10% to around 20% [OH92, CHGB00], with a cuboid shape. It has further been found by Craven [CHGB00] that this ratio is widely independent from the overall Ti/Nb ratio in the steel. About the ratio C/N little is known. This is due to the difficulties in light element analysis in the electron microscope and the fact that the sample preparation technique used is usually the fabrication of carbon extraction replicas. Thermodynamic calculations suggest that the C/N ratio falls with rising temperature [OH92, ASH92]. At lower temperatures, the particles formed, tend to form NbC with only a minor inclusion of Ti.

As expected from fig. 2.12, the precipitation of particles away from interfaces goes faster by magnitudes, if the material has a high dislocation density. For (Ti,Nb)(C,N) particles this is displayed in fig. 2.13. This is also manifest in the different particle radii at the different sites (fig. 2.14).

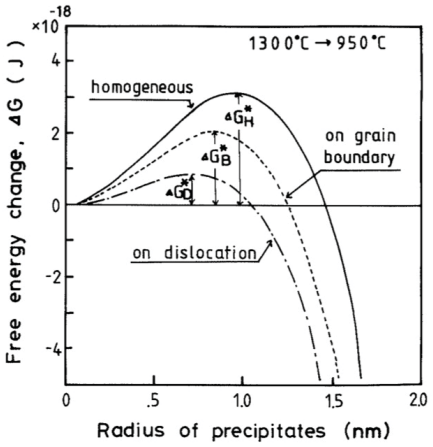

Figure 2.12: Relationship between free energy and particle radius of precipitates in 0,03%Nb-0,02%Ti steel [OH92].

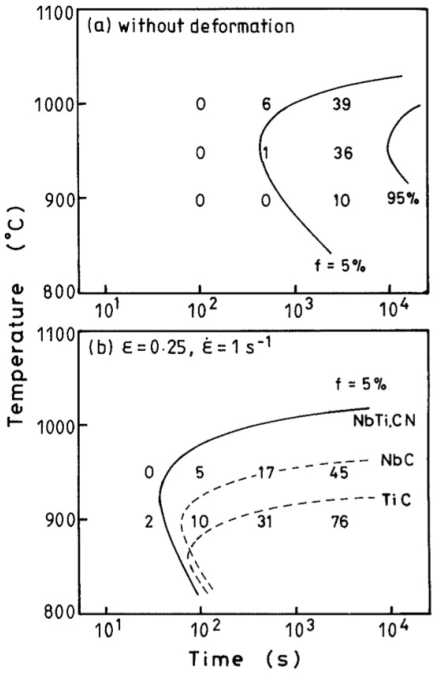

Figure 2.13: Calculated PTT diagrams for undeformed (a) and deformed (b) austenite, backed with measurement results [OH92].

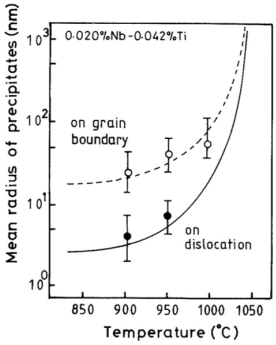

Figure 2.14: Average radius of precipitates at different sites and different temperatures [OH92].

2.5.3 Effect of the Austenite Grain Size/Austenite Conditioning on the Microstructure

If we want to get an impression of what effect the austenite conditioning has to bainitic/martensitic transformations, first the thermodynamics behind have to be considered. The main effect of austenite conditioning is the introduction of a dense dislocation debris into the austenite grain in comparison to recrystallized austenite. This increases the driving force for transformation. The deformation further increases the interfacial area per unit volume and the number of possible nucleation sites.

The effect of pancaking is also manifest in the CCT diagram of the steel. One for a steel, that is quite similar to the investigated one[5] has been published by Cizek et. al. [CWD+02], for undeformed and deformed austenite (fig. 2.15). Here, it can be seen that the transformation occurs in a temperature range from 500°C to 400°C for the cooling rate of around 30°C/s (dependent on the plate thickness) that is employed in the industrial process by voestalpine (DIC - direct intense cooling). Since this work has been performed using deformation dilatometry, the obtained strain (0,3 in the recrystallizing regime and 0,47 in the non-recrystallizing regime) is much lower than the rolling strain in an industrial process. What is observed, is that due to deformation, the transformation region is broadened and the transformation is shifted to slightly higher temperatures. Further, the volume fraction of martensite is lowered, what did not result in lower hardness.

Further data has recently been published by Jun et. al. [JKS+06][6], also here, the deformation has been performed using deformation dilatometry (3 passes, 20% reduction each). Here, only a slight raise in transformation temperature can be interpreted, but a very salient suppression of the martensite.

[5] 0,044C-0,22Si-0,019P-0,01S-1,73Mn-0,26Mo-0,022Nb-0,017Ti-19ppm B

[6] 0,051C-0,25Si-1,92Mn-0,067Ti-Nb-1,1Mo-Ni-Cr-40ppm N-15ppm B

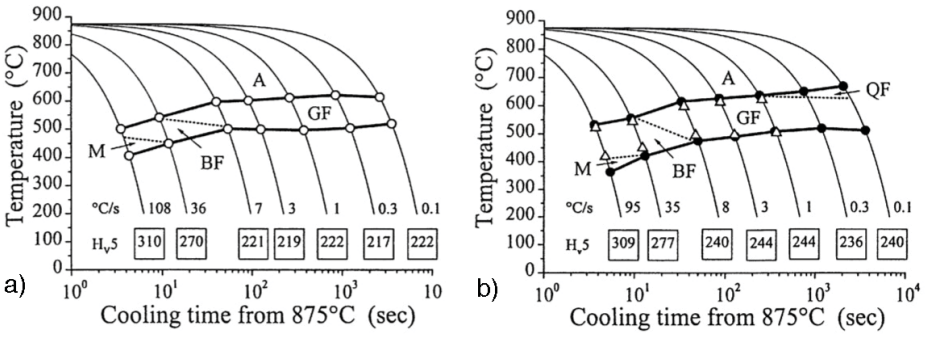

Figure 2.15: CCT - diagrams for a microalloyed B bearing steel without prior deformation (a) and with prior deformation (b). A-austenite, M-martensite, BF-bainitic ferrite, GF-granular ferrite, QF-massive ferrite [CWD+02]

Experiments employing a hot torsion testing machine, adding higher strains to the sample[7] have been carried out by Cota [CMBS99]. This work shows that at higher deformations (5 passes 20% reduction each recrystallizing, 4 passes 20% reduction each non recrystallizing) the bainitic region (bainite finish (B_f) at 450°C M_s at 350°C) seems to be well separated from the martensite start temperature M_s, what is displayed in Fig. 2.16.

[7] 0.08C-1.70Mn-0.25Si-0.029Al-0.033Nb-0.058V-0.17Ni-0.026Ti-0.0048N-0.0024ppmB

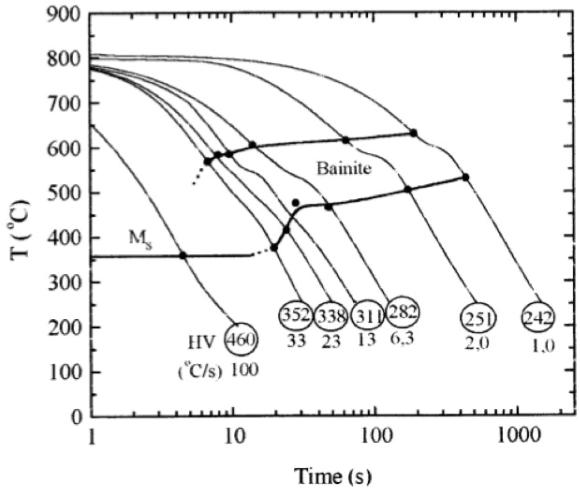

Figure 2.16: CCT diagram of a microalloyed bainitic steel after deformation [CMBS99]

2.6 The Effect of Boron Alloying on the $\gamma \rightarrow \alpha$ transformation

It is known for a long time that boron increases the hardenability of steel already when added in ppm amounts. Since the early 80's it is established, that this effect is caused by the retardation of heterogeneous ferrite nucleation at the austenite grain boundaries [BM80]. A possible explanation for that is that the boron lowers the interfacial energy of the austenite grain boundaries, making it a less effective site for heterogeneous nucleation. For commercial steels, a dissolved boron concentration of 20ppm is often sufficient [Lle93], since a too large amount leads to the formation of borides, especially BN, that are known to enhance ferrite nucleation.

For the reaction $B + N \rightleftharpoons BN$ in austenite, a solubility product is given

by Fountain and Chipman (equ. 2.15) [FC62].

$$logx_B^S \cdot x_N^S = -\frac{13970}{T} + 5,24 \tag{2.15}$$

Here, x_B^S and x_N^S are the concentrations of B and N in wt% and T is the absolute temperature.

In the time-temperature-transformation (TTT) diagram (fig. 2.17 (a)), the boron prolongs the induction period of the ferrite, thus promoting displacive transformations. In fig. 2.17 (b) it can be seen that a plateau is reached at a boron concentration between 20ppm and 40ppm.

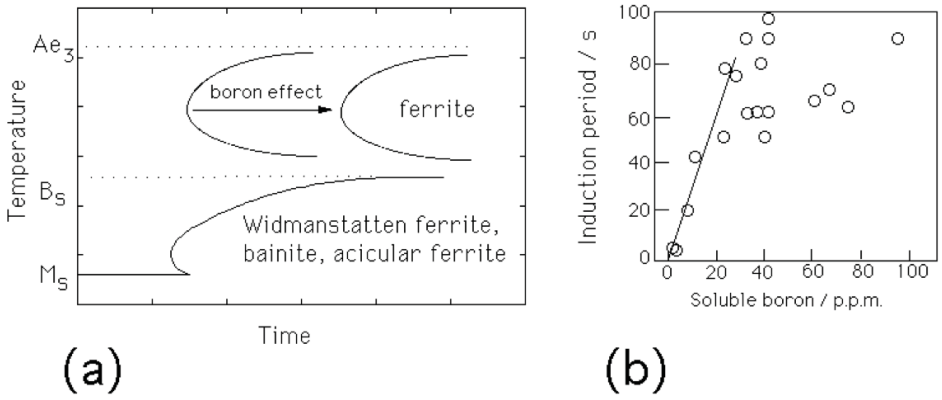

Figure 2.17: (a) Schematic of the effect of boron on the TTT diagram, (b) change of the incubation time of allotriomorphic ferrite as a function of the boron solute [BS93]

Chapter 3

Used Methods

3.1 Tensile testing (ZV)

Most important about the material under investigation are its tensile properties, e.g. yield strength (YS) and ultimate tensile strength (UTS). These values are measured in uniaxial loading under constant strain rate following the DIN EN 10002 standard. In the case of this work this was performed using samples corresponding to DIN 50125 form B with a diameter of 6mm. In the special case of the annealed states, the definition of UTS has been slightly bent, since the yield point has been slightly higher than the measured maximum tension at a large plastic strain. Still, the tension at a larger plastic strain has been taken as the UTS.

3.2 Charpy test (KBV, CVN)

The second value of importance for the practical use of heavy plates is their impact toughness at low temperatures, limiting the range of application. This is usually evaluated by Charpy tests (DIN 10045) that provide technological information about the fracture behavior at lower temperatures. The assembly

is rather simple: a pendulum hits a notched sample and the required energy to break the specimen is recorded. As a limit for use, often a value of 27J for a sample of 10mm thickness at a given temperature can be found. This goes back to the DIN EN 10025 that defines its lowest toughness class J having a minimum of 27J in the Charpy test. In this work, samples of 7,5mm thickness have been used, so the toughness class J would correspond to a value of 20,25J.

3.3 Light Microscopy (LM)

Thus the light microscope is the workhorse in the evaluation of the microstructure of materials, having a relatively low effort in sample preparation and a wide range of contrasting methods, it will always be the base of any structural investigation. In the case of micro-alloyed steels the main contrasting is provided by chemical etchants, mainly Nital and Bechet - Beujard‘s etchant.

The recipe for Nital is 2%-5% nitric acid dissolved in ethanol, Bechet - Beujard's etchant is basically picric acid in water with added HCl and Agepon (wetting agent). The recipe used in particular is: 300ml cold saturated picric acid with 20 droplets of HCl for the base solution. It should also be filtered to remove possible crystals of picric acid that could dissolve during later reheating. For the etching process itself, 40ml of the before-mentioned solution are taken, and 2 droplets of concentrated HCl and 2 droplets of Agepon (wetting agent) are added. The solution is to be applied at 80°C for 1min.

Nital contrasts the lath boundaries as-well as the former austenite grain boundaries or generally spoken about any inhomogeneity in the steel, while Bechet - Beujard‘s etchant selectively etches the former austenite grain boundaries. Descriptions of these methods can be found in [KB62].

A more advanced contrasting method is le Pera's etchant [LeP79], a mixture of picric acid in ethanol and potassiumdisufite in distilled water. Here, a layer is deposited in the anodic regions of the dissolution reaction. The layer thickness is dependent on the local reaction rate and the etching time. This gives coloring via interference [AFPK06]. Excellent results are furthermore obtained using polarized light for the micrographs, since all these layers have non cubic crystal systems.

3.3.1 A Chemical Etchant suitable for Phase Analysis (HFP)

Still, Le Pera‘s etchant has some disadvantages. The biggest problem is its difficult application, that often impedes reproducible results. Furthermore a useful contrast between the annealed martensite and the bainite could not be obtained. This led to the thought of an etchant that combines the technique of deposition etchants with more suitable electrolytes in an oxidic instead of an sulfitic environment. Found to be suitable was an mixture of 2ml 40%HF in 100ml 30%H_2O_2 applied at room temperature. The samples should be rinsed in 30%H_2O_2 afterwards to avoid pitting. Etching time was 10s for all samples.

This etchant produced good contrasts between martensite and bainite aswell as between different forms of martensite. It was also highly reproducible and formed very even microstructures.

The general problem using the light microscope in this specific case is the resolving limit of practically about 1000x, while the structures that provide the strengthening mechanisms in micro-alloyed steels tend to scratch this limit or need magnifications well above. A typical lath diameter for example is 100-300nm, making it impossible to be resolved by classical light microscopy, obeying Abbe's law. All other strengthening mechanisms base

on structures that are smaller by magnitudes. The next step in magnification is therefore the electron microscope.

3.4 Electron Microscopy

The resolving power of the electron microscope bases on the equivalent wavelength of electrons accelerated by an electric field as well as the energy of the electrons that makes them capable of interacting with the sample material in various ways. This enables simultaneous imaging, diffraction analysis and chemical analysis, a combination than cannot be provided by any other device type. By apparatus we divide into scanning electron microscopy and transmission electron microscopy.

3.4.1 Scanning Electron Microscopy (SEM)

SEMs use an electron beam of up to about 50kV acceleration voltage, that scans the sample surface (impinging illumination) (fig. 3.1). It records the interactions of the electron beam with the present position of the focus. The sample can have about any shape that fits the vacuum chamber, making it possible to investigate samples with virtually no preparation. The second main advantage is the high depth of focus, limited just by the convergence of the electron beam.

Since the electrons have sufficient energy to expel tightly bound core electrons from the sample atoms, the relaxation of this excited state provides X-rays that are characteristic for the atoms, making it possible to perform chemical analysis on microscopic scales. This is in lateral resolution limited by the fact that there is a trade off between the value of the acceleration voltage defining the interaction volume and the ability to excite the core electrons.

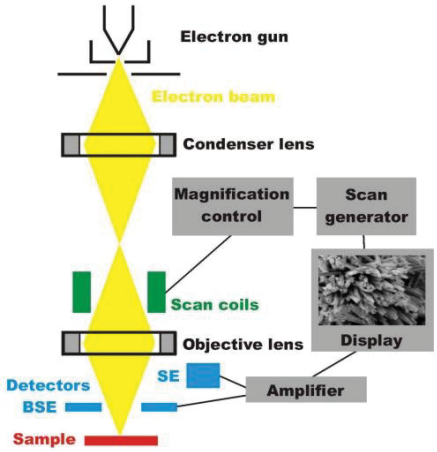

Figure 3.1: Imaging in the SEM [Kru]

The microscope majorly used in this work is an Zeiss EVO 50 SEM using an LaB_6 electron source with a maximum acceleration voltage of 30kV and an attached windowless energy dispersive X-ray analysis device (EDX) by Oxford Instruments (INCA Dry Cool). It was used to take pictures of the fracture surfaces from the charpy test as-well as from the metallographic samples at magnifications above the resolving limit of the light microscope. The used signal was secondary electrons. A good guidance for electron microscopy in the case of micro-alloyed HSLA steels can be found in [Bra87].

The X-ray analysis was used to provide information about some precipitation's on the grain and lath boundaries, being well on the limit where meaningful results with an LaB_6 emitter can be expected. The microscope where FIB is installed is an Zeiss 1540 with an Schottky FEG, capable of resolving features in the range of a few nm.

3.5 Transmission Electron Microscopy (TEM)

The TEM uses an electron beam with energies from typically 100kV upwards. The samples used are thin specimens (up to about 300nm), so the majority of the electrons is transmitted. The build-up of the image is rather complex, but for standard work, the microscope has an image transformation quite similar to the one in light microscopes. A simplified representation of the

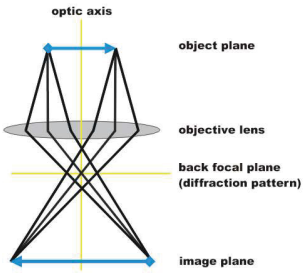

Figure 3.2: Imaging in the TEM [Kru]

ray path leading to the first intermediate image in the image plane of the objective lens can be found in fig. 3.2. Electrons, which come from the condenser system of the TEM, are scattered by the sample, situated in the object plane of the objective lens. Electrons scattered in the same direction are focused in the back focal plane, and, as a result, a diffraction pattern is formed there. The positioning of the aperture in the diffraction pattern is of vital importance for the image formation (fig. 3.3). Electrons coming from the same point of the object are focused in the image plane. In the TEM, the first intermediate image is magnified by further lenses (projective system) [Kru]. Most TEMs can also be operated in scanning mode (STEM), that has of course an image build-up for each individual illuminated spot.

In this work, a Phillips CM20 S/TEM (LaB_6 emitter) with an maximum acceleration voltage of 200kV and an energy dispersive X-Ray analysis device

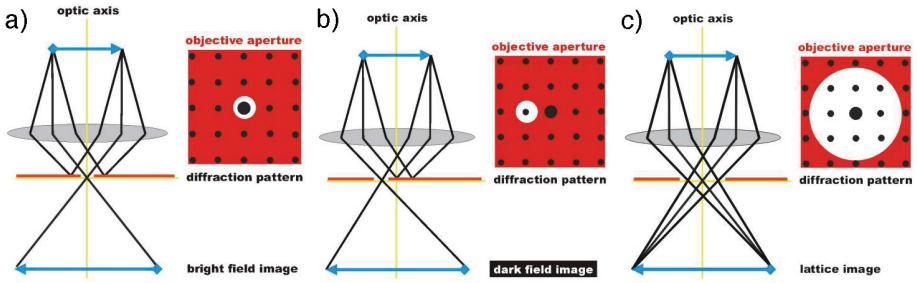

Figure 3.3: Imaging in the TEM dependent on the aperture position in the diffraction pattern [Kru]

has been applied for standard work, for high resolution imaging, a FEI Tecnai F20 G^2 (Schottky FEG) with 200kV capability was used.

3.5.1 Bright Field Images (BF)

In the bright field mode, an aperture is applied in the back focal plane of the objective lens (fig. 3.3 a). It only allows the direct beam to pass. Therefore, the image built-up results from a weakening of the direct beam (zeroth order diffraction) as it interacts with the sample. Hence, mass-thickness and diffraction contrast are the two phenomena that contribute to the image formation: thicker areas and areas in which heavy atoms are enriched as well as crystalline areas, that fulfill diffraction conditions, appear darker. Since all these phenomena occur simultaneously, an exact interpretation of the micrographs is not straight forward. Since dislocations are crystal defects, their orientation relative to the beam axis is important for the imaging as displayed in fig. 2.2.

3.5.2 Dark Field Images (DF)

To obtain dark field images, in contrast to the LM, where light is just shed sideways onto the sample, one or more first or higher order diffracted beams of crystalline regions in samples are used to build up the image, the direct beam is blocked (fig. 3.3 b). Since these beams have interacted strongly with the solid they contain more information about the crystalline phases in the material and their defects. It is for instance possible to image just one phase of the steel.

3.5.3 High Resolution Transmission Electron Microscopy (HRTEM)

To obtain high resolution lattice images, interference between the zeroth order beam and higher order diffracted beams is used (phase contrast). Therefore a larger aperture is chosen (fig. 3.3 c) and the sample has to be tilted, so its aligned with a zone axis parallel to the incident beam. If the point resolution of the microscope is good enough and the sample allows it, the atomic structure of the specimen can directly be examined in the microscope. The interpretation of these pictures then involves even more uncertainties than in the case of BF images, since the image transforms in a strongly nonlinear way for different spatial frequencies (described by the contrast transfer function (CTF)).

3.5.4 Electron Diffraction (ED) / Selected Area Diffraction (SAD)

The wave-like properties of the electrons also allow the recording of diffraction pattern similar to the ones of X-Rays. To obtain this, the primary beam is blocked out and the focal length of the diffraction lens is changed, so that the

diffraction pattern of a distinct region in the micrograph is projected onto the phosphorous screen. This allows the identification of phases in the TEM on the base of their crystal structure. In contrast to X-ray diffraction the scattering angles in the ED are rather small ($0° < \theta < 2°$), due to the smaller equivalent wavelength of the electrons (0,00197nm @ 300keV) in comparison to, for example, $CuK\alpha(0,154nm)$ radiation that has been used for the XRD in this work.

The main differences to XRD are, that ED can be performed in small volumes and that the electrons interact with the positive potential inside the electron cloud, while X-rays interact with the electron cloud.

3.5.5 Energy Dispersive X-Ray Detection (EDX)

Since the impinging electron beam bears quite some energy, it is able to interact strongly inelastic with matter. Most important here are the occurrence of bremsstrahlung and characteristic radiation. The bremsstrahlung is majorly defined by the acceleration voltage, while the principle shape of the characteristic radiation is independent of the apparatus. It is the chemical composition of the material that defines it. Responsible for that are transitions of core electrons in the material. These transitions have sharp defined energies, the frequentness of which is dependent on the content of the element in the material. It has to be considered that the relative intensity is influenced by the bulk s average atomic number, abortion and fluorescence[1]. This makes a quantitative analysis very difficult, but qualitative analysis is very time-efficient, especially when using a EDX. It is a Si crystal, doped with Li, that has the lowest excitation energy in Si (0,33eV). Incoming X-ray quanta excite charge carriers, until their energy is used up. This allows the identification of the energy of each individual photon. The energy resolution

[1] This is the so-called ZAF correction

is limited by the energy to excite a single charge carrier, superconducting detectors with better energy resolution are currently in development, but not commercially available. The used detector is an Oxford Instruments Inca Dry Cool in the case of the SEM, the TEM has an EDAX Apollo SDD detector attached.

In this work the individual peaks have just been labeled, omitting a quantitative interpretation. Nevertheless, the ratios of the peak heights are in accordance to the distributions of the chemical elements.

3.5.6 Thin Foil Preparation

To examine metals in the TEM, the standard procedure is to cut slices with 3mm in diameter and a thickness around $80 - 100\mu m$. These are further thinned by dimple grinding and ion polishing (Ar ions) to electron transparency (thickness <300nm). Another way is to thin them by electrochemical etching. Descriptions of this techniques can be found in [WC96, chapter 10].

3.5.7 Fabrication of Carbon Extraction Replicas

If the object of interest is not the bulk material itself, but, for example, precipitation's, these can be extracted with various techniques. Since the extracting film is supposed to influence the examination as little as possible, amorphous (or nearly amorphous) carbon films are the technique of choice [PI07]. To Investigate the precipitates, carbon extraction replicas have been fabricated by the ARCS Seibersdorf.

In principle, to fabricate such replicas, the sample material is etched slightly with ethanolic HNO_3, so the precipitates stick out of the surface. A vapor of carbon is then deposited and clasps around the precipitates. The sample is then etched further, so the film with the included precipitates can

be stripped. Since only a distinct fraction of the precipitates, mainly the ones that have been enclosed to around 2/3 and more, remain in the replica, it is only possible to extract one size range of the particles. In this work it has been tried to extract the smallest ones, down from around 50nm size. The smallest particles to be investigated are around 10nm.

In contrast to techniques where the precipitates are extracted by dissolution of the bulk material, the advantage is that the correlation with the microstructure is still intact and that the microstructure can be viewed in an area even much bigger than on thin foils, just limited by the mesh-width of the carrier-grid, though the statistics on the particles are not as good.

3.6 Atom Probe / Field Ion Microscopy (FIM)

If an electrostatic field is applied to a conductor, local curvatures lead to higher field intensities. This can be seen from Gauss theorem (equ. 3.1), since an electric conductor is field-free inside and the field is provided by surface charge carriers. The sharper curved the conductor, the more charge lies inside a volume V included by a surface of S.

$$\int_S E dA = \int_V \frac{q}{\varepsilon} dV \tag{3.1}$$

If we assume a sphere - like object (as a model for a tip apex), its electric field is given by equ. 3.2.

$$E = \frac{U}{r} \tag{3.2}$$

As one can see, the field at the surface is a term that depends on the radius with 1/r. So if the radius is just small enough, extremely high field intensities can be expected. These intensities can be so high, that they are able to ionize adsorbed atoms or to expel ions from the material. These effects can be used to either image the surface of the material on an atomic

level by recording adsorbed gas atoms that have been ionized or reconstruct the volume by identifying the evaporating ions from the sample. An imaging by field extracted electrons is also possible, but the resolution is much lower due to the equivalent wavelength of the electrons.

These effects have first been applied by E.W. Mueller in the 1960s [Mül60]by impressing a voltage between a needle-shaped tip and a spherical phosphorous screen with an image gas in between. This was the first device to ever image single atoms. Remarkable for a device of this simplicity. The Tomographic Atom Probe 3DAP uses this principle to image the specimen surface with better spatial resolution than in the atom probe mode and for proper alignment of the sample in the apparatus.

The same pointed needles are used in the atom probe, where besides the bias voltage a pulsed voltage or a laser pulse is used to evaporate single ions. This pulse also triggers a Time of Flight Measurement (TOF). The trajectory of the flying ion goes into a so-called reflectron, where an ion that starts at the beginning of the voltage pulse penetrates deeper and so looses its lead over the same atom that evaporates at the end of the pulse. It further follows the field lines and hits a 2D detector (microchannel plates with a delay line grid) at a position that is supposed to be a linear transformation of the surface position from where the atom has been emitted. The time measurement stops at that time, so the TOF represents the mass/charge ratio at a given voltage. From the voltage and the impact position on the detector a tomographic reconstruction of the tip can be performed. A description of the FIM and the Atom probe can be found in [BKC$^+$08, MS89, Mil03, CCG$^+$07, KL00, KM07].

Since the needle (or other) shape of the specimen and the assembly of the probe have a scatter field, the surface field of this assembly is no longer described by equ. 3.2. Luckily the field just differs by a linear factor called k. This factor is defined, so that equ. 3.3 describes the surface field. It has to be found either by experiment or by calculation as in [TKYS07]. The

Expression found is then equ. 3.3 [Mil03]. Since the evaporation field is given and the total voltage applied defines the susceptibility of the needle to fracture, a smaller value of k is preferred.

$$E = \frac{U}{k \cdot r} \tag{3.3}$$

3.6.1 Tomographic Atom Probe (3DAP)

The 3D atom probe by Oxford Nano Science (now part of Imago) is one of the latest devices in metals research. Atom probes are the only devices around that can provide atomic scale resolution with chemical identification of each single atom and even its isotope. The Department for Physical Metallurgy at the University of Leoben is in possession of one of these.

The 3DAP is able to operate from a bias voltage of 3500V up to 18500V with a puls frequency of 20kHz and a detector efficiency of 35%. For the k - factor, a value of 6 has turned out to be a good figure. Usually we choose a evaporation rate of 1,5% - 2,5% and a pulse fraction of 20% (ratio of pulse voltage / bias voltage). The actual limit to the bias voltage is the pulser, that is able to operate up to 3000V. That means that in average, every 50 pulses, an ion is detected or about 1 - 1,5Mio atoms per hour. A good run contains around 20Mio atoms leading to a reconstructed volume of, for instance, 60x60x180nm.

Sample preparation

The standard procedure to provide pointed needles on an atomic level is by electrochemical etching. A rod - shaped sample (usually 300μm square cross - section) is therefore dipped into a layer of 25% perchloric acid in 75% acetic acid ("step 1") that floats on an inert fluid (galden®, provided by solvay solexis). The external voltage (9V - 17V) is then applied until a

neck is formed, while the specimen is moved lengthwise up and down. The necked sample is dipped into an uniform fluid, namely 2% perchloric acid in butoxyethanol ("step 2") that is somewhat less aggressive and gives a well polished surface. 12 V have turned out to be a good value for the polishing. Short voltage pulses are then applied until the two parts of the sample fall apart. For the final pulses, a voltage of 9,5V gave the best results. In general, it can be stated, that longer polishing led to longer runs in the atom probe. Re-shaping of a fractured specimen can be obtained by electropolishing in a droplet of "step 2" included in a ring of gold wire. This often produces even better results. The surface is then comparable to one that has been electropolished, what means that a faint microstructure is present on the surface. It is assumed, that this is one of the reasons why martensitic and bainitic samples are very prone to factures in the voltage mode.

It is quite obvious that this preparation technique, though easy to use and quite cost- and time-efficient, is not selective, at lest not in an influenceable way. Many questions that can be answered using atom probe techniques, demand site specific preparation methods.

3.6.2 Local Electrode Atom Probe (LEAP)

The most sophisticated atom probe around is the so called LEAP 3000X HR by Imago, which is also present at the Department for Physical Metallurgy in Leoben. In contrast to the 3DAP with its remote counter electrode, the LEAP has an counter electrode with an aperture of $45\mu m$ that is located just in front of the needle‘s tip, while the specimen can be moved in all three spatial directions. This makes it capable of measuring local tips that are just divided by distances in the range of the aperture diameter. In this work, it has been tried to find a method to produce samples that can be investigated in the TEM (standard 3mm slices) as well as in the LEAP. This is based

on a recent technique presented in [SCM+07]. Multiple tips per sample are possible and also the ion thinning of regions of interest for the TEM.

The LEAP operates from a bias voltage of 400V up to 14500V while the evaporation pulses can be applied either by voltage pulsing or by laser pulsing (the X in LEAP 3000X). Laser pulsing has the advantage that it tends to be more gentle to the sample and that it enables the measurement of non - conducting samples (not relevant in this case). On the other hand the laser slightly blurs the mass spectrum and tends to evaporate more complex ions, that are sometimes hard to identify.

The pulse frequency is 200kHz and the evaporation rate can be up to 5% or even more. This beats the 3DAP by magnitudes, single runs can have up to 200Mio ions and up to two microns or more in length. The analysis cross section is up to 100x100nm, depending on the tip radius. Due to the local electrode, the scattering field in the LEAP is lower than that in the 3DAP leading to a k of around 3. In the case of site - specific sample preparation, the shape of the tip surrounding can lead to a slightly higher k (as can be seen from equ.. 3.1 if the surface of integral includes more sample surface in comparison to its included volume). This can be compared to the images of the TEM. Desirable would be calculations of the field factor depending on the depth of the line cuts, to get the optimal distance that does not influence the measurement in order to minimize the cutting times required.

Sample preparation with Focused Ion Beam (FIB) / Scanning Ion (Electron) Microscopy (SIM/SEM)

For the LEAP, besides the standard needles, also before-mentioned slices can be used. These slices have a diameter of 3mm and a thickness of $100\mu m$. First they are glued on an aluminum rod and etched to get the orientation of the sample (if textured). If the sample is in the right angle, two slits are cut into it to ensure the right position in the sample holder. To obtain

a thin wedge, they are glued on a glass plate with a thermal glue that is fully removable and ground (SiC paper, 2400 mesh and 4000 mesh, Diamond paste $1\mu m$, rotating tables) to an angle of approx. 1°. This removes most of the bulk material around the potential tip to minimize cutting times with the FIB, still enabling a microstructural investigation with the SIM/SEM. The geometry obtained was 500nm thickness at the edge and $5\mu m$ in $100\mu m$ depth. The usable width was then about 2mm. The FIB is able to remove around $1\mu m^3/s$.

SIM is the recording of the secondary electrons that are knocked out by the incoming ions (usually Ga^+ from a Liquid Metal Ion Source)[2] of the FIB. Since these ions have a momentum that is by far bigger than the one of electrons of the same energy, they penetrate the material much deeper. This depth is largely influenced by the type of crystal as-well as the crystal orientation relative to the beam axis. This effect is called channeling. It often allows the direct observation of the materials microstructure without chemical pre-treatment. If this is not the case, such as for small carbides, classical chemical etching can a be used.

Once the site of interest is defined (3.4), a small rod is fabricated by four triangular shaped line cuts at high milling current-densities. We used a current of 5nA at an acceleration voltage of 30kV. The length of the rod has been chosen to be $100\mu m$ initially, but has been reduced to $50\mu m$. Other groups have even used $20\mu m$ long stubs in the voltage mode and tips shorter than $10\mu m$ in laser mode[3]. Finally, a tip is shaped by annular milling patterns with stepwise decreasing inner radius (last pattern: 120nm inner radius, 100nA). The impinging Ga ion beam produces an amorphized zone up to 100nm, where artifacts are to be expected. It is desired, to examine the

[2] A He based FIB has been introduced by Zeiss SMT in Fall 2007

[3] personal communications with Dr. David Saxey of the Materials Dept., University of Oxford.

result of the milling in the TEM, which also allows to directly compare the electron microscope image with its better spatial resolution with the atom probe micrograph with its full chemical resolution. This is a task, that has not been finished in the present work. An example of the result obtained with a P91 type steel is displayed in fig. 3.4, the tip exhibited produced a run of 27Mio ions.

3.7 X-ray Diffraction (XRD)

If X-Rays are shed onto a crystalline solid, the diffracted beam shows maxima and minima, the spatial distribution of which is dependent on the crystal structure of the solid. This is (for lattice planes) described by Bragg's equation , where n is the diffraction order, d is the lattice spacing of the individual plane, λ is the wavelength of the radiation (Cu Ka, 0.154nm) leading to a diffraction angle of θ .

$$n\lambda = 2d \sin\theta \tag{3.4}$$

In the case of polycrystalline solids, these sharp rays form cones (powder diffractogram) due to the random orientation of the crystallites, each cone represents a different lattice plane. Using a so-called $\theta - 2\theta$ assembly, an electronic detector at an angle of 2θ to the source can be applied. This leads to a distribution of the intensity over the diffraction angle, resulting in "sharp" peaks. The peak's shape furthermore contains information of defects of atomic order of magnitude, such as dislocations and vacancies. The incoming X-ray quanta are counted for a defined time (3,2s in the present case) at each fixed angle. The stepwidth was $2/1000^\circ$ (2θ), since this is the limit of the apparatus.

In this case the focus is on the shift and the broadening of the peaks, caused by defects, distorting the crystal lattice. The (110) peak of the iron

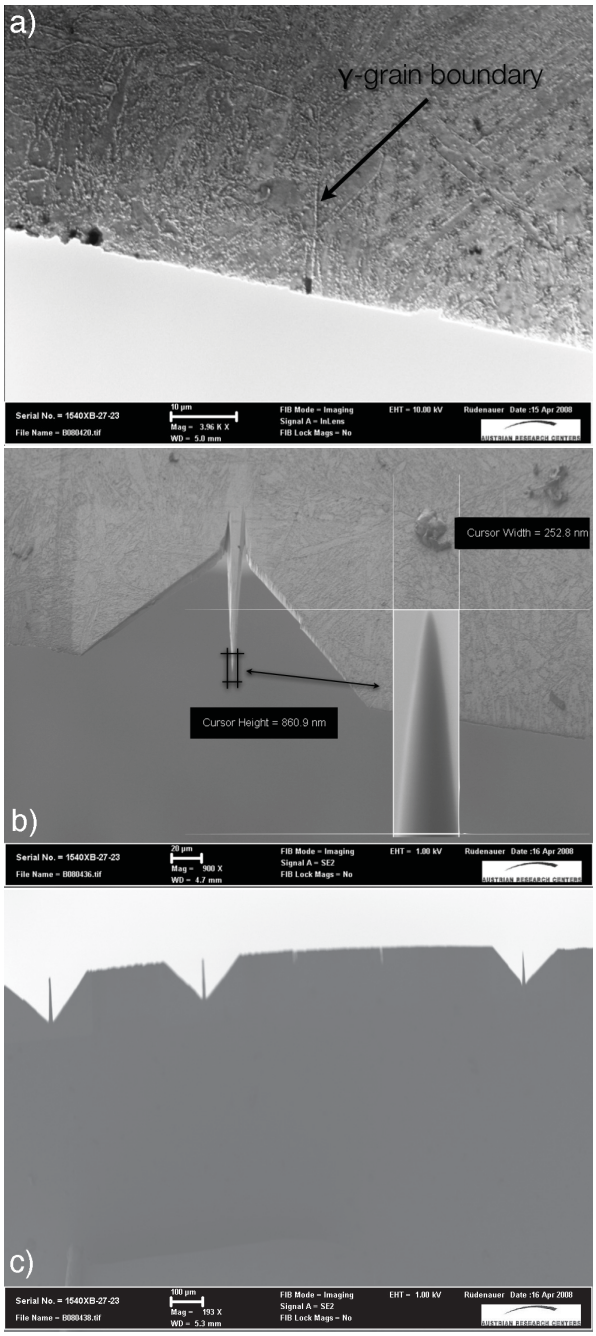

Figure 3.4: Atom probe sample of a P91 type steel, produced with the FIB mill (SEM-SE): the original position of the stub (SIM-SE) (a) and the final tip (b), multiple tips per sample are possible (c)

was taken, and its evolution during an annealing process up to 600°C was measured. The figures characterizing the peak are the location of its maximum and its full width at half maximum (FWHM). For noise reduction, a 5-point average of the diffraction data was used. The samples have been extracted from from the PaQ state material as thin slices (approx. 1mm thick) and heat treated at the specified temperature for 24min. The oxide layer has been removed afterwards. The device used was a Siemens Kristalloflex D500 diffractometer.

3.8 Dilatometry

A dilatometer is used to follow the linear thermal expansion of a solid through different temperature regions.

In the case of a push - rod dilatometer a sample is inserted into a furnace and heated, in the present case, by induction. Accelerated cooling can be obtained by nitrogen. The sample lies in between two rams, that ideally show no expansion. During the temperature program, the travel of the dies is recorded. The measurements have been performed employing a Bähr DIL 805 A/D, with samples of diameter 2,5mm, the nitrogen gas flow necessary to obtain the desired cooling rates is automatically controlled by the apparatus.

Chapter 4

Material and its Heat Treatment Conditions

4.1 Chemical Composition

The chemical composition of the trial plate studied in this work is shown in Table 4.1.

C is the main influence on the material's strength and toughness as well as weldability. This means: as high as possible (cost efficiency), but still guaranteeing weldability and fracture toughness at low temperatures.

Mn is the main alloying element in m%. It is used for solid solution hardening and because of its quite low price, it is tried to take as much as possible until the materials properties begin to suffer. 2% is already quite the limit for this class of steels. High levels are blamed to weaken the GB by segregation. (Si is also suspected to do so.)

Cr, Mo are alloyed for diffusion retardation, to obtain a bainitic or martensitic microstructure. The presence of Mo is also known to inhibit P segregation.

Nb, Ti are to form precipitations at high temperatures as explained above. Ti is also used to vanish N, while Nb can also form secondary hardening particles.

P, S are kept as low as possible, as they are detrimental to the quality. Especially S influences the toughness at this level of strength quite much (purity level - non-metallic inclusions). A Ca-treatment for desulphurication has been performed.

Al, Si are contained in an amount that comes from deoxidation/denitrition.

Element	Mass %	Atomic %
C	0,07	0,32
Mn	2	2,01
Cr	0,5	0,53
Mo	0,2	0,11
V	0,04	0,043
Nb	0,03	0,018
Ti	0,01	0,012
B	0,001	0,005
N	0,006	0,0238
Al	0,07	0,32
Si	0,35	0,69
P	0,013	0,0232
S	0,0008	0,0013
Fe	balance	balance

Table 4.1: Chemical composition of the trial plate

4.2 The Rolling Sequence

The complete rolling sequence is shown in table 4.2. The first part of the

pass	durance 1)	wait 2)	rev 3)	thickness	E-TEMP 4)
1	1,0	96,8		188,5	1009
2	0,1	0	8,4	171,96	1000
3	1,9	0	4,7	158,64	995
4	0,3	0	15,6	138,89	986
5	2,3	0	4,7	121,28	982
6	1,4	0	16	101,64	982
7	0,9	0	5,4	85,29	981
8	1,5	0	3,3	72,9	981
9	1,1	0	3	63,23	984
10	0,7	0	3,9	55,56	991
11	1,8	0	3,3	49,36	996
12	1,9	289		49,36	
13	1,6	0	13,4	41,13	811
14	1,9	0	4,1	33,88	795
15	2,8	0	3,4	26,54	791
16	2,6	0	3,6	20,75	812
17	3,0	0	3,5	16,92	815
18	2,9	0	3,6	14,14	822
19	3,4	0	3,7	12,35	812
1) contact durance pate - rolls [s]					
2) interpass cooling time [s]					
3) interpass time [s]					
4) entering temperature of the plate [°C]					

Table 4.2: Rolling sequence of the trial plate

rolling (from 200mm down to 50mm thickness) is done around 1000°C, a region where recrystallization takes place. This is a net deformation degree φ of 1,39. The second part, called ”austenite conditioning” or ”pancaking” is done around 800°C, with a summed deformation degree of 1,43 (50mm - 12mm). Here, precipitations inhibit recrystallization, so the γ is just deformed into elongated stripes. How complete the inhibition of the grain growth and recrystallization is can just be guessed, but no polygonal austenite grains have been found.

4.3 Sample Fabrication

All samples have been manufactured from the same trial plate, within a region of 150cm. The layout, how the samples have been extracted can be found in fig. 4.1. R12 stands for the tensile testing samples, K12 for the CVN samples. S marks the metallographic samples. The tensile tests have been carried out in longitudinal (L) and transverse (T) direction, whereas the Charpy V-notch (CVN) samples have just been extracted in transverse direction.

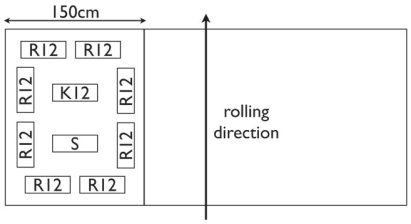

Figure 4.1: Extraction layout of the samples, the rolling direction is vertical.

4.4 The Heat Treatment Conditions

To evaluate the material‘s answer on annealing and the effect of pancaking, different heat treatment conditions have been chosen. As a comparison one state was chosen to be ”normalized” with slow air cooling, to get an impression what effect a weld would have in the worst case. This gives five different heat treatment conditions on the whole (table 4.3). All five have in common that they have been thermomechanically rolled and quenched (Direct Intensive Cooling - DIC) initially.

Name	Additional Treatment
PaQ	none
PaA	annealed at 620°C, 24min, air cooling
PoQ	hardening 1000°C, 12min, quenched (water)
PoA	hardening 1000°C, 12min, quenched (water), annealed at 620°C, 24min, air cooling
N	normalized 1000°C, 12min, air cooling

Table 4.3: Nomenclature of the heat treatment conditions

Chapter 5

Results

5.1 Austenite Microstructure after Pancaking

After the material has been quenched, the former austenite microstructure can be displayed using Bechet-Beujards etchant. In the micrograph (fig. 5.1), elongated grains with a high aspect ratio can be seen. A typical length is $200\mu m - 500\mu m$. The thickness of the grains is in the range of a few microns up to $20\mu m$, thus already in the range of bainite platelet sizes. By line-intersection, the austenite surface area has been determined. This has happened using fig. 5.1. It has been assumed that the austenite grain surface can be approximated by the number of intersections per length. This determines the austenite grain surface to be $319000m^2/m^3$.

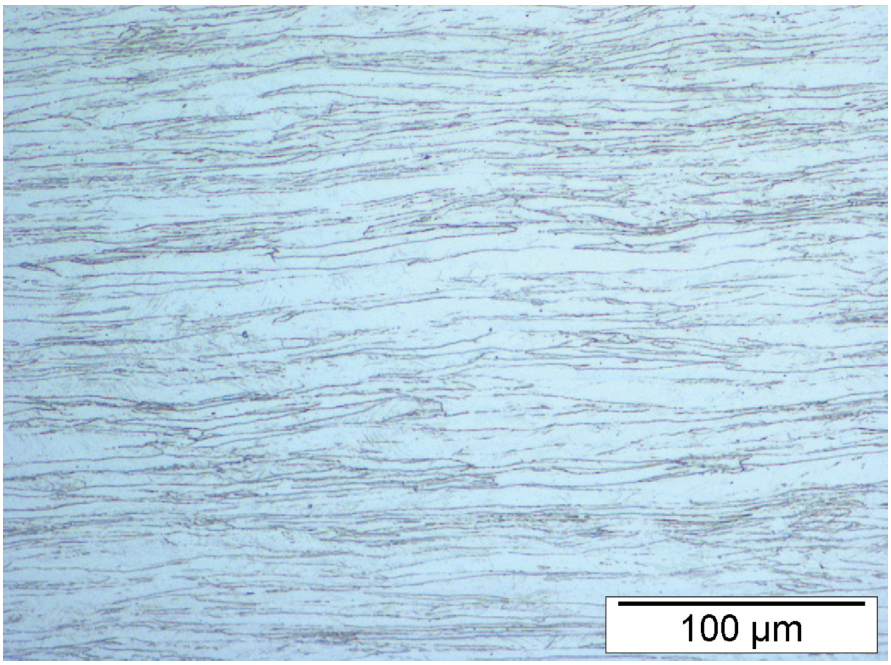

Figure 5.1: Former austenite structure of the PaQ state, etched with Bechet - Beaujards etchant

5.2 Transformation Temperature of the Polygonal Microstructure

Since the transformation temperature plays a key role for the formation of the microstructure, largely influencing the austenite strength during the transformation and the driving force for the transformation, quenching measurements employing a push-rod dilatometer have been performed.

For practical reasons, it has just been possible, to measure the transformation temperature of the material, starting from a polygonal microstructure. In principle, a measurement in a heavily deformed state, starting from the as-cast state would be important, but was omitted, because such high strains are not attainable, employing a dilatometer.

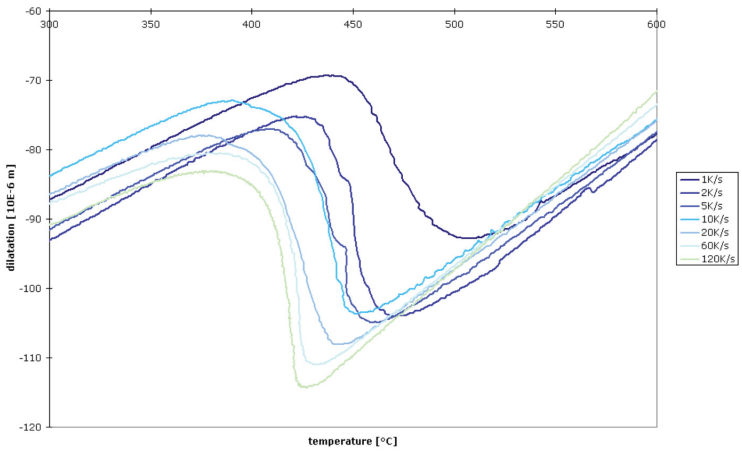

Figure 5.2: Cooling curves of the polygonal microstructure in the dilatometer in a range from 1K/s to 120K/s

Dilatometer curves for quenching and cooling have been recorded in a range from 1°C/s up to 120°C/s (fig. 5.2). The sequence started with heating up to 600°C with 10°C/s, then 2°C/s to 920°C with a soaking time of 300s

at 920°C. The cooling rates were 1, 2, 5, 10, 20, 60 and 120°C/s. The important temperature range for the transformation was found to be from 550°C to 350°C. For a cooling rate of 20°C/s, closest to the industrial process, the onset of the transformation is around 450°C. For very slow cooling rates (1°C/s) the transformation onset shifts up to 500°C, for medium cooling rates (2-20°C/s) it lies around 450°C and for high cooling rates (60-120°C/s), the transformation onset is around 430°C.

5.3 Pancaked Austenite with Quenching (PaQ)

From an economic viewpoint, the most important of the investigated heat treatment conditions is the PaQ condition, since it is the condition in which the material is shipped. This means the major effort in characterization has been put in the PaQ state.

5.3.1 Mechanical Properties

In the tensile test, longitudinal and transverse samples have been tested. For the CVN test, only transverse samples have been fabricated. The stress-strain diagrams can be seen in fig. 5.3, the toughness-temperature diagrams of the material are displayed in fig. 5.4, the corresponding values are summarized in table 5.1.

	transverse	longitudinal
UTS [MPa]	1269	1182
YS [MPa]	1025	924
A [%]	12,31	14,6
YR	0,81	0,78

Table 5.1: Mechanical properties of the PaQ state

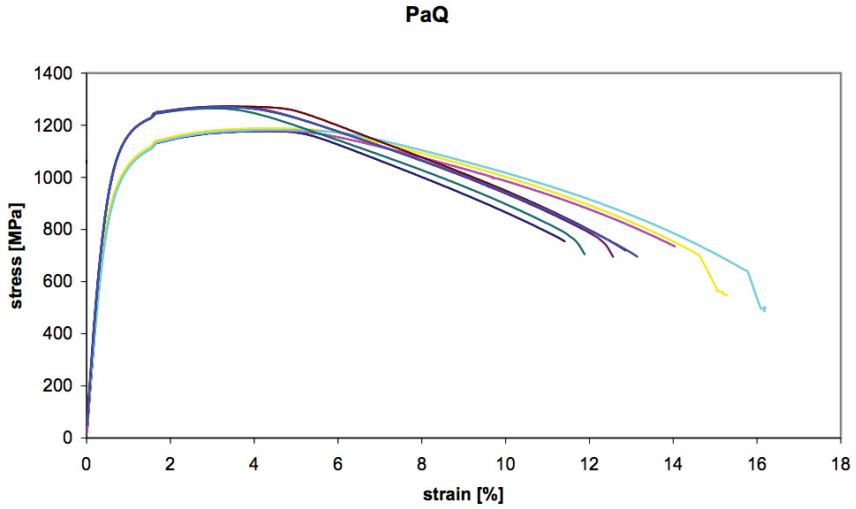

Figure 5.3: Stress-strain diagrams of the state PaQ

What stands out is, first of all, that there are differences in YS and UTS for different orientations of the samples. The samples that are orientated longitudinal (L) in the plate show a UTS of approx. 1180MPa, while the samples oriented transverse (T) to the rolling direction have an UTS of 1270MPa. The fracture elongation (A) corresponds to that, being lower for the higher UTS. It has to be mentioned that the samples show a lengthwise fracture, short before the final fracture, which is located right in the middle of the sample, that is said to be caused by the middle segregation of the plate. The YS are 1025MPa and 924MPa, respectively. The yield ratios are approximately equal for the L and the T direction.

In the toughness-temperature diagram it can be perceived that the material has no clear transition temperature. It shows an approximately linear dependence of the CVN values on temperature, still being above the limit (T_{27}) at -60°C with just one sample being below at -80°C.

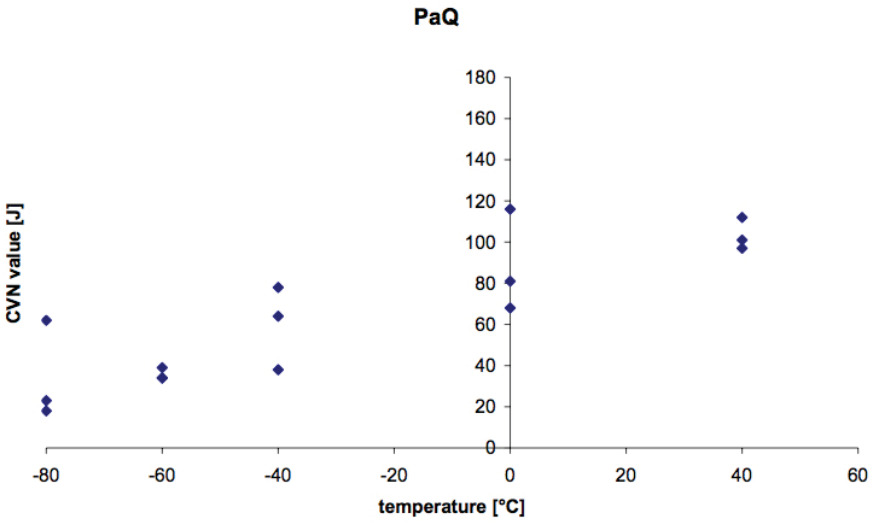

Figure 5.4: The impact toughness temperature diagrams of the state PaQ

5.3.2 Microstructure

The PaQ state consists of majorly three different constituents, all three present within one former austenite grain (fig. 5.5). The dominating constituent is lath shaped, interrupted by uniform areas, sized about 20-30 μm (marked "1" in fig. 5.5 b), in rarer cases up to $100\mu m$. The third constituent can more easily be distinguished with HFP (labeled "2" in figs. 5.5b, 5.6). It's aspect is quite equal to the one of the uniform areas, but the size and shape equals the laths of the lath shaped constituent. Comparing the micrographs obtained with Nital and HFP (fig. 5.5), a differentiation between the different constituents is very difficult in the micrographs etched with Nital, using optical microscopy.

Images taken in the SEM show (fig. 5.7) that the lath shaped areas show clear boundaries between each other that have been etched less by the Nital, while the uniform areas show small dashes inside (marked with arrows in fig. 5.7 a) and b)) This suggests that the lath shaped areas are bainitic whereas the smaller uniform ones as well as the bigger ones are annealed martensite. A justification for this assumption follows.

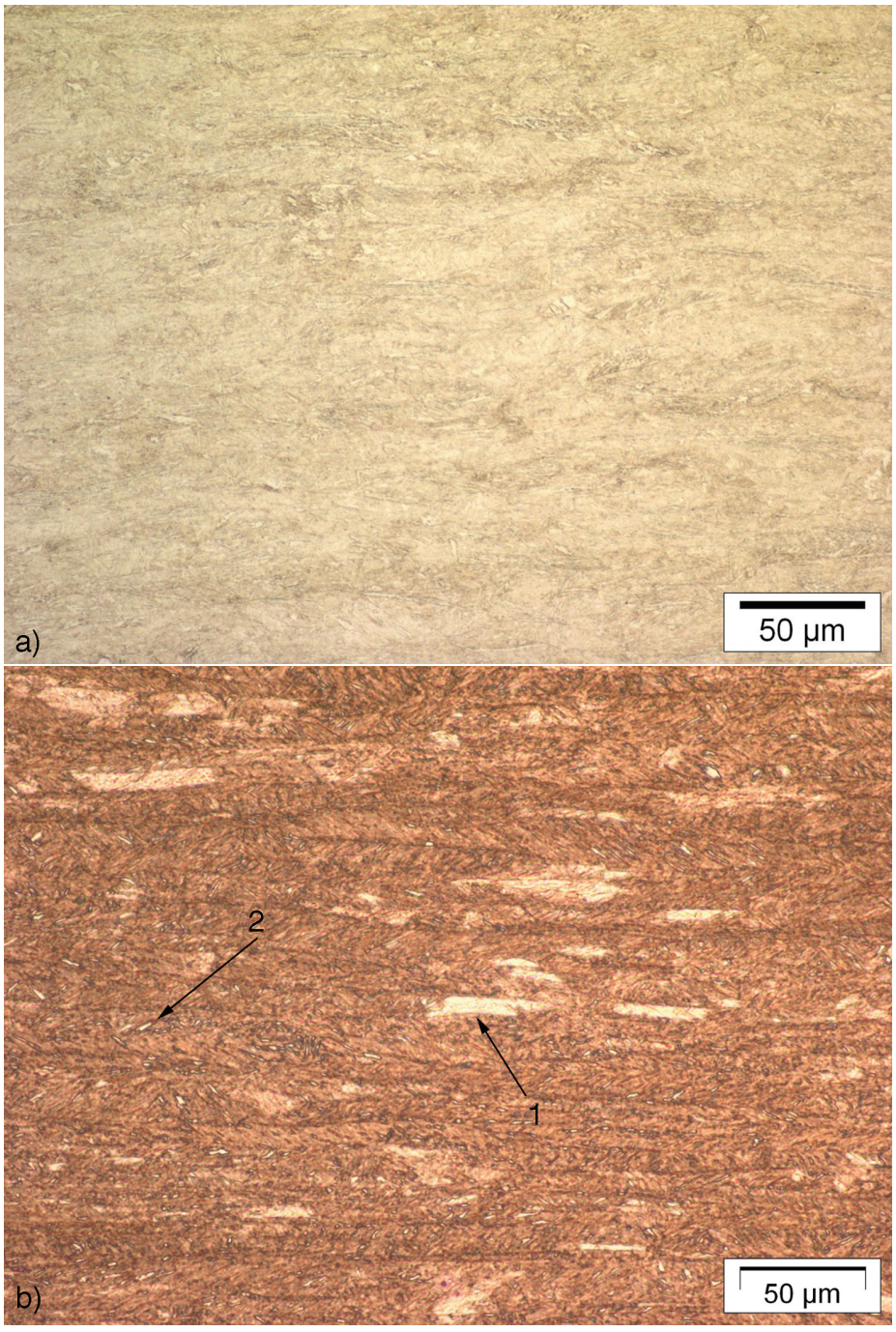

Figure 5.5: The microstructure of the PaQ state in the LM, etched with Nital a) and HFP b). Marked with arrows: "1" martensitic island, "2" martensitic lath

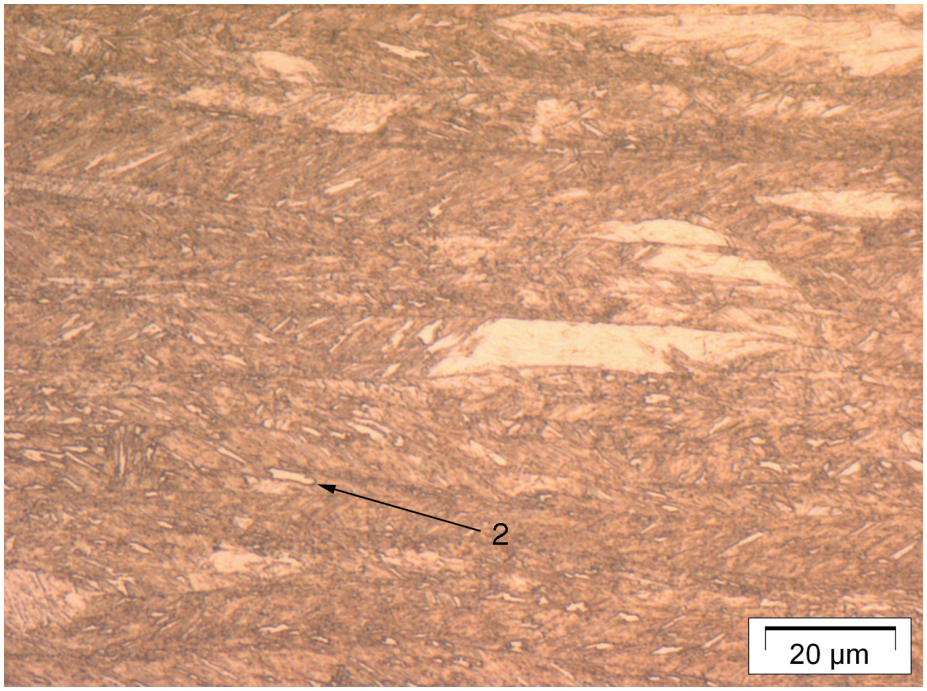

Figure 5.6: Microstructure of the PaQ state in the LM, etched with HFP, "2": martensitic lath

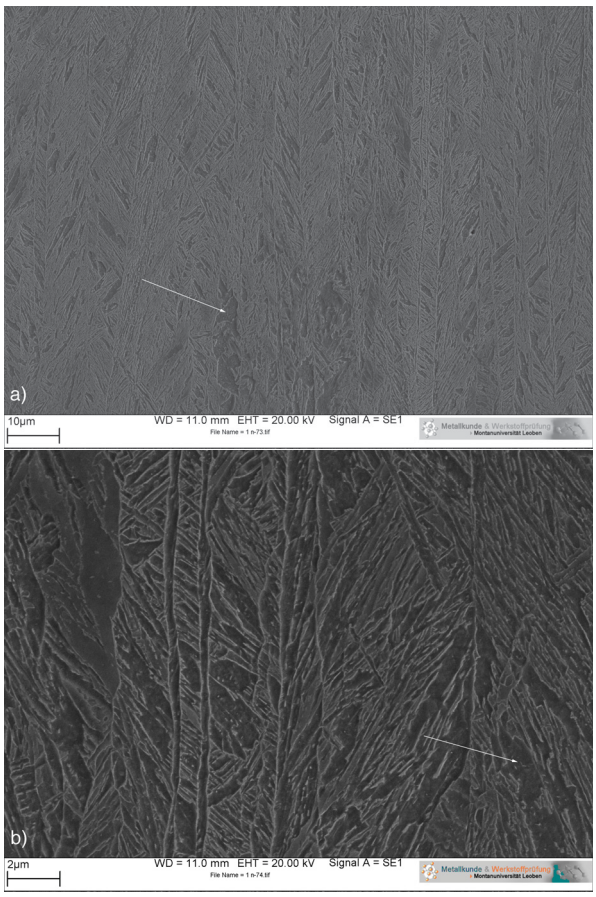

Figure 5.7: Microstructure of the PaQ state in the SEM, etched with Nital b) is a detail of a)). Arrows: auto-tempered martensite

5.3.3 Submicrostructure

TEM investigations proved what has been assumed in the SEM. A general overview (fig. 5.8) shows a lath shaped microstructure with a spotwise high dislocation density, where a dark film is often observed at the lath and grain boundaries. Areas with inhomogeniously distributed precipitations of high aspect ratio are often observed too (marked with red circle).

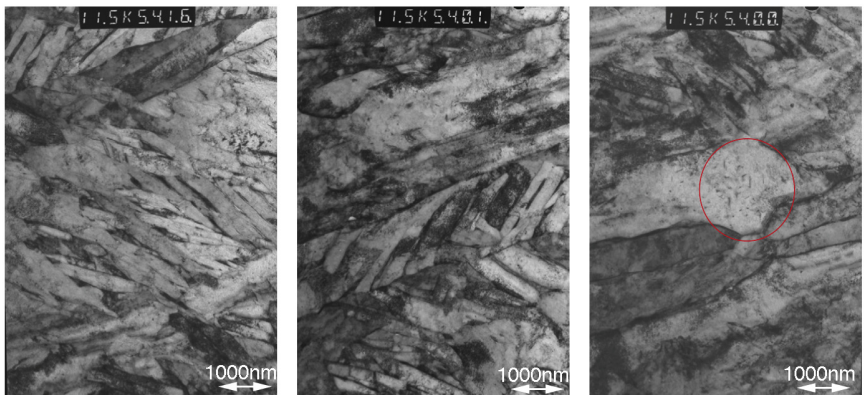

Figure 5.8: Microstructure of the PaQ state in the TEM, general overview. Red circle: auto-tempered martensite

The dark films have been identified by SAD as cementite, fig. 5.9 shows this in bright-field and dark-field, as well as the ED pattern.

TEM bright-field, dark-field and ED images of a region with the precipitations mentioned above (fig. 5.8, red circle) are shown in fig. 5.10. SAD revealed that it is cementite as well. Due to the two different orientations in the matrix (of three possible ones), it can be identified as martensite with precipitated cementite.

A part of a austenite grain boundary where no cementite has been found is presented in fig. 5.11. Precipitations that are found in this area (marked with arrows) have a crystal structure different from the one of cementite

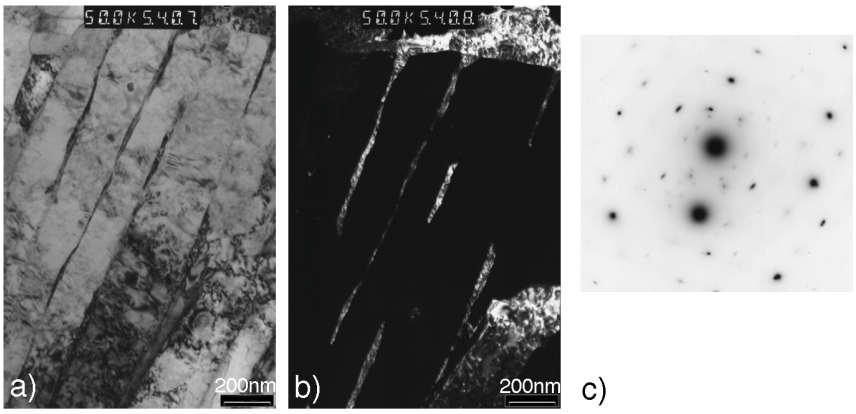

Figure 5.9: Lath boundaries with films in the TEM (BF a), DF b), ED pattern c))

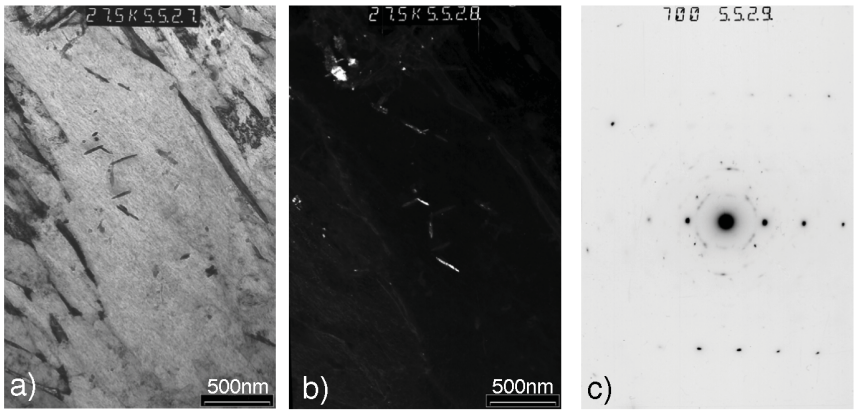

Figure 5.10: A region with precipitations of cementite in the TEM (BF a), DF b), ED pattern c))

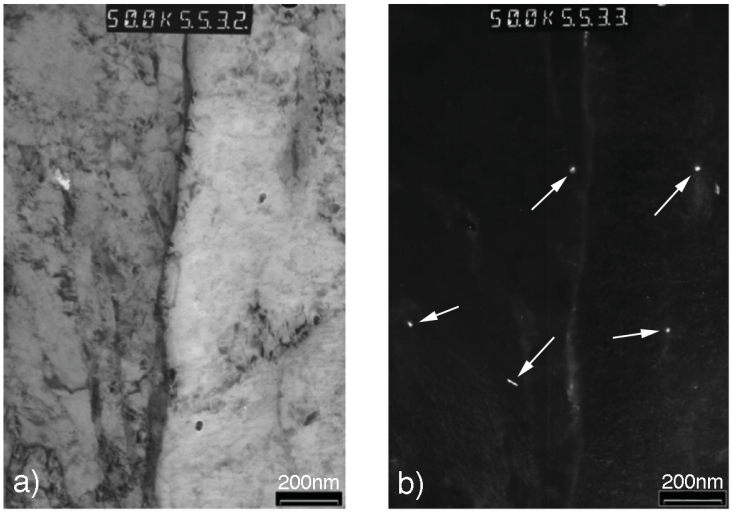

Figure 5.11: A region with precipitations in the TEM (BF a), DF b))

(imaged in dark-field). They can be found majorly in intragranular regions.

A typical distribution of these precipitations is shown in fig. 5.12. They can be divided by size and position into coarser ones (30nm - 50nm) at intragranular positions and smaller ones (7nm - 10nm) at GB and lath boundaries. The dark-field image proofs the identity of the crystal structures. The precipitations have been identified as mixed (Ti,Nb)C carbides[1] by ED (fig. 5.13).

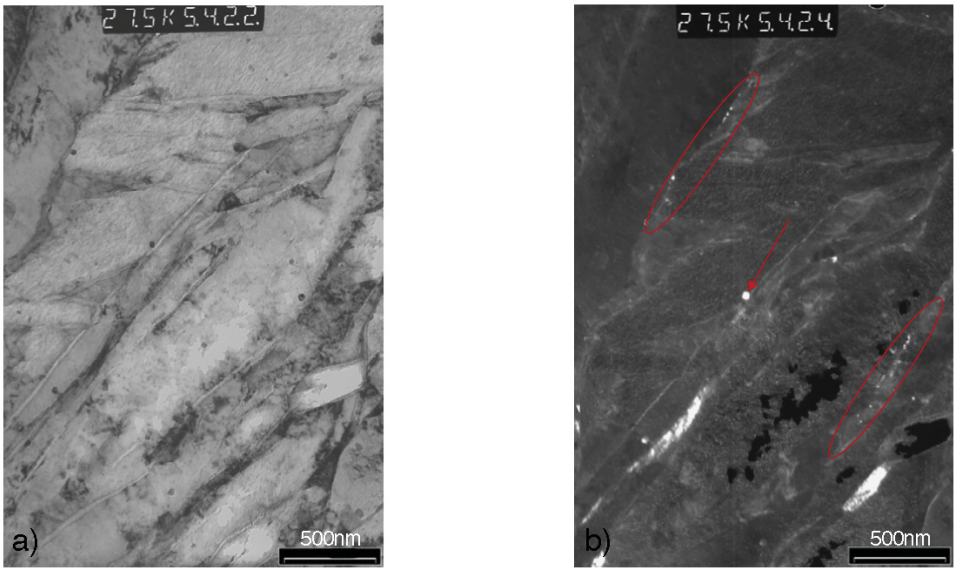

Figure 5.12: A region with intragranular (red arrows) and interfacial (red circles) precipitations in the TEM (BF a), DF b))

Since these precipitations are rather small, it is not really possible to analyze them by EDX, or get high resolved images, as long as they are inside the bulk material. Therefore, the precipitations have been extracted, using carbon extraction replicas. This technique confines the placement of the precipitations in the material. An overview of the extracted precipitations in BF is given in fig. 5.14. It shows the lath-shaped structure of the steel with

[1] An inclusion of N is possible

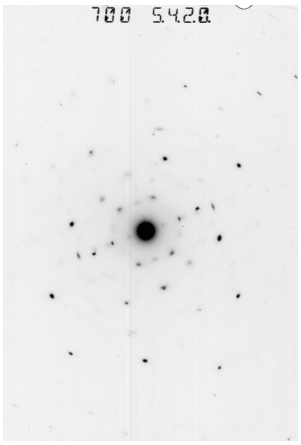

Figure 5.13: ED pattern of one of the precipitations (with matrix) in (5.12)

a quite homogenous distribution of the intercrystalline precipitations. With the replica, only the fine intercrystalline precipitations have been extracted, that is the reason why the cementite at the lath boundaries and GB does not appear. The imprint of a former austenite GB is marked with red arrows.

Details of fig. 5.14 are shown in fig. 5.15.

The precipitations are 20nm-50nm in size and have a spherical or cubic shape with blunted edges. The EDX spectra of four particles at different sites (fig. 5.16), show the qualitative chemical composition. It has been observed that if Ti is dominating, the particles have rather cubic shape and the more Nb is incorporated, the blunter the precipitations get. In particles, where Nb is dominating, also an incorporation of Mo and V can be found. Fig. 5.17 compares the analysis of a particle with a reference spot, where the contribution of the Cu grid where the replica is placed on can be seen.

Since the limit for the extraction of particles in steel is somewhat around 10nm, it was quite difficult to capture the small particle fraction. Nevertheless, it was possible to extract at least some, sized about 10-15nm for investigations in a HRTEM. Fig. 5.18 displays a particle in high resolution

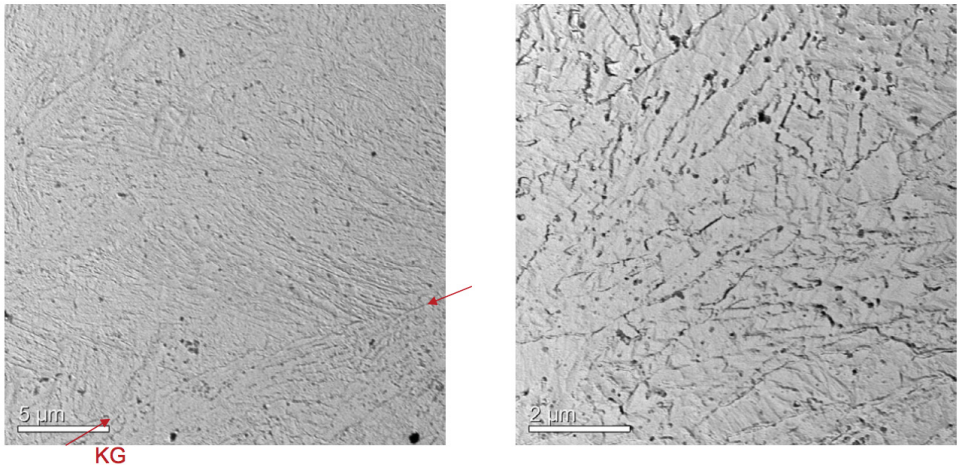

Figure 5.14: Overview of the extracted precipitations in two different magnifications, a former austenite GB is marked with red arrows

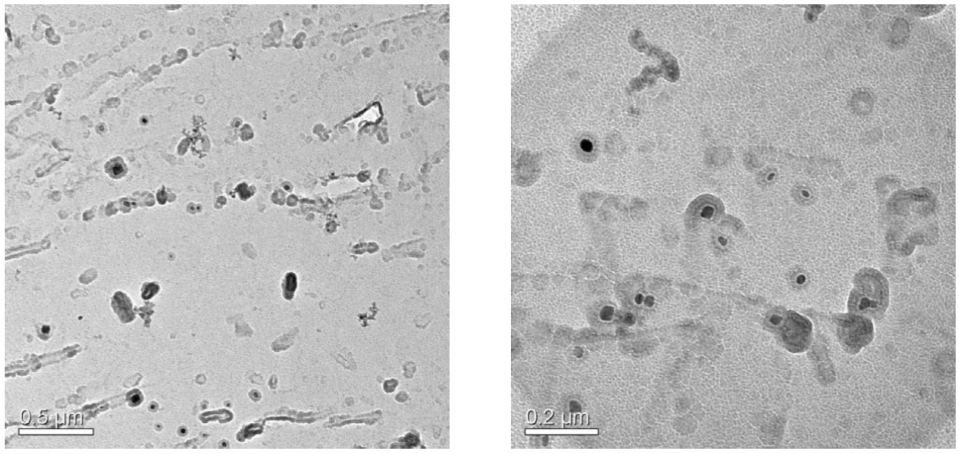

Figure 5.15: Overview of the extracted precipitations in two different magnifications

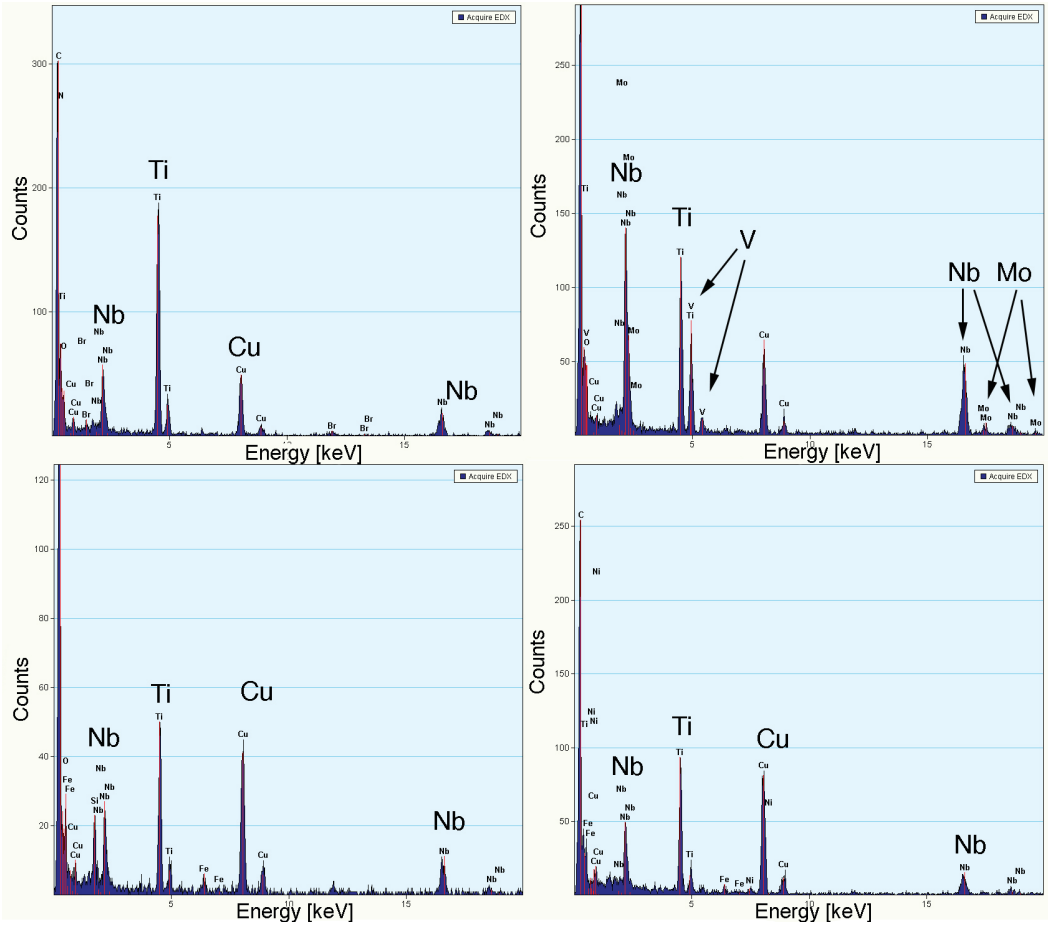

Figure 5.16: EDX spectra of four different particles at different sites

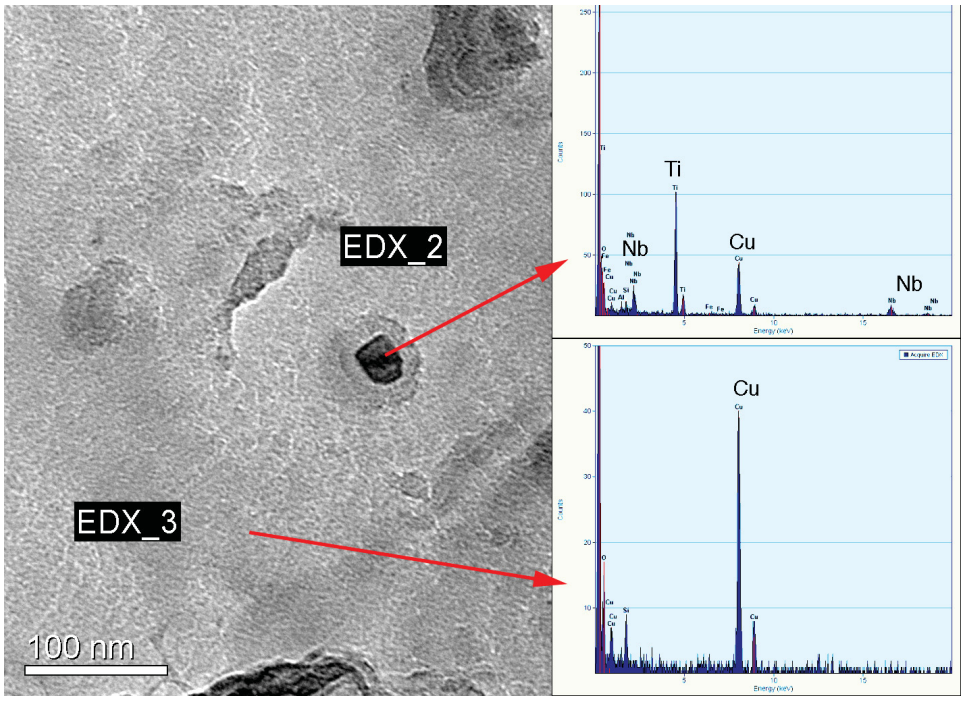

Figure 5.17: Comparison of a EDX spectrum of a particle to a reference spot

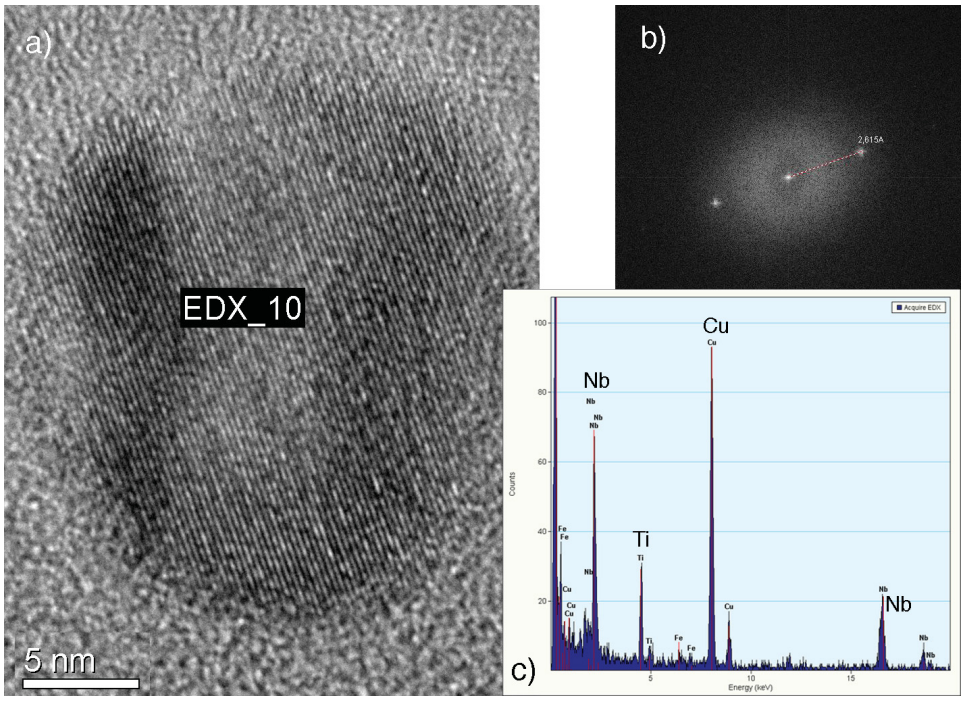

Figure 5.18: High resolution image of a particle a) with corresponding ED pattern b) and EDX spectrum c)

with its EDX spectrum and ED pattern. Precipitations of this type have been observed regularly, with spherical morphology and a homogenous distribution. The EDX spectrum shows Ti, Nb and C with small parts of Mo and V. The Cu peak again comes from the grid. The analysis of the diffraction pattern confirms, that it is $(Nb, Ti)_2C$ or $(Nb, Ti)C$. What stands out is, that the particle has a Nb:Ti ratio of around 2:1. Fig. 5.19 shows another particle on a different site, size and chemistry differ from the precipitation in fig. 5.18. The chemical composition is closer to 50nm sized particles than to the frequently observed smaller ones, containing Mo and V.

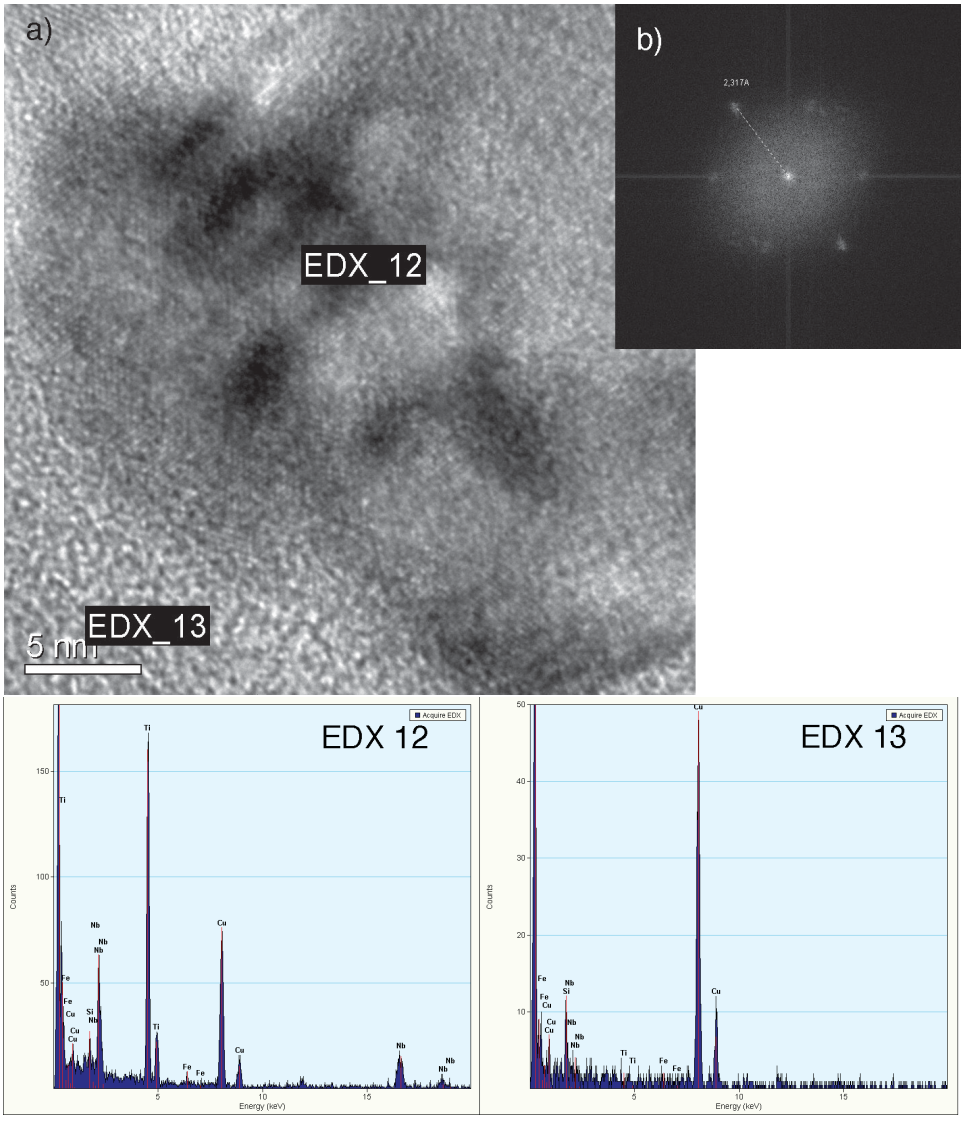

Figure 5.19: High resolution image of a particle a) with corresponding EDX spectrum (EDX 12,13) and ED pattern b)

5.3.4 The Material on an Atomic Scale

Once the constituents of the material are known, the question that is still unanswered is the distribution of the individual elements in the steel that are not boned and the partition of the elements in the precipitations. These questions can be answered using atom probe techniques, displaying the elemental distributions in the tomographic reconstructions and concentration profiles. In the reconstructions, all dimensions are displayed in nm.

In the mass spectrum, nearly all peaks have been allocated. The mass/charge spectrum of one run, containing 19Mio atoms is displayed in fig. 5.20.

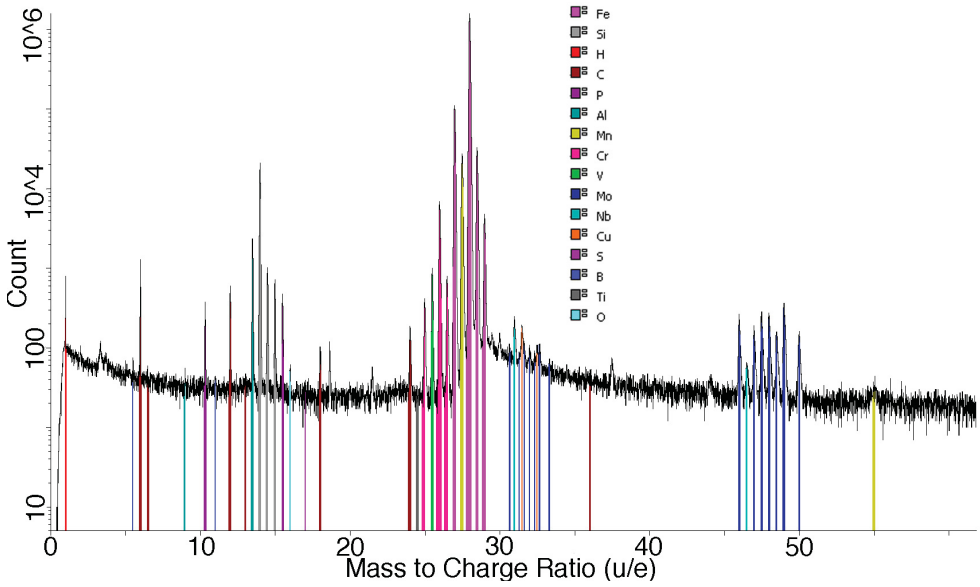

Figure 5.20: 3DAP mass/charge spectrum containing 19Mio atoms

General Distribution of the Elements

As expected from the mechanisms of the bainitic transformation, all elements except carbon are uniformly distributed throughout the bainitic laths. This is consistent with published atom probe investigations on bainitic structures [Bha81a, HBS82, SSB90, PBMB04, CM07]. In fig. 5.21 a measurement of almost 200nm shows the element‘s distributions. It shows a U-shaped diffusion profile of C, that is seen to be a result of the bainitic reaction, the regions of higher carbon content are seen as possible lath interfaces. The concentration of the C is around twice as high at these sites than in the minimum (0,06at%) in the middle. Segregations of any kind, besides C have not been observed in the PaQ condition. This can be seen in the concentration profiles in fig. 5.22, where the microalloying elements, Al and P are displayed. Mn that is for the sake of clarity not displayed here, shows the same behavior. If we take a look at C and P, we see that C has been diffusing, as mentioned above, while P is distributed uniformly.

The distribution of the boron (fig. 5.24) also shows no significant aberration from an uniform distribution, the fluctuations are the result of the concentration in the ppm range.

Further measurements have suggested that the local chemical composition is determined by the distribution of C. Unfortunately, these runs were much shorter than the one in fig. 5.21, so a concentration profile within a large distance could not be obtained (figs. 5.25, 5.26). The main difference is, that the observed enrichment is much higher in these measurements (1:6 and 1:12). In fig. 5.25 a small cluster of C can also be seen about 5nm away from the C-enriched area. In fig. 5.26 a very uneven distribution of C was present, with a ratio of about 1:3. This could be a former γ-GB as well, dividing a martensitic from a bainitic region, since a slight enrichment of B has been observed too (though not as clearly as in fig. 5.21), a reasonable statement would need a larger run. Here, the B seems to go with the C.

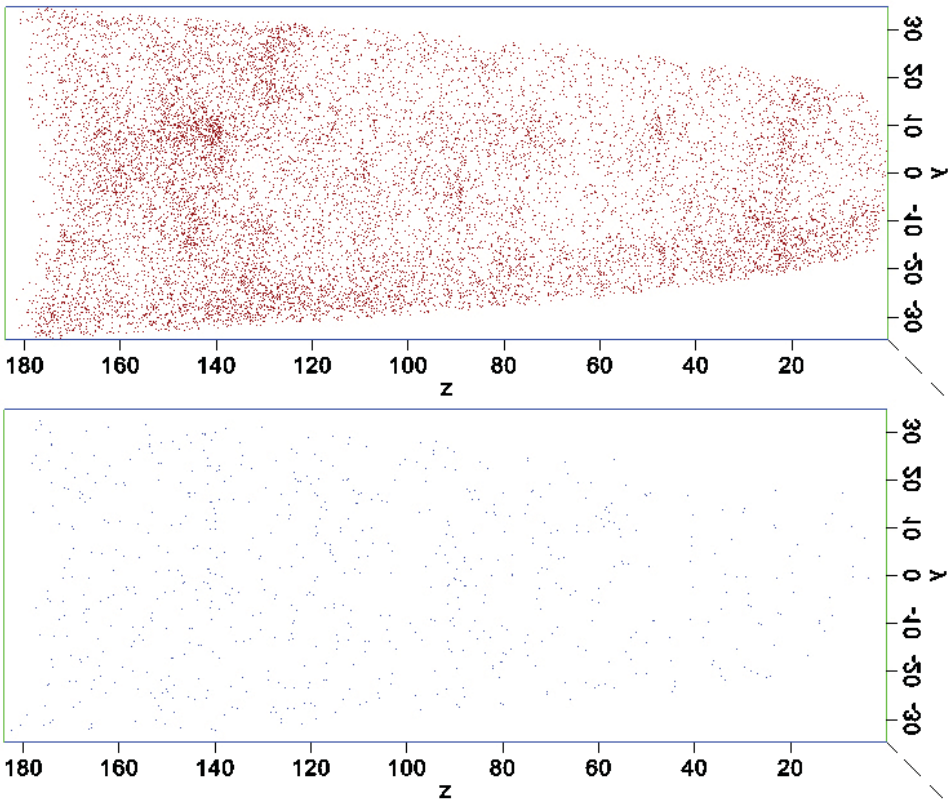

Figure 5.21: Reconstruction of a 3DAP measurement. C (red) B (blue), dimensions in nm

The lower region within the measurement is interpreted to be martensitic, since the carbon concentration quite accurately equals the average carbon concentration of the material. The carbon concentration at positions where enrichments have been observed has scattered in a wide range. The lowest measured concentration was 0,12at% (0,025wt%), the highest was 1,2at% (0,25wt%).

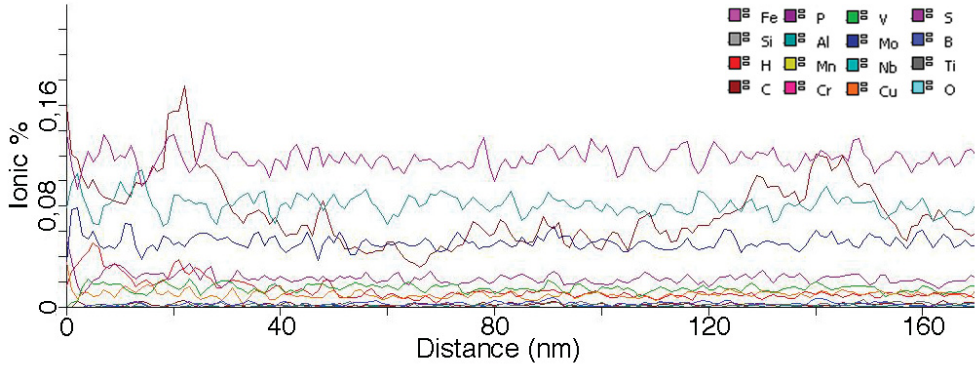

Figure 5.22: 3DAP measurement concentration profile in z direction

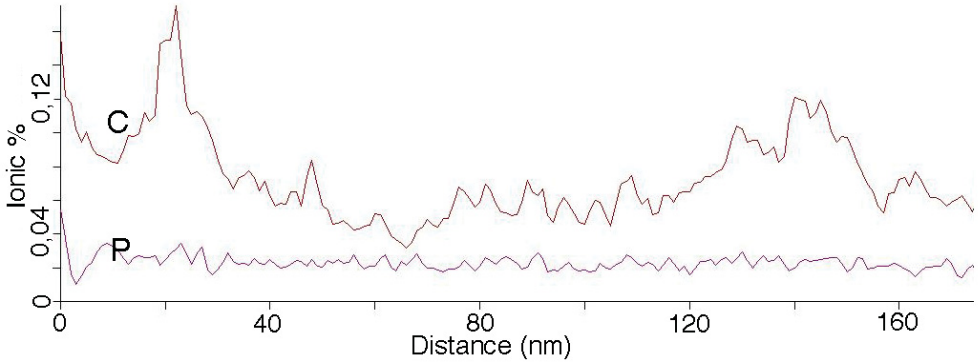

Figure 5.23: 3DAP measurement concentration profile of C and P in z direction

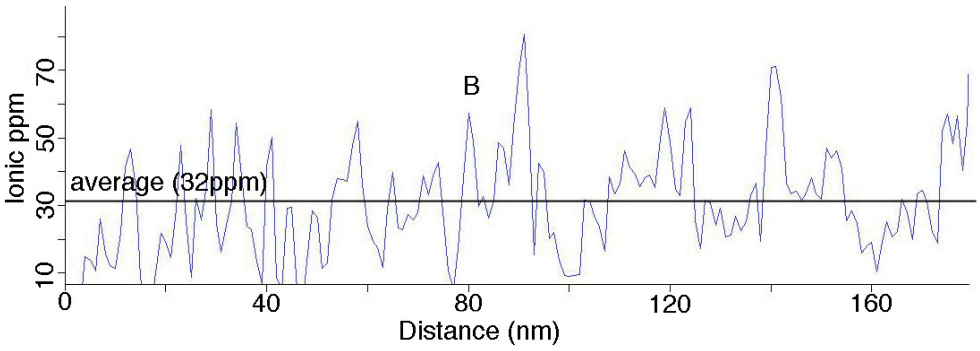

Figure 5.24: 3DAP measurement concentration profile of B in z direction

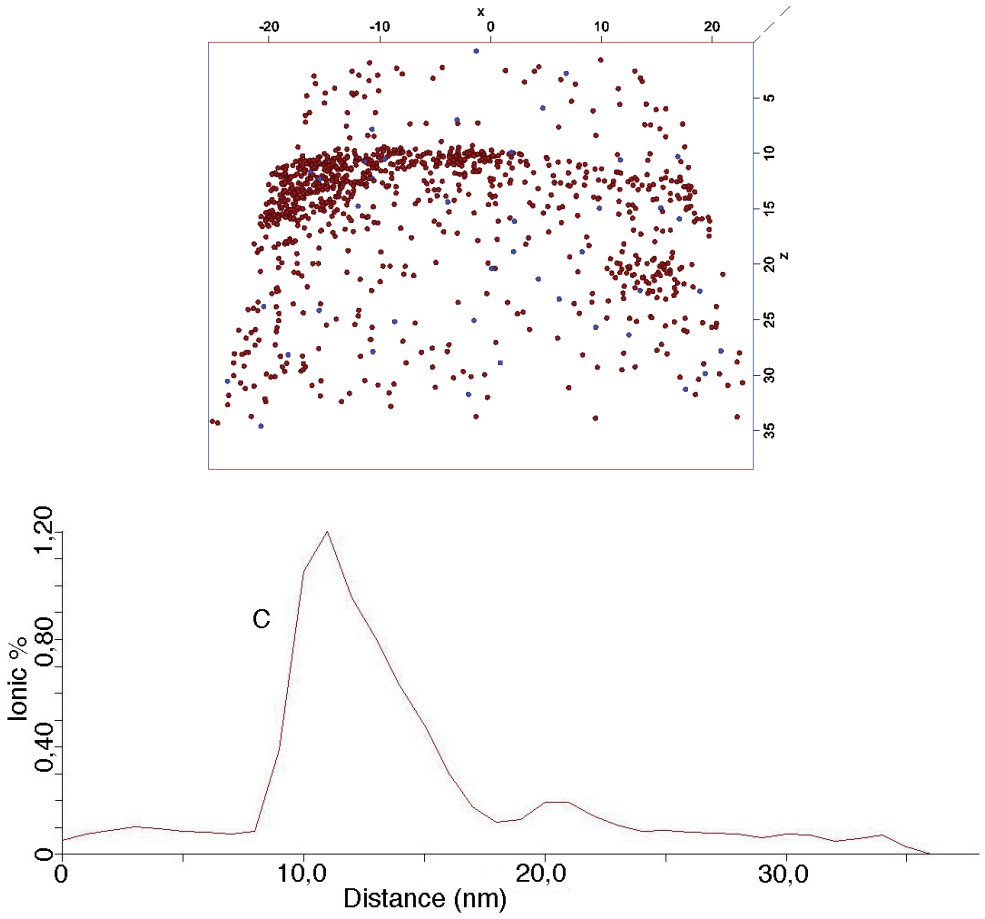

Figure 5.25: 3DAP measure containing an inhomogeneity, with 1D concentration profile in z direction, dimensions in nm

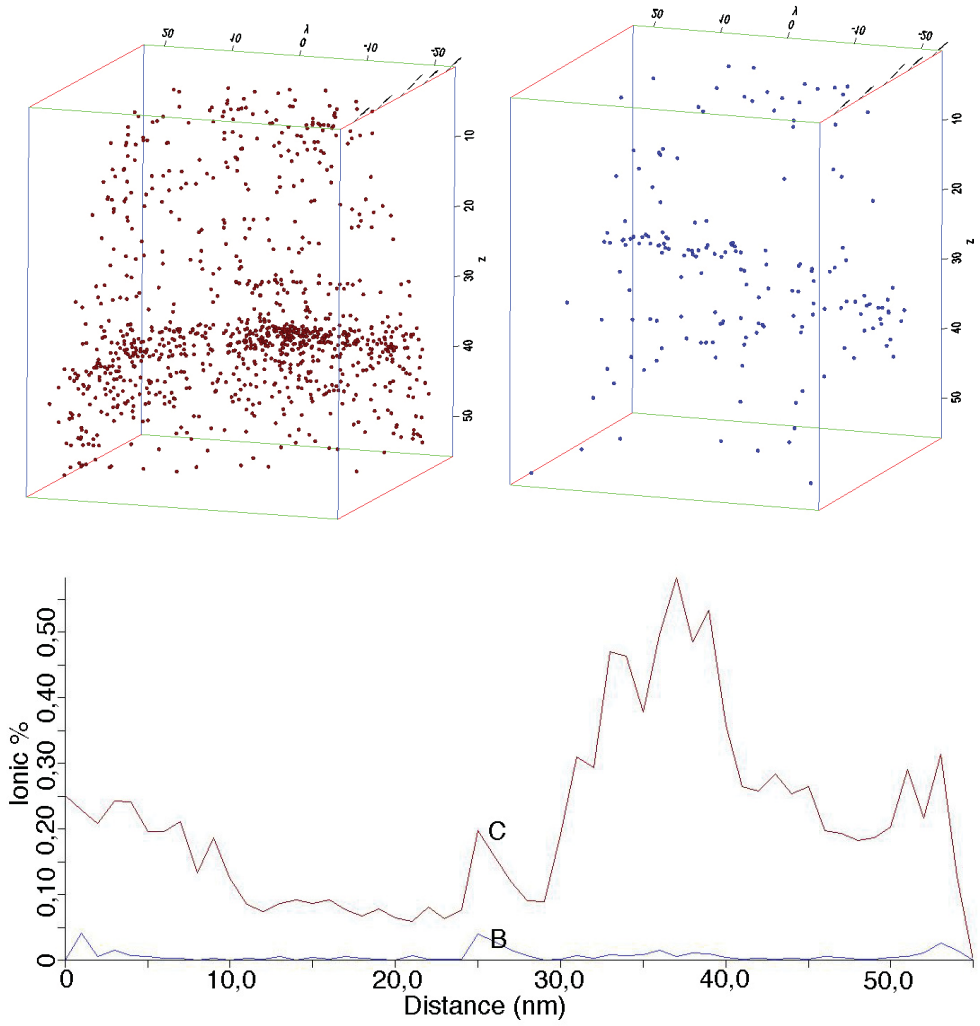

Figure 5.26: 3DAP measure containing an inhomogeneity, with 1D concentration profile in z direction, dimensions in nm

Partition of the Elements in the Cementite

Since low carbon steels have a very low volume fraction of carbides, only one position that is seen to be a carbide has been found during the measurements (fig. 5.27). It can not be distinguished clearly, if the carbide is one that is situated at some interface, or one of those that form in the martensite. Here, again, only C is the element that is not homogeneously distributed. This can be referred to the mechanism of the bainite reaction where no substitutional diffusion is going on.

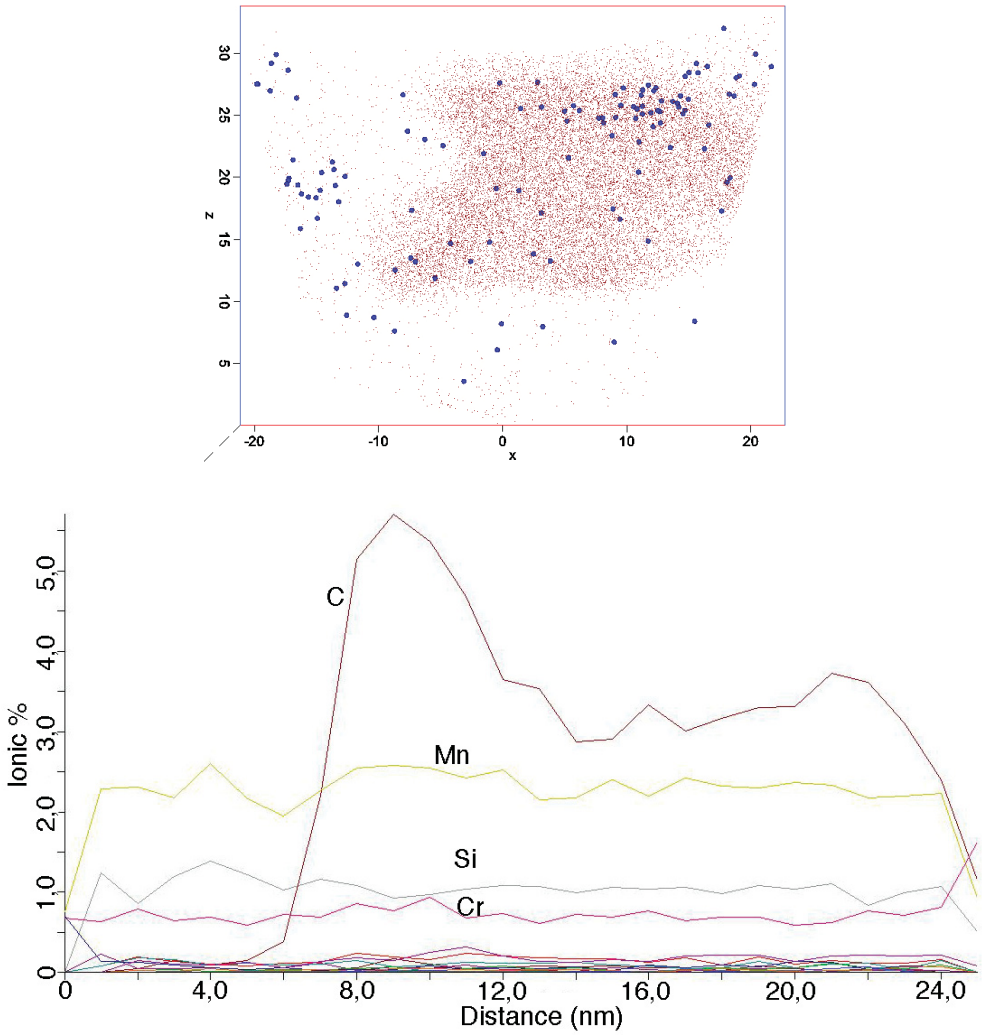

Figure 5.27: 3DAP reconstruction of a carbide with corresponding 1D concentration profile in z-direction. C (red) B (blue), dimensions in nm

Local Enrichment of B

In the case of the investigated material, the distribution of B plays a key role. It is desired to be at the γ-GB and not bound to N in form of BN. B that is found intragranular has no effect. In one measurement, what is seen to be a crossing of a former γ-GB with a lath boundary has been found (fig. 5.28). The orientation of the B-enriched region equals the orientation of the austenite grain boundaries with respect to the axis of the prepared needles for the atom probe investigations. The concentration profile of this measurement clearly shows a tenfold enrichment of B at these sites.

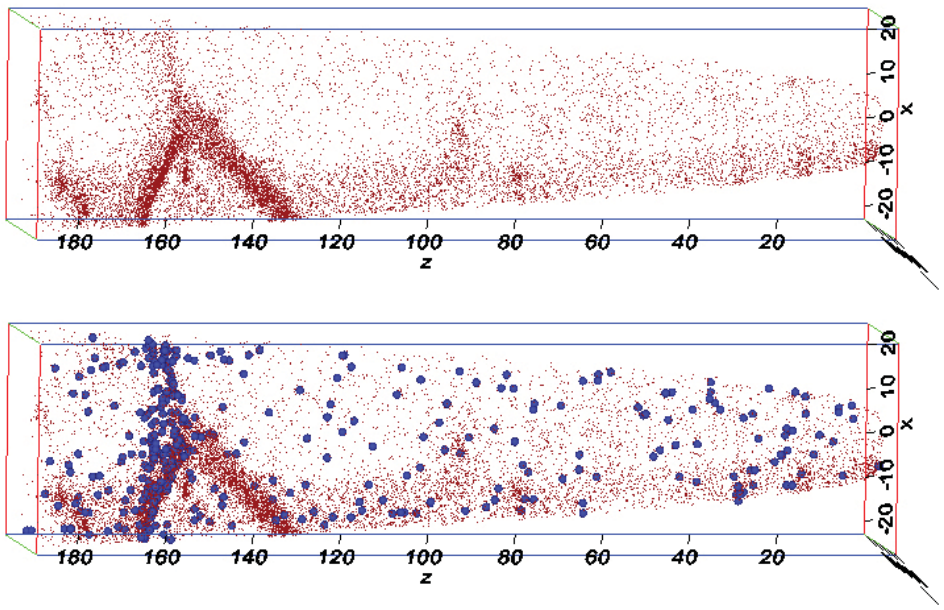

Figure 5.28: 3DAP reconstruction of a possible former austenite grain boundary intersected by a lath boundary. Dimensions in nm, C (red), B (blue)

If we quantitatively analyze this result, 179 B atoms were found at this site in a circular area of 40nm diameter. The detector efficiency is approx.

1/3, so the presence of 519 B atoms has to be expected. This equates to $6,86 \cdot 10^{-7} mol/m^2$ or $0,4 atoms/nm^2$. If we take the austenite GB-area of $319000 m^2/m^3$ this amounts to 1,55ppm(atomic) boron that are found at the grain boundaries. The amount measured inside the bulk, in the run behind fig. 5.21 is 32ppm(atomic). This leads to the conclusion that the solubility of B in the steel can not measurably be influenced by the amount of austenite grain boundaries. The activity of B in the material just defines the chemical potential for the segregation. This stands in contrast to existing opinions on that topic, for example [BS93], where it is speculated that the amount of boron alloying has to be dependent on the amount of austenite grain boundaries per unit volume.

What further stands out, is the uneven distribution of the C at the different interfaces. The generally higher concentration of C on the right side of the needle is an artifact of the measurement.

Since this was a quite long measurement, the carbon concentration inside the lath has been analyzed and found to be 0,07at%.

5.3.5 Enrichment of Specific Elements in the Middle Segregation Zone

To analyze the middle segregation zone, atom probe specimens, located at this site, have been prepared. The middle segregation zone can easily be found using SIM, since the chemical difference produces a strong contrast. Unfortunately, only one sample led to an analyzable data set. The spatial distributions of some of the elements analyzed are displayed in fig. 5.29. The measurement was performed in laser mode, using a laser energy of 0,3nJ, at a target evaporation rate of 0,5%.

In the specific case of the middle segregation, the measurement of the composition is more important, the overall composition is displayed in table 5.2. It has to be annotated, that virtually all peaks in the mass spectrum could be allocated. The as Ni defined range could also be CrC, and the as Cu defined range VC, complex ions that form during laser-enhanced field evaporation. If this is regarded, the segregation ratio of C is 0,87 (0,28at% C).

From the elements, that are not present in the overall chemical analysis of the trial plate, Ca has been found in an extender amount, probably remaining from a Ca treatment of the steel for desulphurication. Since this sample was produced without a low-energy clean-up step, Ga contamination is also present in a non negligible amount. Also a peak, that is suspected to be from a alkaline or earth alkaline metal, probably Sr is present.

For the elements found in the provided chemical analysis, it is possible to define a segregation ratio. Though most elements do not segregate significantly, elevated amounts of Nb, Ti and S have been found. While Nb was found enriched in a ratio of around 2,5, Ti was found to be enriched sixfold and S even elevenfold. This is displayed in Fig. 5.30.

Weather Al is not present in the segregation zone or not can not really

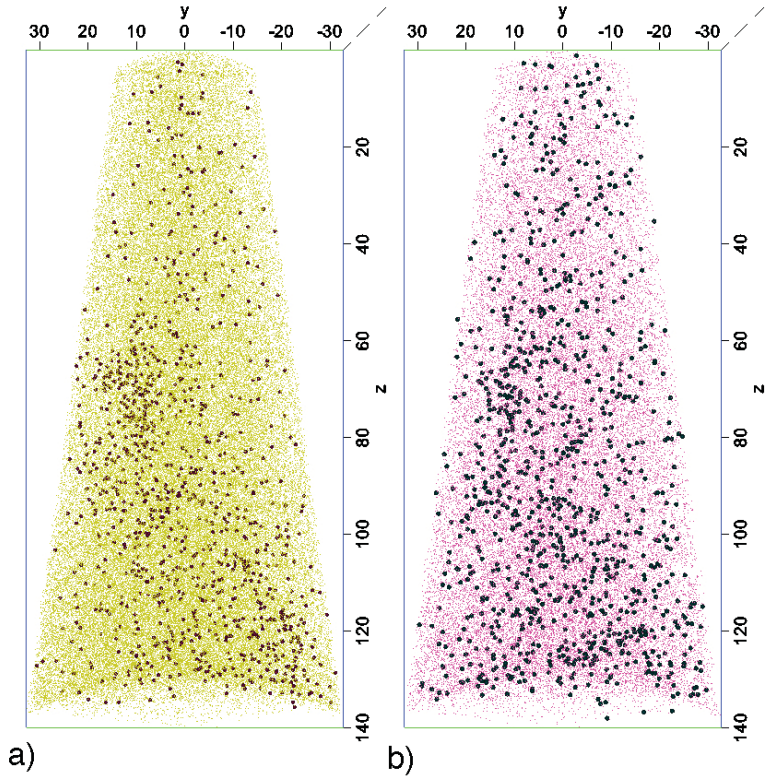

Figure 5.29: Reconstruction of the LEAP measured volume of the middle segregation zone. Mn (dots) and C (spheres) distribution (a) and Cr (dots) and Ti (spheres) distribution (b), dimensions in nm

be answered using atom probe techniques, especially when using laser evaporation. The low evaporation field of Al makes it thinkable that the Al also evaporates in between the laser pulses, as discussed also for Ga [TLL$^+$07] . The detection of H comes from residual H in the measurement chamber.

Ion Type	Composition [at%]	Ion Type	Composition [at%]
Fe	94,5	H	1,02
Si	0,75	Nb	0,0459
C	0,199	P	0,0210
Al	0,0239	Mn	2,180
Cr	0,465	V	0,0415
Cu	0,0389	Ni	0,0401
Co	0,00200	Ti	0,0741
S	0,0140	Ga	0,4780
Ca	0,0142	Mo	0,105
Sr	0,0205		

Table 5.2: Composition for the laser assisted LEAP measurement of the middle segregation zone

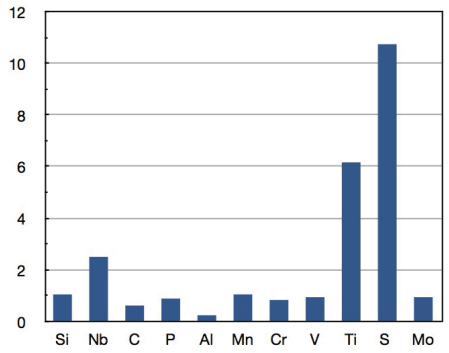

Figure 5.30: Relative enrichments of elements in the middle segregation zone

5.4 Austenite Microstructure after Static Recrystallization

After static recrystallization, the austenite microstructure differs strongly from the pancaked austenite, as can be seen in fig. 5.31. The grains are equiaxed, with a grain size of around $20\mu m$. Single grains with double or threefold size are also observed. If we compare the structure to the pancaked austenite, there is no correlation.

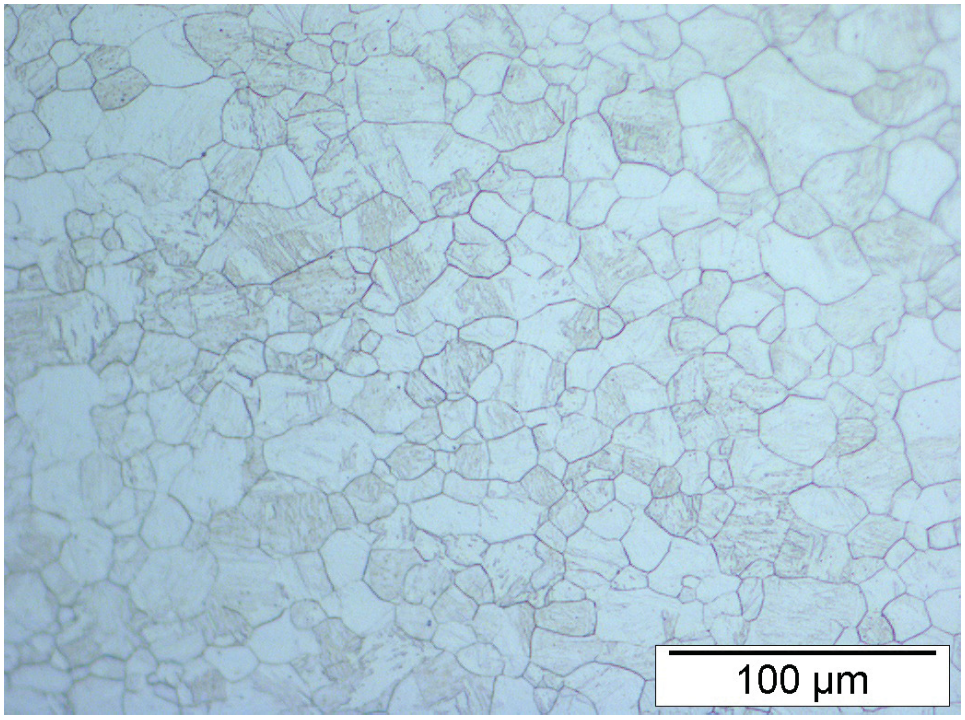

Figure 5.31: Resulting microstructure after static recrystallization, etched with Bechet-Beaujard‘s etchant

5.5 Polygonal Austenite with DIC (PoQ)

To investigate the influence of the pancaking on the microstructure, a part of the material has been austenitized and quenched, this microstructure then strongly differs from the thermo-mechanical rolled one.

5.5.1 Mechanical Properties

The stress-strain diagrams can be seen in fig. 5.32, the impact toughness-temperature diagrams of the material are displayed in fig. 5.33, the corresponding values are listed in table. 5.3.

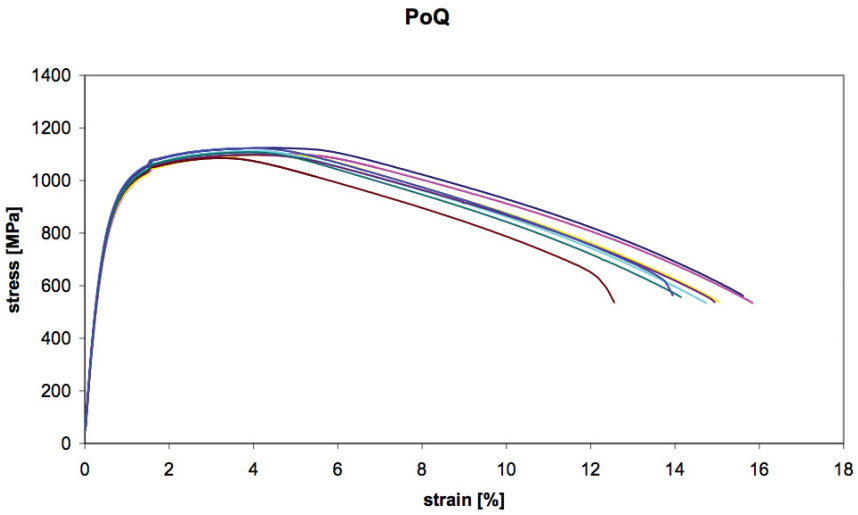

Figure 5.32: Stress-strain diagrams of the state PoQ

One of the features of the polygonal microstructure is, first of all, that the anisotropies in yield strength and UTS are gone. The longitudinal (L) and transverse (T) samples show quite the same values, specifically a YS of around 830MPa and a UTS of about 1100MPa. In the toughness-temperature

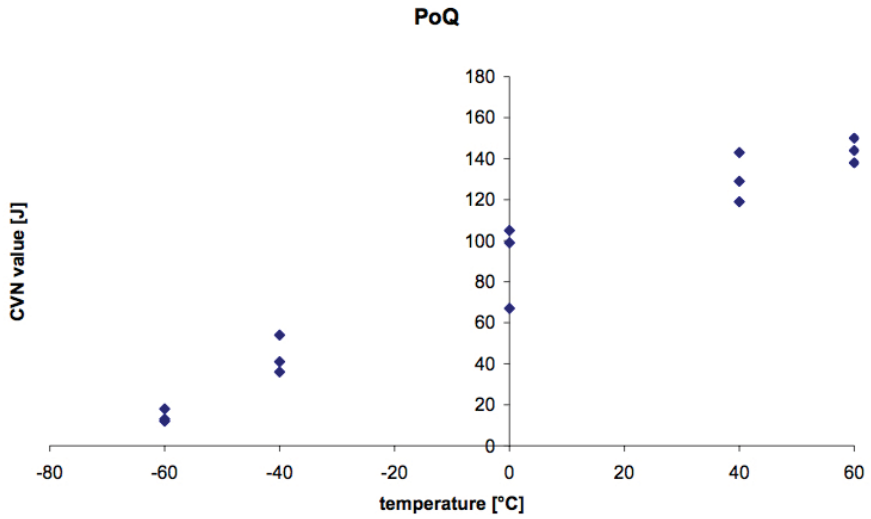

Figure 5.33: Impact toughness temperature diagrams of the state PoQ

diagram this material state also has no distinct transition temperature, it shows a slight slope, as the PaQ state, just with lower values at low temperatures. It would fulfill the requirements of toughness class J (CVN value of 27J for a 10mm sample) at a temperature of -40°C.

5.5.2 Microstructure

The PoQ state consists of the same three constituents as the comparable pancaked state, all three sometimes present within one former austenite grain (fig. 5.34). Again the contrast obtained by Nital is not sufficient to quantify the amounts of the individual constituents. In fig. 5.34 b), the three different constituents are marked with arrows. The constituent denoted "1" is seen to be bainitic ferrite, "2" is seen to be martensite and "3" the smaller, lath shaped martensite type. So, it pretty much equals the PaQ state, just with a polygonal γ-GB. It has to be denoted that the fraction of martensite is

UTS [MPa]	1106
YS [MPa]	831
A[%]	14,3
YR	0,75

Table 5.3: Mechanical properties of the PoQ state

higher than in the PaQ state.

In the SEM (fig. 5.35), the picture shows that the laths structure of the bainite seems to be coarser then in the pancaked state. In the martensitic regions there are also precipitated carbides (marked with arrow) are present, indicating that auto-tempering of the martensite occured.

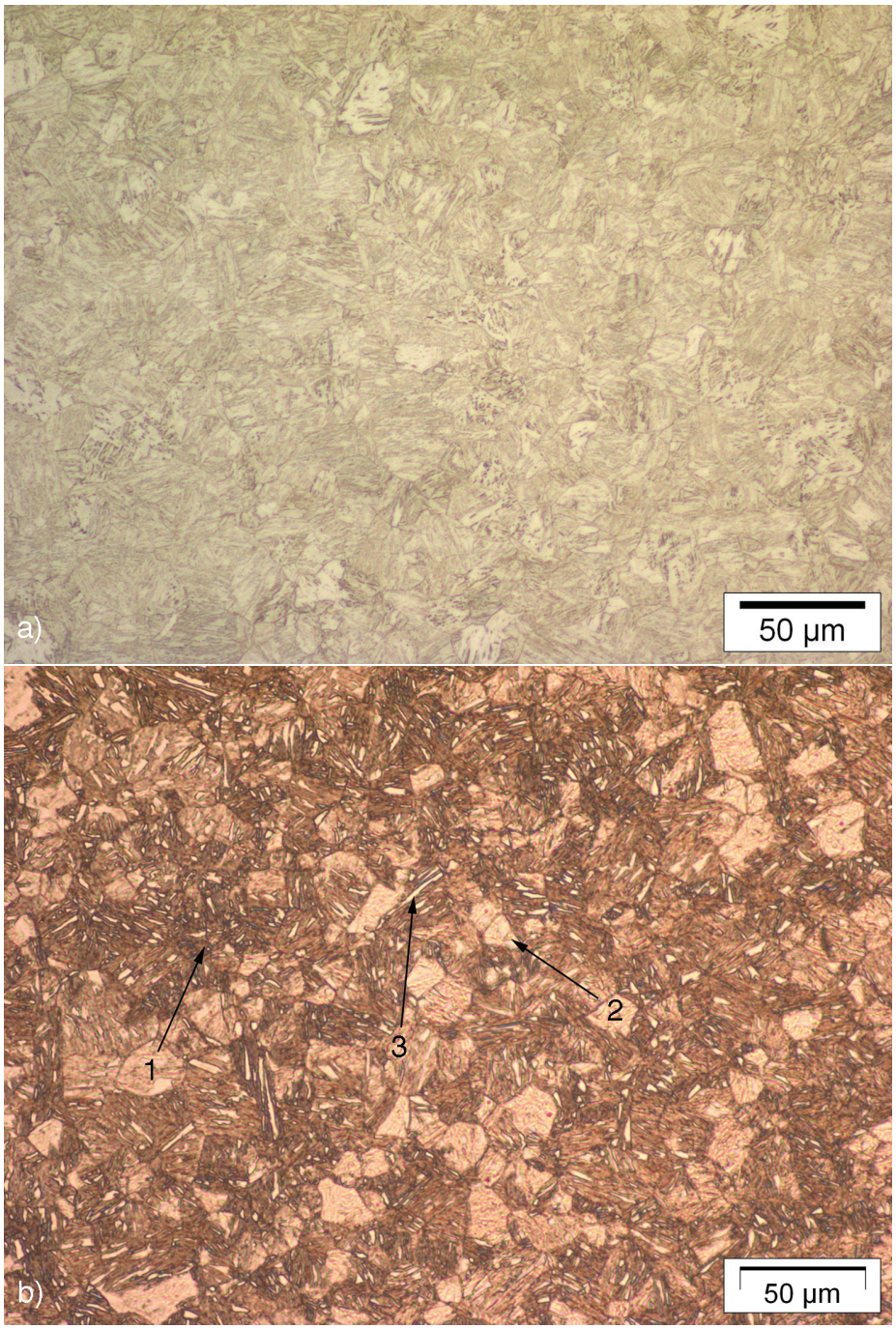

Figure 5.34: Microstructure of the PoQ state in the LM, etched with Nital a) and HFP b). "1" bainite, "2" blocky martensite, "3" lath-shaped martensite

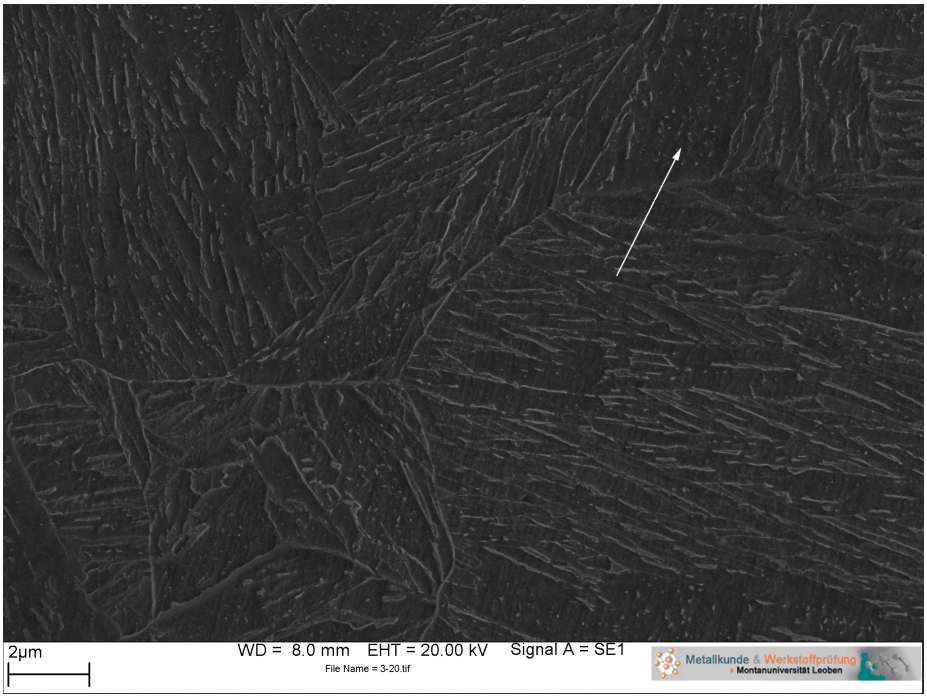

Figure 5.35: Microstructure of the PoQ state in the SEM, etched with Nital, arrow: auto tempered martensite

5.5.3 XRD Measurements of the Carbide Precipitation during Annealing

Since it is now clear what the constituents of the PaQ and the PoQ state are, the development of the material during annealing, with respect to a precipitation sequence of interest. Several samples have been annealed to temperatures from 200°C to 600°C and the peak broadening of the {110} peak of the iron has been measured. In principle, the broadening of the peak is caused by the instrument, crystallite shape and size, lattice defects (mainly dislocations) and lattice strain [Lan00]. In this work only the last two play a role, since just the {110} peak has been measured (vanishes instrumental influence) and the grain size and shape remain constant during the tempering. The decrease in broadening is then caused by the annihilation of lattice defects, whereas an increase is caused for example by the lattice distortion, coherent particles introduce.

The development of the FWHM over the tempering temperature of the peak is displayed in fig. 5.36. Up to 200°C virtually no difference to the unannealed material has been found, then the curve gets a constant, negative slope that is interrupted at 350°C where the FWHM starts to raise again. At 400°C the maximum FWHM has been found, then the curve gets back to its old slope, what is seen to be caused by the loss of coherency of the particles. It should be mentioned that the annealing temperatures have been divided by 50°C, so the overall maximum is not necessarily exactly at 400°C. The occurrence of a peak of the FWHM around 400°C is interpreted to be caused by a precipitation sequence, that distorts the lattice locally.

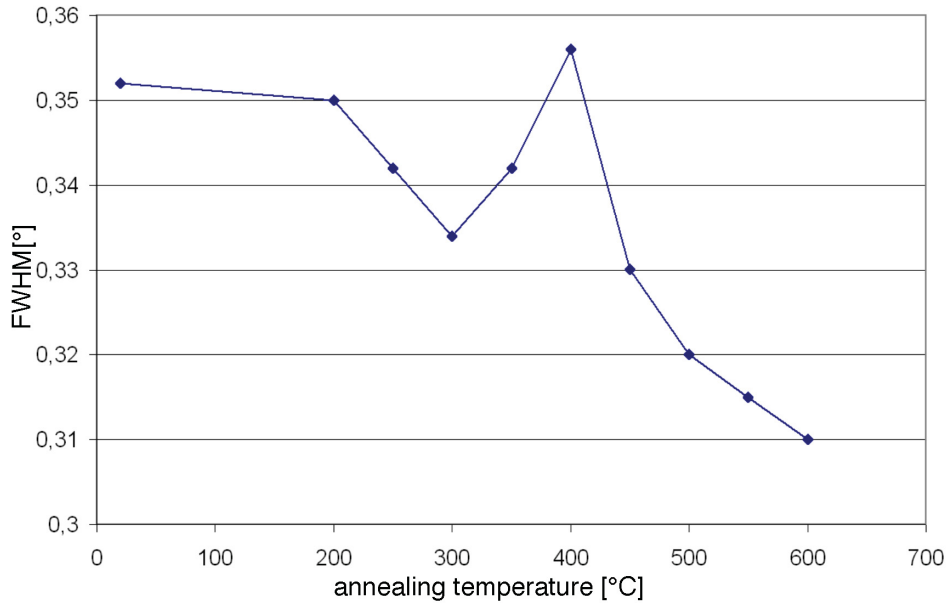

Figure 5.36: FWHM of the {110} iron peak of the material starting from the PaQ state against tempering temperature

5.6 Pancaked Austenite with DIC and Annealing (PaA)

In industrial practice, thermo-mechanical rolled heavy plates are frequently annealed, in order to lower the UTS, resulting in better cold-forming properties. These heat treatment has often caused vulnerability to an undesired fracture modes, where so-called "separations" form. These are fractures following the former austenite grain boundaries (see e.g. [Pet88, p.169-172]). In order to reveal possible reasons, annealed samples have been fabricated.

5.6.1 Mechanical Properties

The measured stress-strain diagrams for this state are depicted in fig. 5.37, the impact toughness-temperature diagrams of the material are presented in fig. 5.38, with the corresponding values quoted in table 5.4.

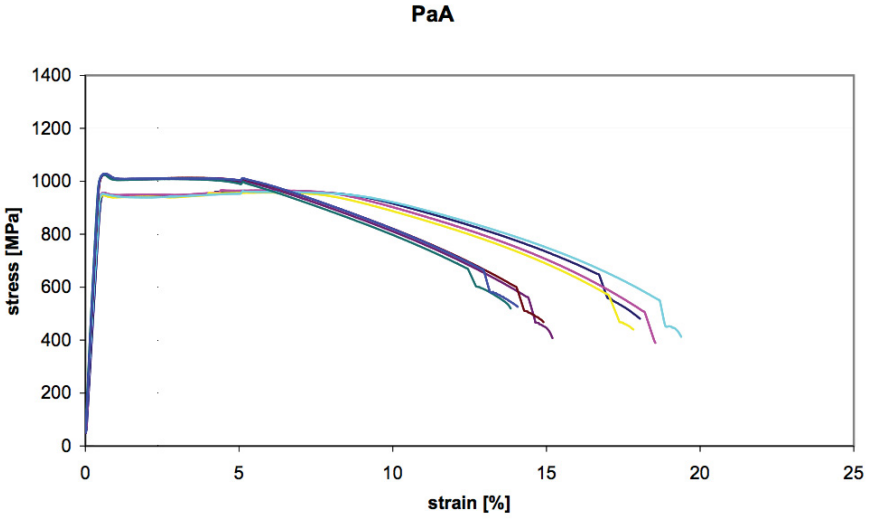

Figure 5.37: Stress-strain diagrams of the state PaA

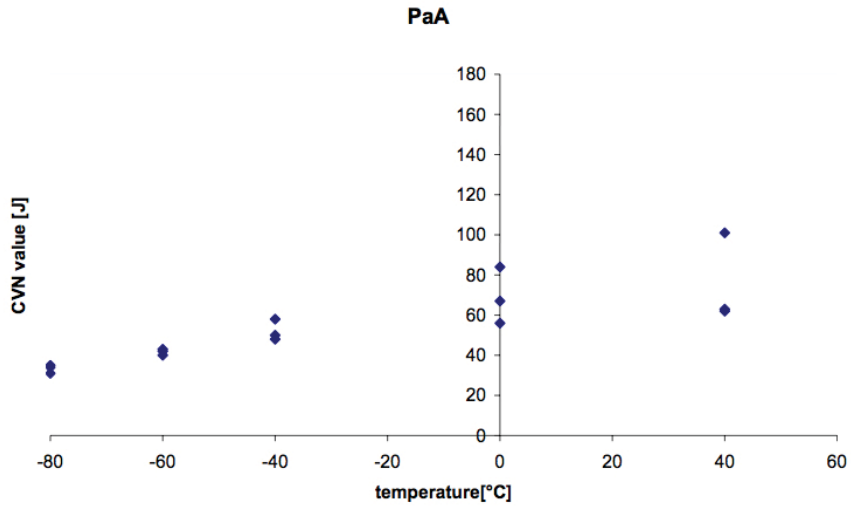

Figure 5.38: Impact toughness temperature diagrams of the state PaA

In this state, the anisotropy observed in the initial quenched state is still present, though the material has already undergone major changes. The L samples show a tensile strength of 960MPa the T samples 1030MPa. It is remarkable that the yield point is higher than the maximum tension in the plastic region. Since a yield point has not been observed in the quenched states, it is suspected that precipitation of small particles is accountable for that phenomenon.

The toughness-temperature diagrams of the PaA state show good values in the low-temperature range, but the CVN values do not raise with temperature as much as in the quenched samples. The 27J equivalent is reached already at -80°C. It has to be denoted that separations are broadening the transition region artificially.

	transverse	longitudinal
UTS [MPa]	1007	961
YS [MPa]	1026	952
A[%]	14,3	18,24
YR	1,02	0,99

Table 5.4: Mechanical properties of the PaA state

5.6.2 Microstructure

In the micrographs obtained with HFP, the difference to the quenched states is striking. It is already manifest on a macroscopic scale. The samples still show mirror finish, like the polished samples do, after they have been etched. This implies that the differences in chemical behavior between the individual phases have vanished. Nevertheless, a microstructure is observed, it is just very uniform (fig. 5.39 a)).

In the SEM (fig. 5.39 b)), it is much clearer, in which amount carbides are present and that they cover the majority of the former austenite grain boundaries (marked with arrows) as well as a large part of the lath boundaries. Though no clear evidence can be provided, it is assumed that the regions that have been etched less by the Nital are annealed martensite.

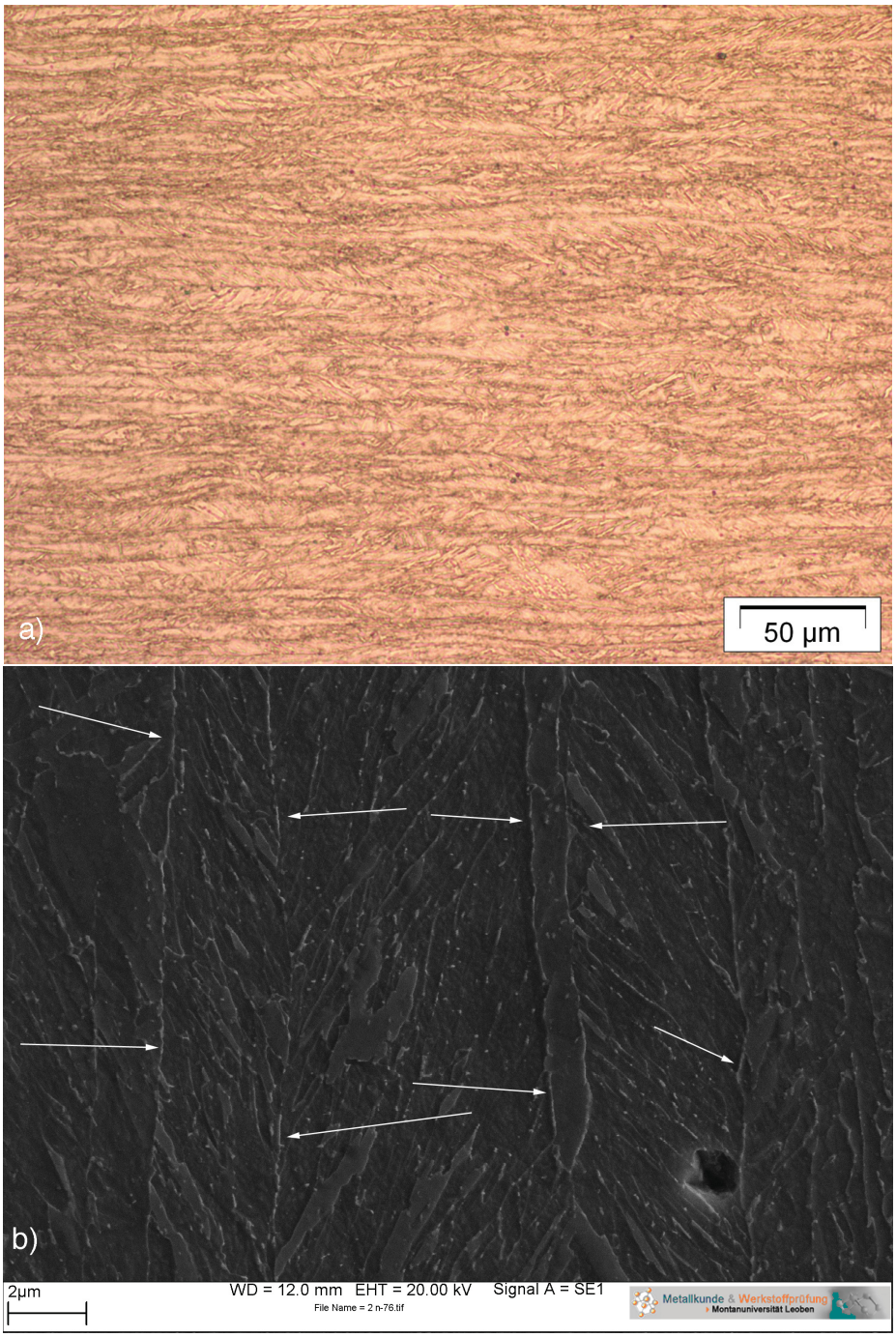

Figure 5.39: Microstructure of the PaA state in the LM, etched with HFP (a) and the SEM, etched with Nital (b). Arrows: former austenite grain boundaries

5.6.3 Submicrostructure

The annealed material shows a distinctly different appearance also in the sub-micron regime. The precipitations are here present in a much higher number density and size, leading to almost continuos films at the former austenite grain boundaries. Fig. 5.40 displays an overview of the material in the TEM, showing the lath shaped structure with a still high dislocation density in some regions and parts with a high intragranular precipitation density.

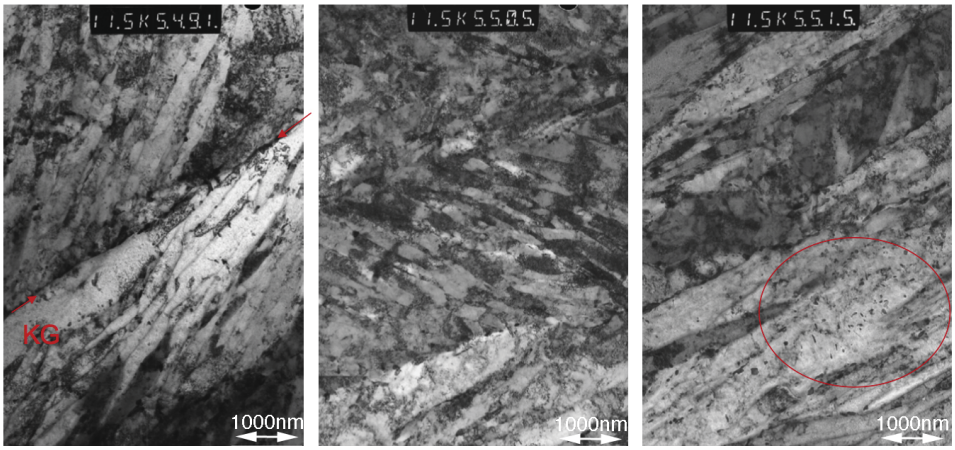

Figure 5.40: Submicrostructure of the PaA state in the TEM, general overview

Images with higher magnification show the decoration of the former austenite grain boundaries with cementite, identified by ED. Fig. 5.41 shows this in bright-field and dark-field, as well as the ED pattern.

The assumption that all the coarse precipitations found are cementite, has been checked on a different position. (fig. 5.42) The typical size of these precipitates ranges from 70 to 250nm, with regions of higher density and some of lower density.

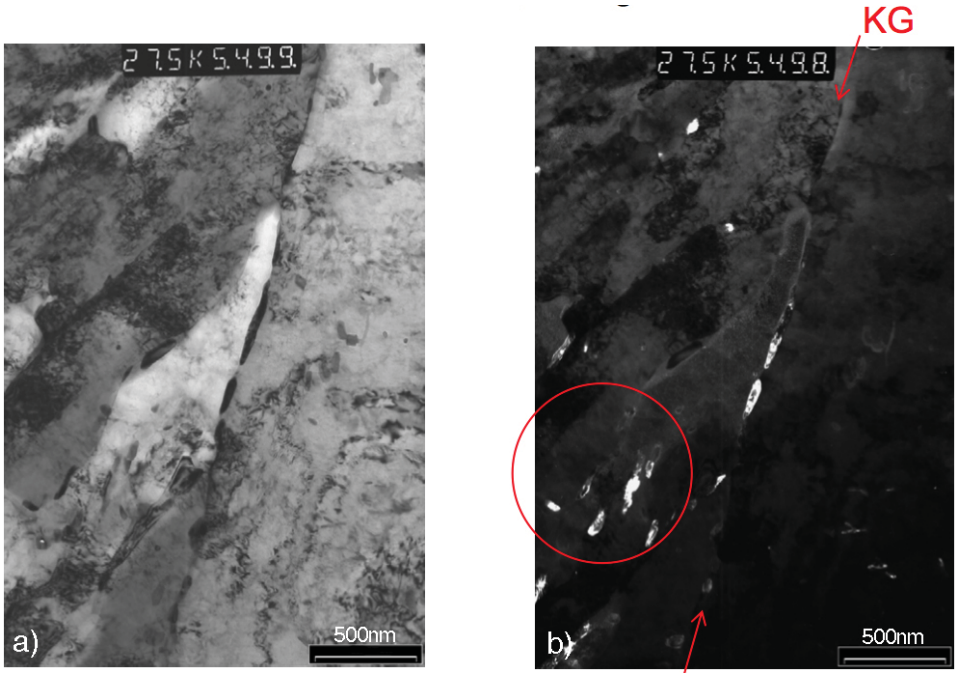

Figure 5.41: Grain (KG) and lath boundaries in the annealed structure with cementite films in the TEM (BF a), DF b))

Also regions can be found where lath boundaries are densely decorated with cementite, extending to a length from 100 - 500nm (fig. 5.43)

Furthermore in this state, finer, blunter precipitates have been found that have been identified as Nb(C,N) already described above. They seem to have undergone growth to some extent, since the measured sizes are from 20 - 70nm in this state, compared to 20 - 50nm before annealing. Fig. 5.44 shows bright-field and dark-field images of these precipitates. Since these precipitates are to stop recrystallization during rolling and do not contribute to the material‘s strength in a direct way, no emphasis has been placed on the characterization of these particles in the annealed state.

The most important change in the material during annealing is the raise

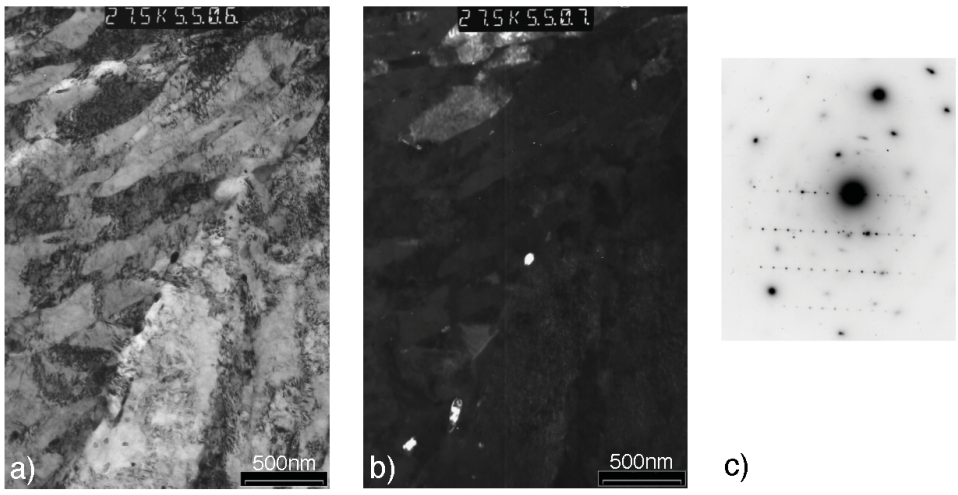

Figure 5.42: Grain and lath boundaries in the annealed structure with cementite films in the TEM (BF a), DF b), ED Pattern c))

in yield strength. Employing XRD measurements, hints have already been found that precipitation of some phase is accountable for this. The TEM investigations proved the presence of VC and/or V_6C_5 type precipitations, imaged in dark-field and bright-field in fig. 5.45.

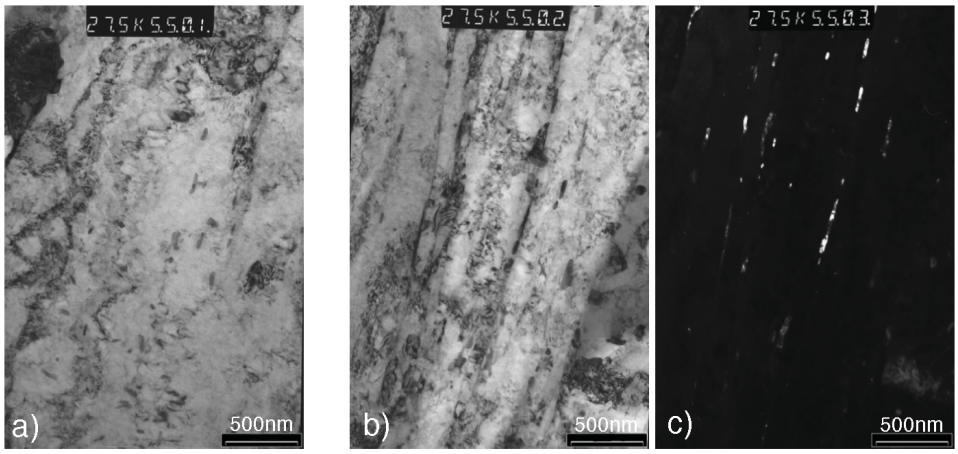

Figure 5.43: Grain and lath boundaries in the annealed structure with cementite films in the TEM (BF a),b), DF c))

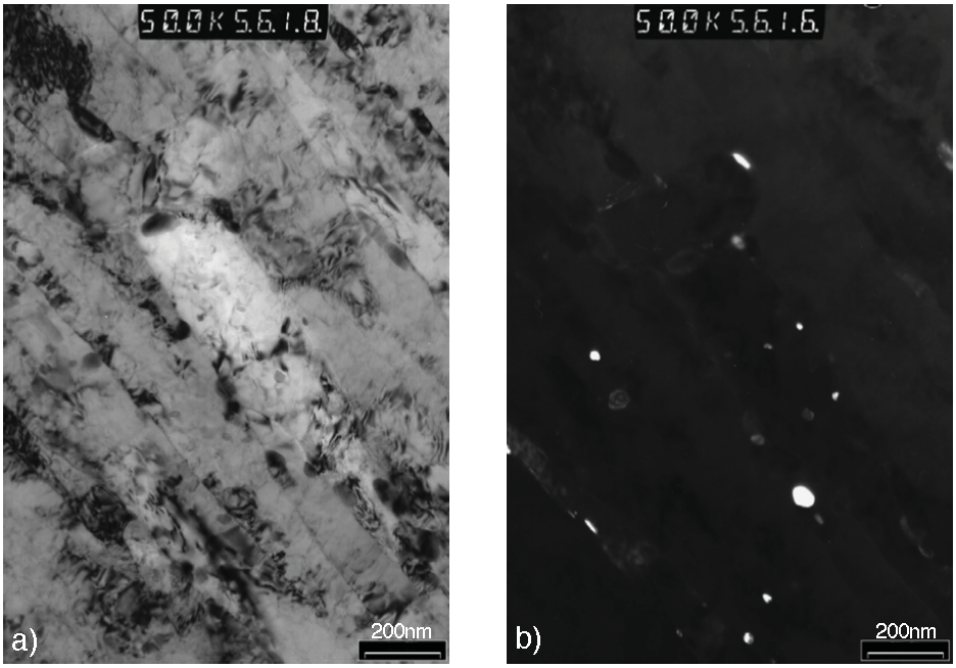

Figure 5.44: Nb(C,N) particles in the PaA state in the TEM (BF a), DF b))

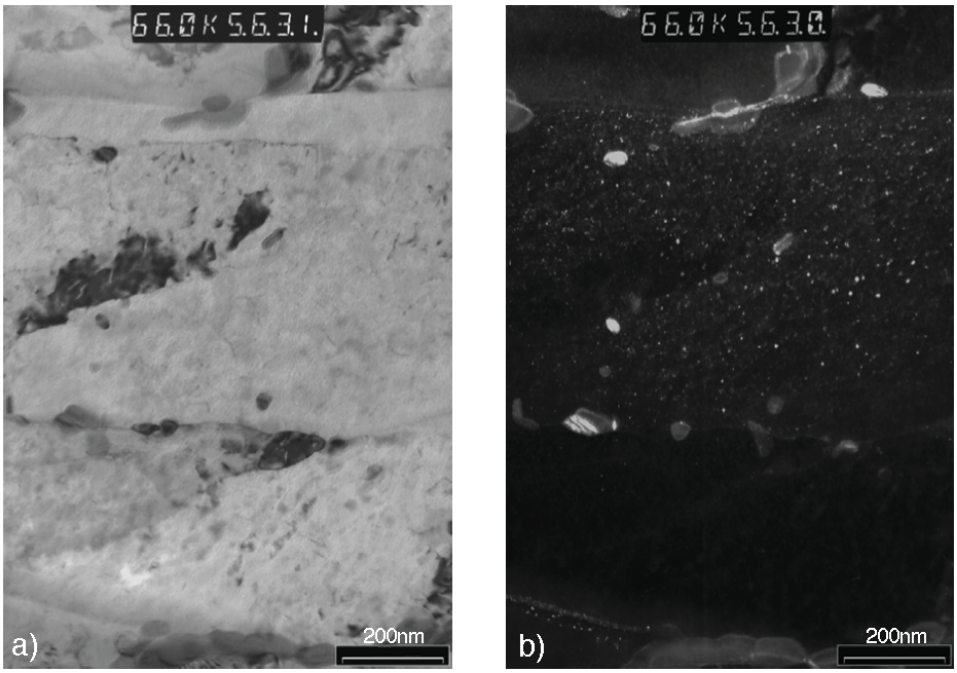

Figure 5.45: VC particles in the PaA state in the TEM (BF a), DF b))

5.6.4 The Material on an Atomic Scale

Though the limited time made it impossible to intensely investigate the annealed states, the measurements performed at least gave some information about possible segregations. VC particles have unfortunately not been detected. It has to be mentioned that this does not state anything about the frequentness of the VC precipitates, since the atom probe is an instrument that analyzes only very small volumes.

What has been found is the enrichment of various elements at one position inside a reconstructed volume. This is seen as to possibly be an interface. Analog regions have been contained in measurements of the quenched state. The difference is mainly that besides C, also P, B and other elements are enriched. Fig.5.46 shows the region of the atom probe reconstruction, where this enrichment has been found.

In fig. 5.47, shows a sixfold enrichment with respect to the surrounding area, the peak concentration is 0,6at%. A clear enrichment of Mn is also displayed (2at% compared to 1,4-1,6% away from this position). Si is rather uniformly distributed at a level of 0,8at%. This is slightly above the overall chemical composition of 0,69at%. The level of Cr in this measurement is around 0,3at%, this well below the alloying addition amount of 0,53at%.

The concentration profile for the elements that are contained in lower amounts in the alloy is displayed in fig. 5.48. First of all, the enrichment in P is very salient. Already the base level in this measurement is twice as high ($\approx$ 400ppm atomic) than the average P concentration (230ppm), with a peak concentration of around 1600ppm. Similar applies for B, with a local concentration up to 300ppm, compared to around 50ppm in the surrounding area. This measurement also displays a segregation of Nb. The width of segregation, which was estimated from the composition profiles, was 7 nm.

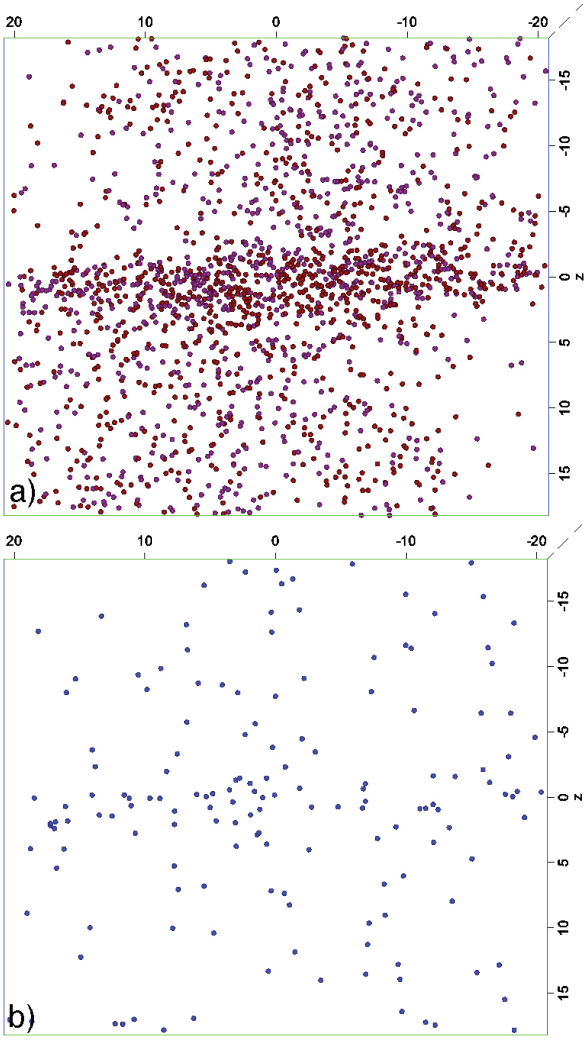

Figure 5.46: Spatial distribution of P (purple) and C (red) atoms (a) and B atoms (b) with a local enrichment. Dimensions in nm

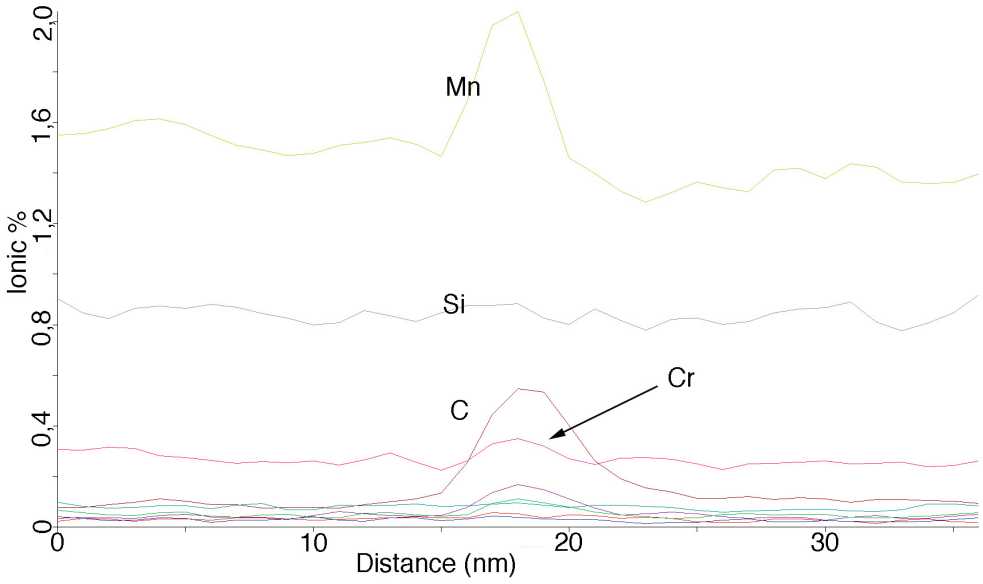

Figure 5.47: 1D concentration profile along the z-axis of the region in fig. 5.46 with a local enrichment of elements in the PaA state

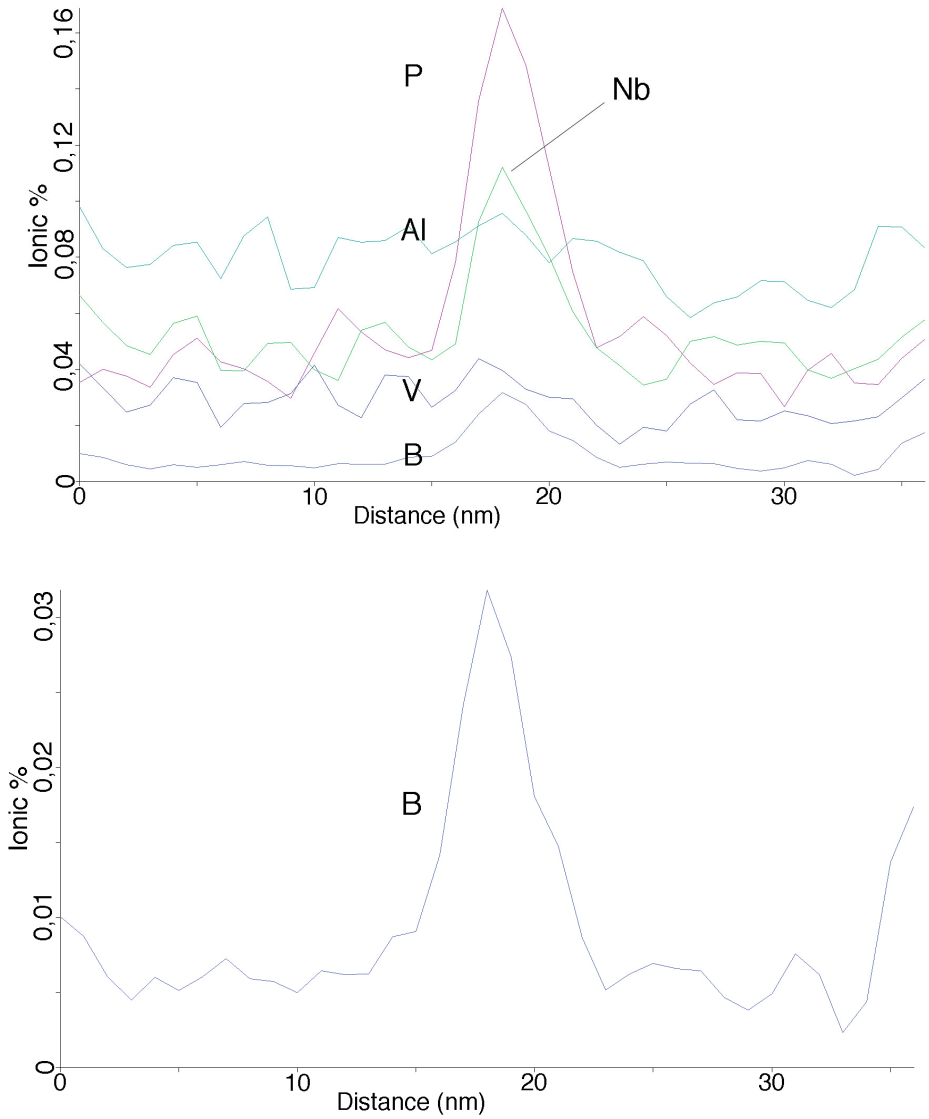

Figure 5.48: 1D concentration profile along the z-axis of the region in fig. 5.46: details of a local enrichment in the PaA state (separately displayed for B)

5.7 Polygonal Austenite with DIC and Annealing (PoA)

To compare the development of the microstructure resulting from polygonal austenite during tempering with the behavior of the thermomechanically rolled condition, tempered samples from the PoQ state have been fabricated.

5.7.1 Mechanical Properties

The stress-strain diagrams of this specific state can be seen in fig. 5.49, its toughness-temperature diagrams are found in fig .5.50, with the corresponding values shown in table 5.5. In the stress-strain diagrams it can be seen that this state shows similar analogies to the PoQ state as the PaA to the PaQ state. A sharp yield point is observed and the UTS falls by 229MPa whereas the YS raises slightly, compared to the quenched state. This gives a YR of 0,96.

UTS [MPa]	882
YS [MPa]	842
A[%]	18,3
YR	0,96

Table 5.5: Mechanical properties of the PoA state

The impact toughness-temperature diagram is above the limit for toughness class J at 0°C, showing distinct scattering in the temperature regime above 0°C.

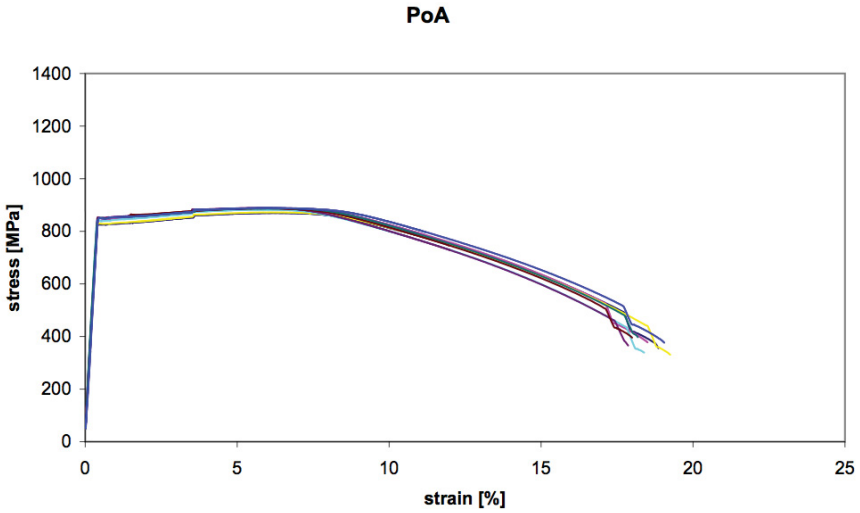

Figure 5.49: Stress-strain diagrams of the state PoA

5.7.2 Microstructure

The microstructure of the PoA state shows the same relations to the PoQ state as the PaQ state to the PaA state. This means that already in the optical microscope cementite, preferably at the austenite grain boundaries is observed (fig. 5.51). Furthermore, the contrast between martensite and bainite in the HFP etched micrographs is widely gone. In the SEM (fig. 5.51 b), marked with arrows), it can be seen that the precipitated carbides already decorate a large part of the austenite grain boundaries.

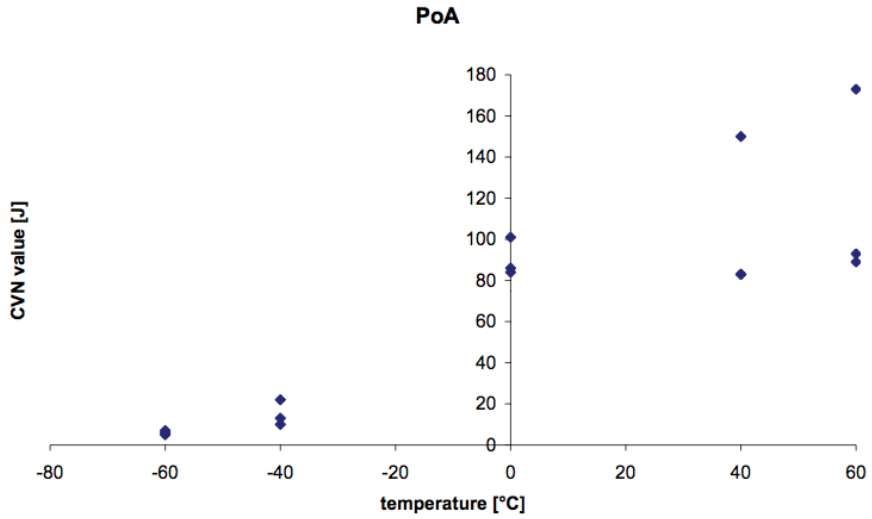

Figure 5.50: Impact toughness temperature diagrams of the state PoA

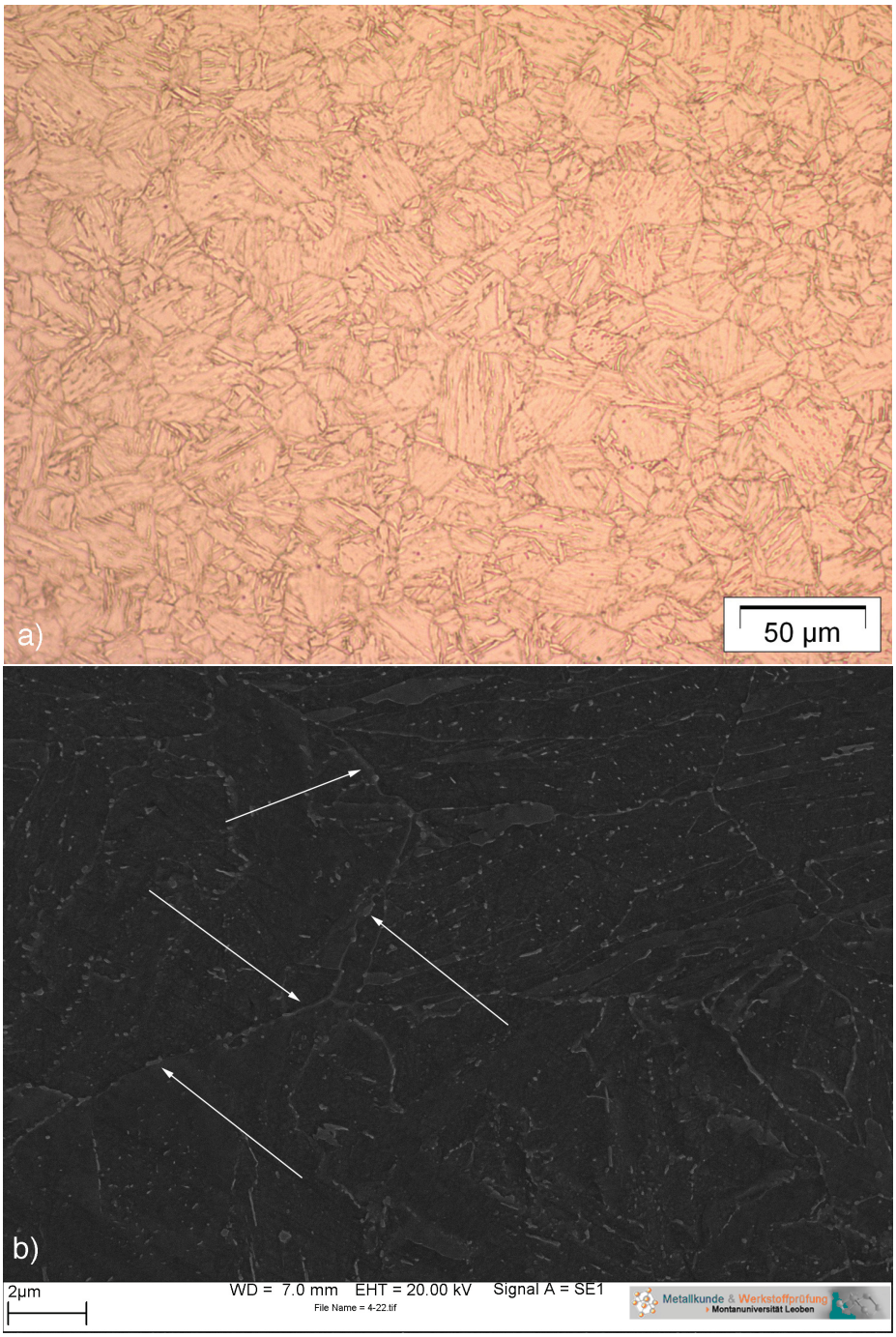

Figure 5.51: Microstructure of the PoA state in the LM, etched with HFP a) and in the SEM, etched with Nital b). Arrows: former austenite grain boundaries

5.8 ”Normalized”

Apart from the scheme deformed-undeformed austenite, quenched-annealed, a heat treatment has been performed with slow air cooling after the austenitization. This heat treatment state is to evaluate the approach towards equilibrium due to slow cooling.

5.8.1 Mechanical Properties

The stress-strain diagrams can be seen in fig. 5.52, the toughness-temperature diagrams of the material are displayed in fig. 5.53, the corresponding values in table 5.8.1. Besides the fact that no sharp yield point is observed here, the stress strain curve is quite identical to the PoA state, though being obtained by a very different time-temperature history. The lack of a sharp yield point is manifest in the yield strength of 605MPa. The toughness of this state is even poorer than in the PoA state. It does not ascent until a temperature of 40°C.

UTS [MPa]	862
YS [MPa]	605
A[%]	17,1
YR	0,70

Table 5.6: Mechanical properties of the normalized state

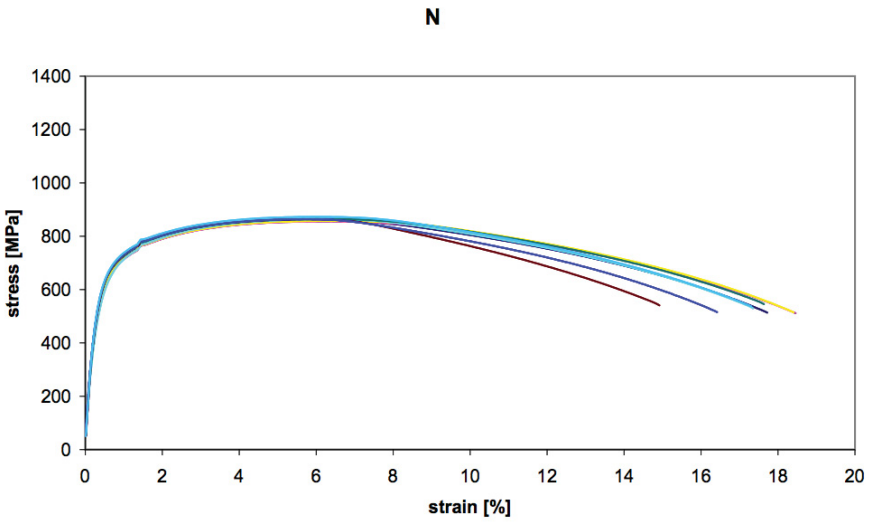

Figure 5.52: Stress-strain diagrams of the normalized state N

5.8.2 Microstructure

In the normalized state, the microstructure has a strongly altered appearance compared to the other states (fig. 5.54). This is expected, since the structure of microalloyed, thermo-mechanical processed materials is widely defined by the temperature-deformation history of the material, which is totally different in this case. The main reason for the occurrence of this microstructure can be seen in the slow air cooling from high temperatures. Even the substitutional elements had plenty of time to diffuse, leading to a microstructure that has mainly two constituents, where one is very inhomogeneous.

Such a microstructure develops, when ferrite (marked "1" in fig. 5.54 b)) forms below A_{R3}, pushing the supersaturated elements into the remaining austenite, where the solubility is higher. When the slow cooling material finally reaches A_{R1}, the remaining austenite does not really equal a low alloy steel any more, since a large enrichment of alloying elements has been

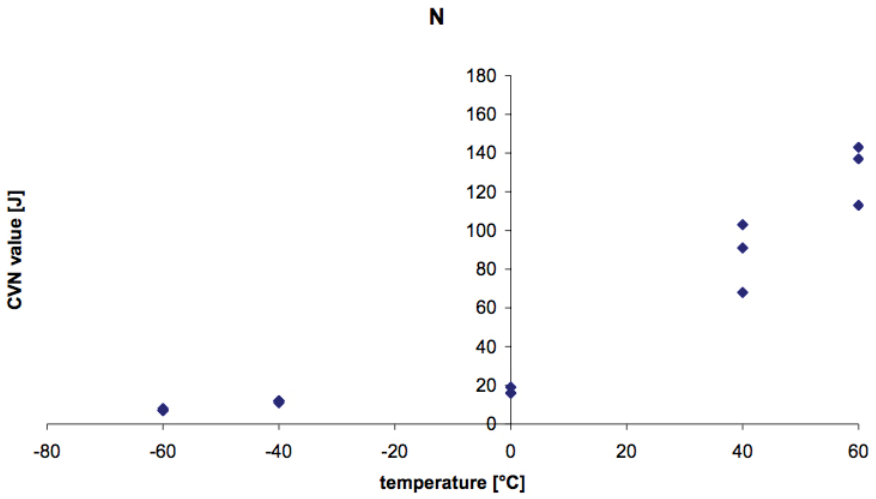

Figure 5.53: Impact toughness temperature diagrams of the normalized state

performed. The remaining austenite forms bainite/martensite. This behavior is for instance used to produce dual phase steels. In contrast to dual phase steels, the trial heavy plate also contains very slow diffusing elements such as Mo and V, so we see an assumingly martensitic shell (labeled "2" in fig. 5.54 b))with a bainitic or auto-tempered martensitic core (marked "3"), when looking at the larger grains of the inhomogeneous phase in normalized state. In the end, since further investigations have not been performed for this state, It can just be assumed what the individual phases are. In fig. 5.54 b) also, the presence of small particles (assigned "4") can be hypothesized. These particles are probably cementite but could already be coarse VC particles, NbC is also seen as possible.

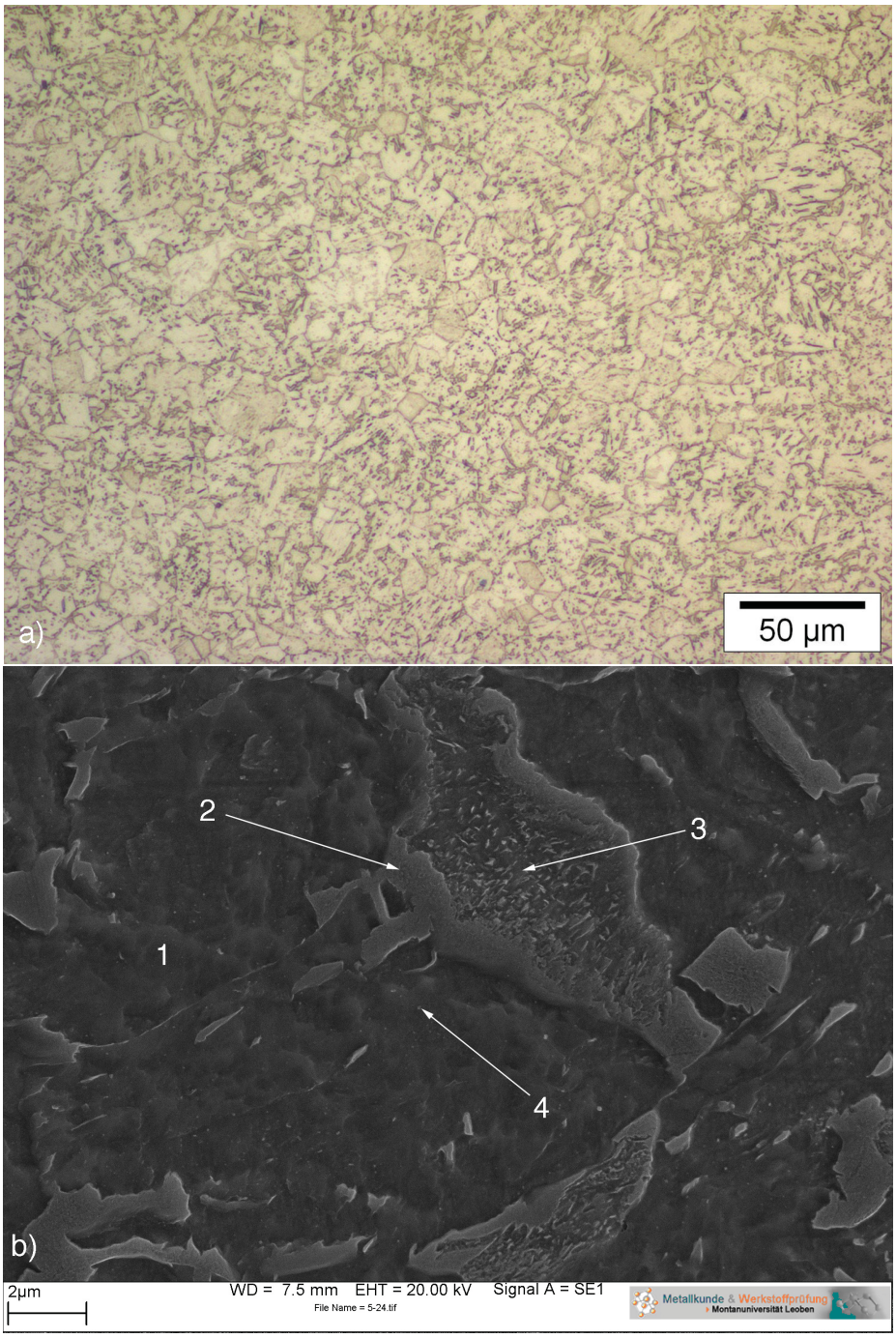

Figure 5.54: Microstructure of the normalized state in the LM a) and SEM b), etched with Nital

5.9 Fracture Appearance of the Tensile Testing Samples

If a mild steel is loaded with tensile stress at room temperature, usually ductile fractures are observed that are called cup and cone fractures. The fractures observed with the tensile tests in this work (fig. 5.55) show the same appearance in principle, but with some anomalies.

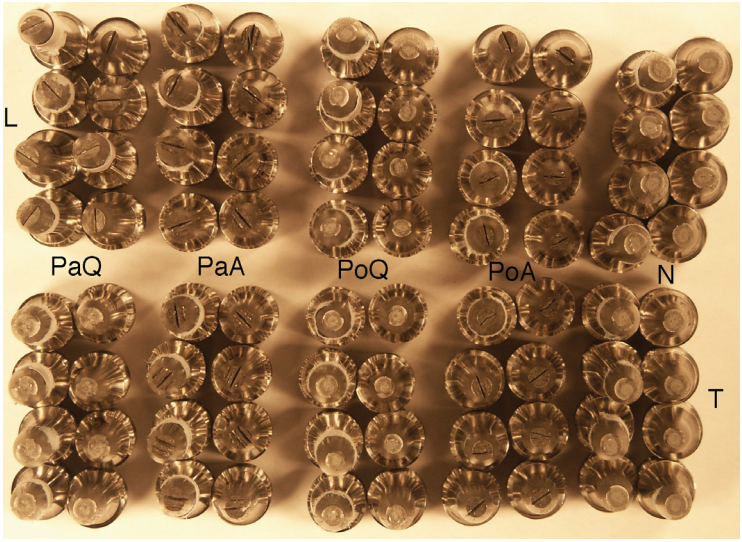

Figure 5.55: Fracture appearance of the different heat treatment states in the tensile test

First, in the pancaked states, an anisotropy in deformation is observed, manifest in an elliptical fracture shape. The PaQ state additionally shows pre-fractures in the middle segregation zone for the longitudinal samples. These occur shortly before the sample fractures in the tensile test. Second, the annealed states showed a splitting of the samples perpendicular to the original fracture plane (separations), that will be discussed below.

5.10 Change of the Fracture Appearance with the Annealing

Below a defined temperature, bcc metals show the effect that they loose their ductility. The fractures then obtained follow distinct crystallographic planes. In the case of ferrite it is the {100} plane, the plane with the highest packing density. Under different conditions, it can be observed that the fracture (ductile and brittle) dos not follow the path given by the load any more, following some microstructural features, such as grain boundaries. The CVN values measured then can be lower than the one of the uniform material.

In the case of microalloyed bainitic steels, the former austenite grain boundary is the feature that is prone to show such phenomena. The occurrence of so-called separations is well known in industrial practice, meaning, the material shows multiple fractures, perpendicular to the main direction of the fracture, following the former austenite GBs. The inhomogeneities that are seen to cause this are second phases (carbides) or segregations. The first ones have been observed in this work.

In particular, separations follow a combination of the triaxial stress state (plane strain conditions) with the microstructure. This relieves the triaxiality of the stress state in the notch base in general, sometimes leading to higher toughness values in the low-temperature regime. At elevated temperatures, where the tough fracture mode is dominant, the triaxiality is less important, so the weakening by the separations lowers the toughness values. It has to be mentioned that the raise in CVN values at low temperatures can not be considered positive, since it is not clear, at which degree of deformation the material is already marred. This would be of special importance, if mounting brackets or cantilevers are welded to the material. An instrumented CVN test could probably clarify at which point damage is present. In the present

case, intergranular[2] fractures are present at temperatures where the samples do not fracture fully brittle. In fig. 5.56 the different fractures obtained are shown.

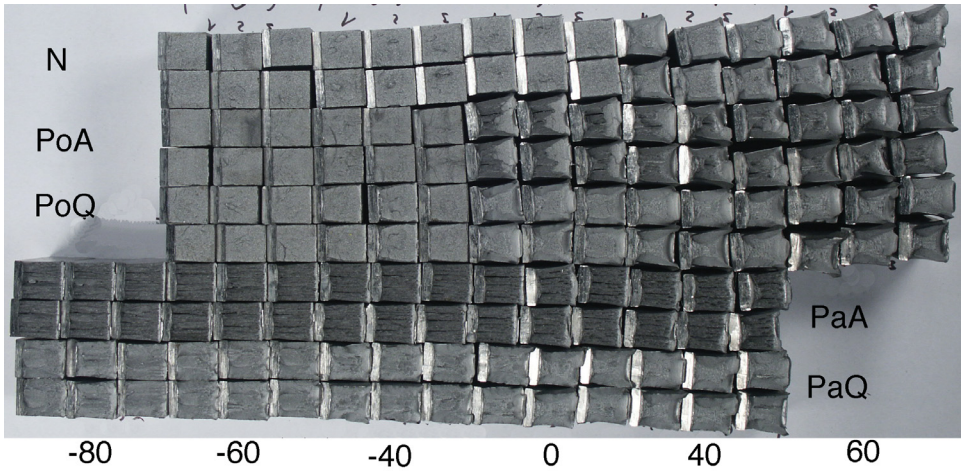

Figure 5.56: Fracture appearance of the different heat treatment states in the CVN test at different temperatures

Investigations in the SEM illustrate the different microscopic appearances that are already manifest macroscopically. The shipping state PaQ shows a fracture, as it is desired (fig.5.57). Homogeneously distributed honeycomb shaped structures, in the case of this very clean steel, with hardly any inclusions observed inside the honeycombs.

The PaA state shows the afore - mentioned separations (fig. 5.58). It can be seen that the fracture is ductile besides the separations. Though this has not been clearly confirmed, it is assumed that the smooth surfaces of the separations are caused by carbide films precipitated at the former austenite grain boundaries. For the final fracture, the lamellae build prior have been

[2]In the case of the pancaked material, intergranular means in between the former austenite grains

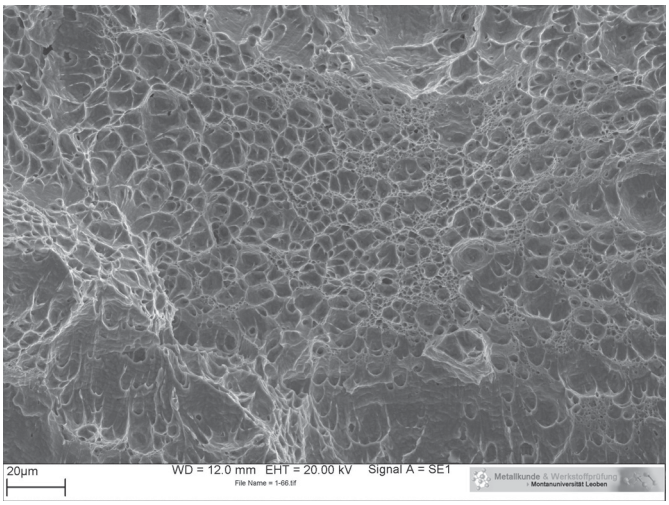

Figure 5.57: Fracture appearance of the PaQ state, SEM image at 0°C

sheared off what is best seen at the "thicker" lamellae on the right side of fig. 5.58 (marked with arrow).

For the polygonal microstructure PoQ, it may surprise that at 0°C already a widely brittle appearance is observed (fig.5.59), since the CVN samples show deformation and the CVN values are at a reasonable level. A small ductile fraction can also be observed.

If the polygonal structure is annealed we obtain the same picture as above. Especially in the temperature region above 0°C, intergranular fracture features are observed (fig. 5.60). Below 0°C, the fracture behavior is fully brittle, so the weakening of the GBs obviously plays no role. Here, also carbide films at the grain boundaries are blamed to be the cause of the intergranular fracture.

In the normalized state, entirely brittle fractures are observed up to room temperature (5.61), resulting in low CVN values. At elevated temperatures, values comparable with the other states are obtained. Nevertheless, such a

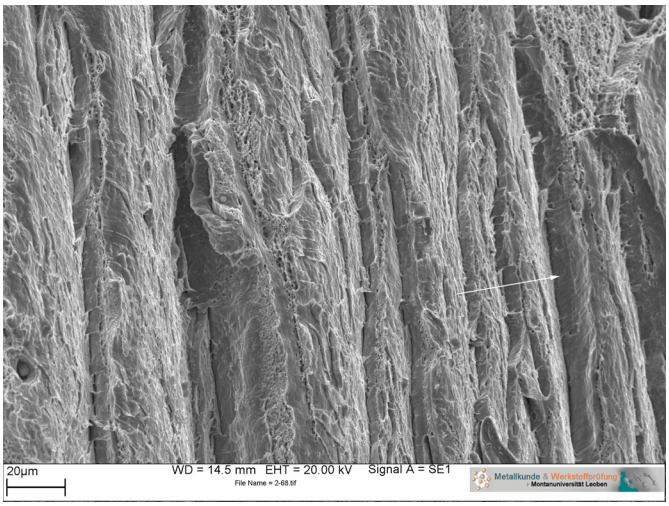

Figure 5.58: Fracture appearance of the PaA state, SEM image at 0°C

material is not suited for technical use.

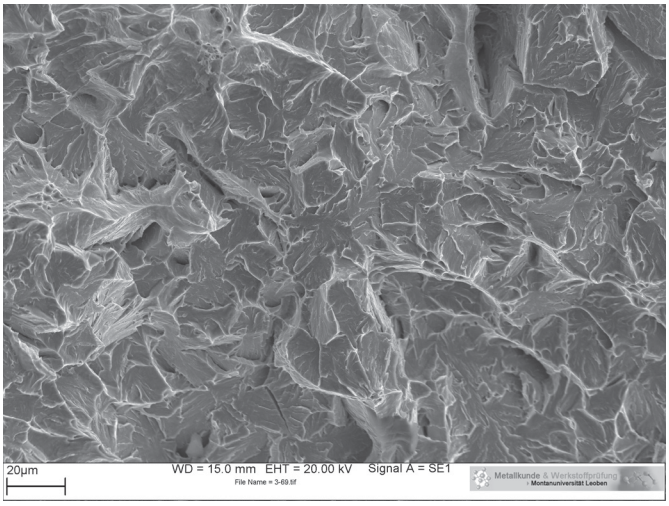

Figure 5.59: Fracture appearance of the PoQ state, SEM image at 0°C

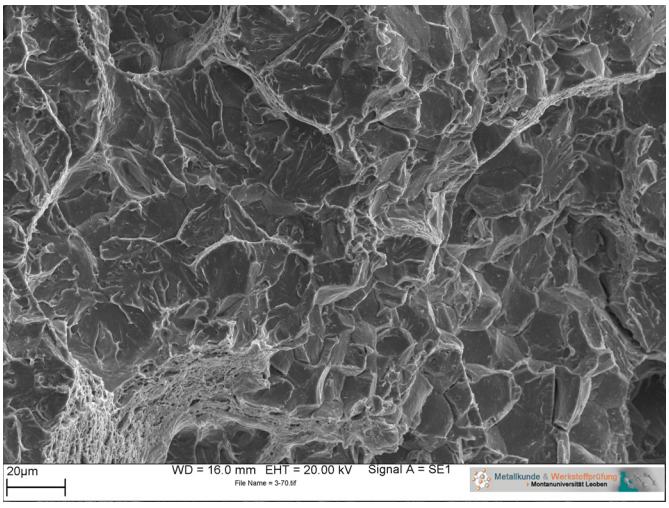

Figure 5.60: Fracture appearance of the PoA state, SEM image at 0°C

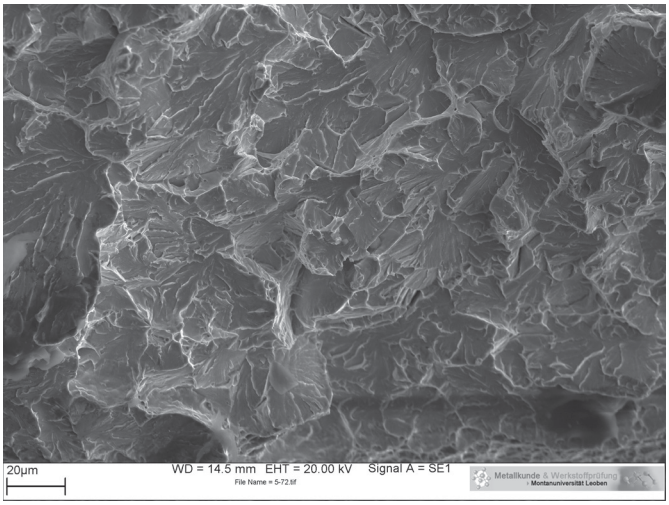

Figure 5.61: Fracture appearance of the N state, SEM image at 0°C

5.11 Impact Toughness - Temperature Diagrams of the Individual States in Comparison

In the shipping condition PaQ as well as in the annealed PaA condition, the material does not exhibit the typical transition behavior, that is expected for a steel of this low carbon content. It shows a slow ascending behavior with temperature, with slightly higher values for the quenched state. This can, amongst other things, be explained by the carbides films at the grain boundaries. It is remarkable, that the low temperature toughness even at a temperature of -80°C is in average above 30J for a 7,5mm subsize sample, equating 40J for a 10mm sample, for both states. The average toughness values versus temperature are displayed in fig. 5.62. As the material's struc-

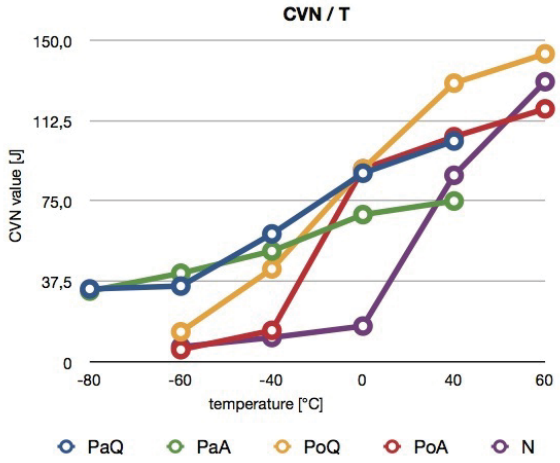

Figure 5.62: Impact toughness-temperature behaviour of with the different heat treatment conditions (7,5mm subsize CVN samples)

ture is changed by heat treatment, also changes in the fracture toughness occur. For the PoQ and the PoA state, it has been observed, that the toughness at -60°C is still poor, for the PoA still at -40°C. It should be denoted

that these states had even more carbides at the grain and lath boundaries than the pancaked conditions. Data about segregations, that could also be responsible for poor toughness at low temperature, is not present. At higher temperatures, the toughness values are higher than those of the pancaked states, probably caused by the lower strength.

In the N state, that has been tested for comparison, the toughness is low, up to a temperature of 0°C, then strongly rising, reaching the values of the polygonal states at 60°C. It can be stated, that a material with this fracture behavior can not be used commercially.

5.12 Stress - Strain Diagrams of the individual States in Comparison

The stress-strain relations of the individual states in comparison (fig. 5.63) show that the highest tensile strength is obtained by the pancaked and quenched state, while the yield strength is just as high for the pancaked and annealed state. The PaA state also has a higher fracture elongation than the PaQ state. This behavior is caused by the occurrence of a yield point, that is observed in both annealed states. Further, differences of the values for the UTS and the yield strength for the L and T samples have been observed, 90MPa for the shipping condition and around 45MPa for the annealed state.

In contrast to the pancaked states, the states with polygonal microstructure show no anisotropy in the mechanical values any more. The tendency that the quenched state has a higher UTS, while the annealed state has a higher yield strength has also been observed here. The same applies for the fracture elongations, that rise with falling tensile strength.

The schematic development of the material‘s mechanical properties due to the different heat treatments is displayed in fig. 5.64. It can be seen, that the UTS falls, the more heat treatment steps the material has experienced, what does also apply for the YS. In tendency, the fracture elongation raises, as the strength falls, with a remarkable high value for the longitudinal samples of the PaA state.

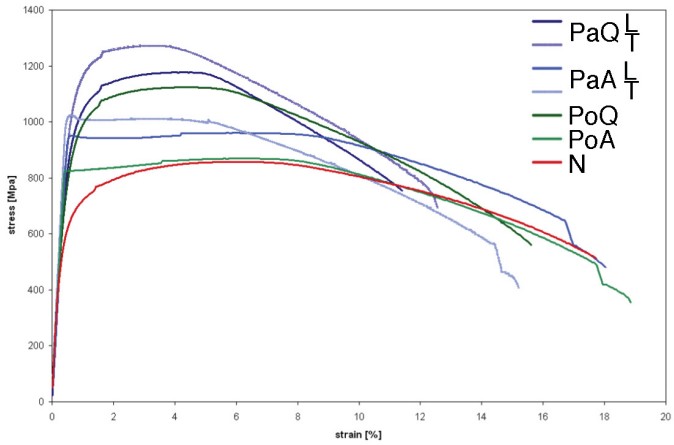

Figure 5.63: Stress-strain relations of all states (for PaQ and PaA in longitudinal (L) and transverse (T) direction) in comparison

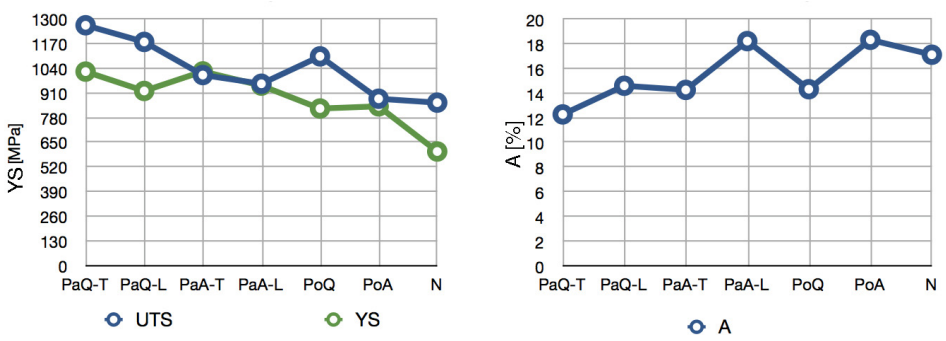

Figure 5.64: Development of the mechanical values with the different heat treatment conditions, the UTS and YS (both [MPa]) on the left side, the fracture elongation [%] on the right side

5.13 Calculated Contributions to the Strength

5.13.1 Overall Strength of the PaQ State

If we use the information gathered about the microstructure and the elemental distribution of the PaQ state, equ. 2.11 (pp. 17) can be used to calculate the individual contributions to the overall strength.

The Strength of Pure Annealed Iron

The strength of pure annealed iron can be found for example in [Bha97], as 219MPa.

Dissolved Carbon

After Young, the contribution of C is given by $1722,5\sqrt{wt\%C}$ [YB94]. In this case, we have to assume that the average concentration of carbon inside the laths equals the concentration of carbon, measured with the atom probe, displayed in fig. 5.22. The measured value is 0,06at% or 0,012wt%, thus giving a contribution to the yield strength of 189MPa.

Substitutional Solid Solution Hardening

For calculating the contribution of the substitutional elements, values from [Bha97] have been taken. Due to the low concentration of the hardening elements, the effects have been assumed to be linear with respect to the concentration. In fact, only Si and Mn give relevant contributions, namely $0,35wt\%Si \cdot 115MPa/wt\%$ and $45MPa/wt\%Mn \cdot 2wt\%$ summing up to 126,75MPa.

Dislocations

For a cooling rate of 20°C/s a transformation temperature of approx. 450°C has been measured for the undeformed austenite. Following equ. 2.14 (p. 25), this gives a dislocation density of the bainite of $2,5 \cdot 10^{15} m^{-2}$, and a raise in yield strength of 366MPa, with a work-hardening constant K_{WH} of $7,34 \cdot 10^{-6} MPam$. This is a rough estimation, to get exact data, it would be essential to perform measurements on material that has been deformed like the material in the industrial process. Furthermore, the microstructures, where the empirical equation of the dislocation density is based on, have been obtained by isothermal transformation and without prior austenite deformation. By far the biggest factor of uncertainty is the general scattering of the data, used to derive equ. 2.14, as can be seen in fig. 2.7. A much lower dislocation density of $1 \cdot 10^{15} m^{-2}$ is seen to have the same justification based on this data, giving a contribution of 232MPa.

Lath Boundaries

The lath thickness has not been determined exactly, but a value of 250nm is seen as a reasonable value (see e.g. figs.5.8 and 5.9), so the dislocation's mean free path $\bar{L}_3$ is $2 \cdot 250nm$. k_ϵ is $115 MPam$ [Bha01]. This gives a lath boundary contribution of $230 MPa$. This contribution is a very critical value, since lath thickness varies a lot inside the microstructure, and a small change in lath thickness leads to a big change in yield strength.

Overall Strength

Regarding the calculated contributions, this sums to a total yield strength calculated in equ. 5.1, the amount of the individual contributions is illustrated in fig.5.65.

$$\sigma_y = \qquad (5.1)$$

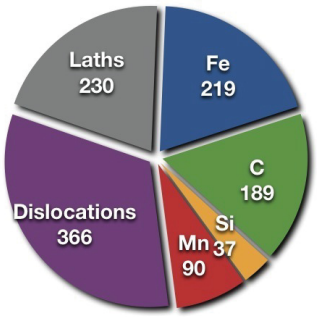

Figure 5.65: The calculated tensile yield strength factorized into the different contributions [MPa]

$$\sigma_{Fe} + \sigma_C + \sigma_{ss} + \sigma_{Dislocations} + \sigma_{Laths} =$$
$$219MPa + 189MPa + (36,75 + 90)MPa + 366MPa + 230MPa$$
$$\approx 1130MPa$$

The overall value incorporates two big sources of error, the dislocation density and the lath thickness. The good accordance to the measured value of 1025MPa is therefore not to be taken for granted, these models need to be verified on a lot more materials, to get an estimate of the error.

5.13.2 Overall Strength of the PaQ State estimated from Measured Data

Another way to approach the problem of predicting the strength of the produced material is the estimation of the UTS from the hardness, that has been measured for different transformation temperatures by Cizek et. al. [CWD+02]. For the derivation of the UTS from [CWD+02], one needs to extrapolate the data, since a transformation temperature of 450°C has not been achieved. A linear extrapolation gives a hardness of 320HV5,

what equates to a UTS of around 1100Mpa (UTS/HV = 3,4). To estimate the strength of the microstructure based on the transformation temperature alone makes sense, since the strongest contributions to the strength, the dislocation density and the lath thickness, are strongly influenced by the transformation temperature, while the element distribution is not altered significantly. This should be consistent as long as the ratio bainite/martensite is not changed significantly, since the martensite does not accommodate its strain plastically.

5.13.3 An Estimation of the Precipitation Hardening of the Annealed States from the Swift Equation

It has been shown that, for steels, it is possible to derive the yield ratio (YR), defined as the ratio of yield strength (YS) to ultimate tensile strength (UTS), from the work hardening exponent [KKLK02] by a continuum mechanical approach. This is expressed in the so-called Swift equation (5.2),

$$YR = \frac{YS}{UTS} = \frac{(b + ln(1 + e_y))^N}{(1 + e_y)} \frac{exp(N - b)}{N^N} \tag{5.2}$$

where b is the additive strain constant, e_y the engineering strain at yield strength (usually 0.002) and N is the work hardening exponent. The Swift equation is, of course just applicable if there is no yield point, meaning Ludwik's equation (equ. 2.1, pp. 7) is valid. In this work, it has been used to estimate the increase of yield strength, added by precipitation hardening. The basic idea is that the yield ratio would be described by the Swift equation, if there were no precipitations and that the difference to the actual yield point is just caused by the precipitations and the effects entailed. This is seen to be possible since the yield ratio of all of the investigated material states are within a narrow range (0.75-0.8, except for the normalized state, where it is 0.7). The value for the work hardening rate, that basically defines the

yield ratio, of course changes with the annealing [WW86]. Just for 600°C, it happens to be the same again as for the unannealed material. Otherwise, it would have to be corrected, because the work hardening rates can differ up to 1:3. Strong differences, on the other hand would already be manifest in the stress-strain relations. The data shows similar values for all three pairs of tensile tests, where such a calculation was possible, but since the values are just based on a few tensile tests and the work hardening rate has not been determined directly for this material, it can just be seen as a guide value.

The calculation, displayed in table 5.7 states a raise in yield strength by the precipitations of slightly above 200MPa, for an annealing to 600°C. This might appear quite high, but the stress strain curves show a loss of around 250MPa of tensile strength during the annealing, that is for the YS fully compensated by the precipitation hardening.

	PaA transverse	PaA longitudinal	PoA
actual YS	1026	961	882
YR of the quenched state	0,81	0,78	0,75
calculated YS	816	750	662
difference	210	211	220

Table 5.7: Calculation of the effect of VC on the YS, based on the YR

Chapter 6

Summary and Discussion

6.1 Microstructure and Sub-microstructure

During the industrial development process of the material, the microstructure has mainly been investigated using the optical microscope, etching with Nital. Especially in the case of the investigated trial plate, the structures that are responsible for the properties of the material can not be accessed by this method. It has therefore been unclear, which constituents are formed under the influence of microalloying and thermo-mechanical treatment. The application of atom probe tomography even made it possible to reveal the behavior of the alloying elements down to an atomic scale.

6.1.1 Microscopic Appearance

It has been observed that the material, as it is shipped, consists of a bainite based structure with martensite (fig. 5.5) . Martensite is found in two different forms. First martensitic laths, that are embedded in the bainitic structure and second, larger martensitic islands, that extent through a whole austenite grain in thickness and have a length from $10\mu m$ up to around

$50\mu m$. These larger martensitic islands have not been observed elsewhere in the literature [CWD+02, SRM+07, KKLK02, JKS+06, etc.] even though lower austenite deformation has been applied in almost all cases. It has to be emphasized that the present literature deals with steel grades of the API X80 and X100 class, whereas the investigated trial plate is rather comparable to the API X120 class [GMH+07] and higher.

If the martensitic islands have an impact on the toughness due to their size can just be guessed, since no actual fracture mechanical data is present. If we take data from Bhadeshia [Bha01] we find a lower boundary K_{1c} value of $25MPa\sqrt{m}$ for bainites with a yield strength of around 1000MPa and an upper boundary value of approx. $35MPa\sqrt{m}$. Using the definition of $K_{1c} = \sigma\sqrt{\pi a}$ we get a lower value of $260nm$ for the critical defect size $2a$ at a tensile strength of $1200MPa$ and an upper value of $540nm$. This a conservative estimate, but shows that not just the martensitic islands could already be critical, but also the carbides [Bha01]. It has to be denoted that the hardness of the martensitic islands has not been measured, so it is not known how these martensitic islands really contribute to the mechanical properties. In general, the lath shaped type of martensite is seen to be more desireable. It strengthens the bainitic structure by putting constraint on the bainitic ferrite [YB94]. Measurements of the carbon content of this constituent would be in demand for an estimation of the strength and the transformation temperature and to model the transformation mechanism.

At the lath boundaries and the former austenite grain boundaries, carbide films have been observed. After the material has been annealed to 600°C, the carbides show coagulation tendencies quite similar to steels that have been spherodize annealed. It is observed that the chemical differences between the martensite and the bainite have widely vanished during annealing, as can be seen by a uniform microstructure, obtained by etching with HFP (fig. 5.39). Furthermore, not just the amount of carbide films at the grain boundaries

has risen, but also the carbide size (up to 500nm), being above the fracture mechanical critical size. Separations are observed for the CVN samples in this state, that can be assigned to these carbide films, as recently found in a comprehensive study on forming limits of various steels by Narayanasamy et. al. [NPN08].

The material that started from a polygonal austenite microstructure, shows the same constituents, as the material with a pancaked austenitic structure (fig. 5.34). It is bainite based with annealed martensite. This structure is more similar to the microstructure that is found in the heat affected zone (HAZ) of welded HSLA heavy plates [SGM04, XBM+03] or microstructures that have been obtained by other processes without or with low austenite deformation [CWD+02, BYMJ98, JKS+06, DP03]. The lath thickness seems to be larger than the one of the pancaked material, caused by lower driving force and austenite strength during deformation [Bha98]. The carbide films also seem to be more salient than in the pancaked states. The annealing also has the same effects as in the pancaked state. Spherical carbides are present in a chemically even microstructure. The CVN samples also show separations.

6.1.2 Submicroscopic Appearance

The results obtained in the submicron regime, investigated with the TEM, are confirming the results from the optical microscope and SEM, regarding the grain boundary films and the principle identification of the microstructure of the material as bainite with annealed martensite (fig. 5.8). It can be seen that the lath thickness is in the range of 250nm, for both the quenched and the annealed condition. Further, a high dislocation density in the laths has been found, that has been conserved during annealing.

The resolution of the TEM made it also possible to find the particles that

are responsible for the recrystallization inhibition in the material. These (Ti,Nb)(C,N) particles have been observed inside the former austenite grains in a relatively coarse form, sized around $50nm$ (fig. 5.11). For the coarser particles it has been found that the morphology depends on the ratio of Ti/Nb in the particle. The blunter the particle, the higher the Nb content is. This is consistent with existing literature and confirms that the coarser, Ti rich particles have formed at higher temperatures, as stated in [HJKP03, OH92, PCH01].

At the former austenite grains, finer (Ti,Nb)(C,N) with $7 - 10nm$ have been found (fig. 5.11). Similar size distributions have been observed in recent neutron scattering (SANS) experiments [DSOR$^+$02] whereas prior TEM studies often indicate a precipitation size slightly above that value (10-20nm) [HKP02, CHGB00, PL07, PCH01]. One of the fine particles analyzed ($\approx 10nm$ diameter), shows a ratio of Ti/Nb that is already 1:2. In these Nb rich particles, also a participation of Mo and V has been found. This indicates a formation temperature below 900°C [ABJ83, HKP02], where Mo and V retard the precipitation of the carbonitride by lowering the activity coefficients, mainly of the interstitials. The conclusion drawn is that the intragranular particles mainly bearing Ti are formed at temperatures above the TM rolling process, and therefore do not contribute to recrystallization inhibition. They can also act as nucleation sites for undesired intragranular formation of the carbonitrides [CHGB00].

In the annealed structure, fine VC particles sized below $10nm$ have further been found (fig. 5.45). These are seen to cause the yield point observed for this states.

6.1.3 Atomic Level

Dealing with the processing of bainitic heavy plates, various questions arise, that are assigned to interface chemistry or short-range diffusion. These questions had to remain unanswered in the past. The recent developments in atom probe analysis and sample preparation techniques are now enabling direct quantitative observations of phenomena like the C distribution after the bainite reaction or small scale segregations, some of which have been observed in this work.

In the quenched condition, there has not been found any uneven distribution of the elements in the steel besides C and B (fig. 5.21). Even in a carbide that has been measured, the elements besides Fe and C participated in a ratio that is equal to the bulk composition. This is expected for baintic structures and has priorly been observed [Bha81a, HBS82, SSB90, PBMB04, CM07].

At interfaces, carbon is enriched, or even carbides are formed. At several sites that are assumed to be interfaces, the carbon content one one side has been higher than on the other side. Segregations of any kind have not been observed besides B and C. Inside one larger region that is contained in a single measurement, the carbon shows a concentration profile, that is U-shaped. This concentration profile could for example be produced by a bainitic lath forming, when the carbon that was pushed into the remaining austenite diffuses back into the lath. Comparing this with the TEM results, the enrichment in C is obviously not enough to stabilize the austenite, neither in the form of austenite films, nor as martensitic-austenitic (MA) constituents, both of which have not been observed in the TEM (described for example in [GDCR06, SRM$^+$08]). The observed C concentration inside the lath was 0,06at%. The concentration at the lath boundaries varied in a wide range from 0,12at% (0,025wt%), to 1,2at% (0,25wt%), comparable data has not been found.

At one site, that is seen to be an austenite grain boundary, a clear en-

richment of B has been measured, combined with the detection of C (fig. 5.28). B has not been measured in an comparable amount at any other position in the thermo-mechanical rolled and quenched state. From a quantitative viewpoint, it is stated that only around 1,5appm are in total present at the austenite grain boundaries[1] in contrast to 32appm within the grains. This means that the amount of B addition should be independent from the austenite grain surface per unit volume. This stands in contrast to present literature, where this is assumed [BS93]. Comprehensive TEM investigations on the structure and crystallography could reveal if this is already an saturation value. Such investigations have not been performed on steels so far, but atom probe investigations have been performed by Wolde-Giorgis [WG05] to reveal the physical origin of Bi solubility in Cu. This has been performed for Bi segregation in Cu to a 12° low angle grain boundary and gave a value of $1,2 atoms/nm^2$ compared to a calculated value of $2 atoms/nm^2$ if the Bi atoms are assumed to align in the core of the dislocations forming the interface. The measured value of $0,4 atoms/nm^2$ in this work also is of this magnitude, what suggests that a similar mechanism might be the cause of the grain boundary solubility of boron.

In the annealed state, an enrichment of P, Mn, V and Nb has clearly been observed at one position, besides the priorly present segregation of C (fig.5.46). Similar behavior for C and P has been found by Pereloma et. al. [PTJM06]. In contrast to the present work, Pereloma found a depletion of Mn. Further, a very inconsistent behavior of Cr has been observed. Some interfaces showed enrichments in Cr, while others exhibited depletions. The width of segregation at all the observed boundaries, which was estimated from the composition profiles, was 7–8 nm. The same has been detected in this work. Segregations might also contribute to the formation of separations in the annealed states as speculated for example by Peters [Pet88].

[1] Austenite grain surface per unit volume times the observed areal atomic density

In the middle segregation zone, an enrichment of Ti(6x), Nb(2,5x) and especially S(11x) has been found. This relys on a single measurement where no particles have been detected (fig. 5.29). This leaves the possibility that C has not been found in an extended amount, because carbides have formed in presence of Ti and Nb. Such particles could promote the fractures observed in the middle segregation zone.

As a conclusion for the atom probe measurements of the trial plate, it has been recognized that investigations without site-specific sample preparation or TEM imaging of the needles are putting major difficulties to the interpretation of the results in microstructures with varied constituents. It is not always clear, which feature caused the elemental distribution observed with the atom probe. The preparation methods suitable are still in their infancy [KM07, MRT+07, CCG+07, Sch01], but will in future enable investigations of selected areas within the microstructure [SCM+07, CSMR07, TLL+07]. The method introduced in this work (fig. 3.4) has demonstrated this capability.

6.2 Effect of Pancaking on Microstructure and Strength

One of the key aspects of the investigated heavy plates is the deformation of the austenite, before it is transformed into bainite/martensite. The reason for this is that the driving force for transformation is much higher in the deformed state than in the polygonal, recrystallized state. To estimate the effect, the pancaking has to the material, we can compare the pancaked states to the one that have been recrystallized. It has to be regarded, that the PoQ and PoA state have been produced by static recrystallization instead of dynamic recrystallization.

When comparing the HFP micrographs of the PaQ (fig. 5.5) and the

PoQ (fig. 5.5) states, it can be seen that the percentage of martensite is much higher in the PoQ state than in the PaQ state. Further the amount of "blocky" martensite has increased in comparison to the amount of lath-shaped martensite. It is therefore assumed that the "blocky" martensite is formed from uniform austenitic areas whereas the lath-shaped martensite is formed from regions that have been enriched in carbon during the bainite reaction, thus having a lower M_s and higher strength.

The change in amount of martensite is also manifest in the CCT diagrams, published by Jun [JKS$^+$06] and Cizek [CWD$^+$02]. In the work published by Jun, the martensite disappears fully up to a distinct cooling rate, due to the deformation, while the work by Cizek just implies a decrease in volume fraction. Different martensitic constituents have not been distinguished by these authors.

In this work, the differences in UTS between the PaQ state and the PoQ state, as well as the differences between the PaA and the PoA state, have been assessed. The main problem hereby is the anisotropy of the mechanical values of the pancaked states, so we can only take an average between the two orientations of the samples (L and T). This gives a difference of $120MPa$ for the quenched states and a difference of $102MPa$ for the annealed states. From this, it can be assumed, that the effect of the pancaking is a rise in strength of $\approx 100MPa$, in spite of the decrease of the martensite volume fraction. It has to be emphasized that the hardness of the martensite formed is unknown.

6.3 Development of the Material during Annealing

In production, the cooling of the material is stopped at a defined temperature (usually 200°C), the change of which leads to changes in the material's properties, especially the yield strength. It has been speculated what mechanisms stand behind that phenomenon, precipitation strengthening was the logical conclusion that has been drawn. An annealing sequence has already been performed by voestalpine, finding a maximum in yield strength from 300 - 450 °C annealing temperature. Unfortunately, the stress-strain curves behind are not accessible any more, so, the appearance and development of a yield point can not be traced. In the stress-strain relations for the annealed states measured in this work, a yield point has been found consistently.

The further investigations were able to confirm the assumption. First, the precipitations have been directly imaged with the TEM and identified by ED as VC or V_6C_5(fig. 5.45). Second, the lattice strain caused by the precipitation of the particles has been traced by XRD, showing a maximum around 400°C (fig. 5.36). The maximum raise in hardness by VC, found in the literature is obtained by annealing at 360°C [Bha01], for short annealing periods. By analysis of the stress-strain relations, a raise in yield strength, caused by the precipitations, of 200MPa has been found (table 5.7).

6.4 Comparison measured/calculated Mechanical Properties

From measured data [CWD$^+$02] on the dependency of the hardness on the microstructure (fig. 2.15) we derive a UTS of 1100MPa by linear extrapolation, compared to 1269MPa (T) and 1182MPa (L) measured . This is

an aberration of 15% and 7,5%. The possible reasons for the consistent lower values are the linear approach for the extrapolation and the fact that the data by Cizek was obtained by much lower austenite deformation (0,3 recrystallizing 0,47 non recrystallizing) than in the industrial process (1,39 recrystallizing; 1,47 non recrystallizing).

For the calculated yield strength, based on the microstructure (equ. 2.11), we obtain a YS of 1130MPa, in contrast to the measured values of 1025MPa (T) (10% error) and 924MPa (L) (22% error). The main error is to be seen in the uncertainty about the dislocation density and to a minor extent, the lath thickness. The large aberration of the longitudinal value is seen to be caused by the measurement of the lath thickness, that has been performed lengthwise in the microstructure.

As a semi-empirical "hybrid-model" it would be desirable to fit the data published by Cizek and own data by voestalpine with a function that includes both, a model for the dislocation density and the lath thickness, defined by the transformation temperature and austenite deformation. The problem hereby is that the lath thickness depends on the transformation temperature by the chemical driving force, resulting in the nucleation rate and the hot strength of the austenite, as a barrier to the plate growth. Such a model has been derived by Singh [SB98] and could be used to improve the accuracy of the predictions when fed with appropriate data.

Chapter 7

Conclusions

Microalloyed HSLA heavy plates have been around for decades and have improved in their properties steadily. The latest development in this field are bainitic heavy plates, heaving yield strengths up to 1000MPa. The development of these new grades has often been performed by laboratory trials, omitting detailed structural characterization. The investigations performed in this work, employing traditional material characterization methods in combination with today‘s most sophisticated research methods were able to reveal the material‘s constitution all the way from the macro down to the atomic scale and gave an exclusive insight into the structures causing the mechanical behavior observed.

The principle microstructure of the material has been identified as not just bainitic, but bainitic with auto-tempered martensite islands and laths, aligned in a pancaked former austenite microstructure. The yield strength of this microstructure amounts to 1026MPa, the ultimate tensile strength is 1269MPa in transverse direction. HF in H_2O_2 turned out to be an excellent etchant to investigate the distribution of the individual phases. Therefore it can be seen that the austenite deformation leads to a decrease in martensite volume fraction, especially to the decrease of ”blocky” martensite. The lath-

shaped martensitic constituent is seen to be better for the reason that it puts a larger constraints to the bainite laths, thus raising the strength of the bainite. Further, the diffusion paths are shorter, what might result in a higher carbon content of the martensite resulting in a higher martensite strength.

This leads to the thought that the smaller, lath-shaped, martensite might even have a lower M_s temperature than the blocky type. This is seen to be possible if there is a higher carbon content and the fact that the loss of the ability to accommodate the transformation strain by forming different martensite variants within one simultaneously transforming area[1] is lost. A lower M_s temperature would also allow to form the bainite at a lower temperature (by alloying), leading to higher strength.

On the atomic scale, the material shows very uniform conditions, with segregated C at various sites that are assumed to be lath interfaces and B at what is seen to be a former austenite grain boundary, while segregations of other elements have not been observed. It is assumed that the amount of B addition needed is independent of the austenite grain surface per unit volume. The measured iron carbide also consisted of the same composition as the bulk, besides C. In the annealed state, segregations of Mn, P and Nb besides C have been observed at one position.

An atom probe measurement of the middle segregation zone showed an enrichment of Nb(2,5x), Ti(6x) and S(11x) in the middle segregation zone relative to the average composition and the presence of Ca and Sr in a minor amount.

The lath thickness is smaller in the pancaked condition than in the polygonal condition that has a higher strength. For the pancaked states, an anisotropy of the longitudinal (L) and transverse (T) tensile strengths can be

[1] usually this is one austenite grain, but in the case of a pancaked microstructure, it is just one untransformed region within one austenite grain

found. The toughness (Charpy V-notch) requirements for toughness class J (DIN EN 10125) are fulfilled to a temperature of -80°C for the shipping condition (PaQ). The transition region shifts to higher temperatures, the more the material is heat treated.

The (Ti,Nb)(C,N) that inhibit recrystallization and grain growth are present in the laths with diameters of around 20-50nm, and at the former austenite grain boundaries with a diameter of 10-15nm. For the coarser (Ti,Nb)(C,N) applies: the blunter the particles, the higher the Nb content. The lower Nb content is also a hint for a formation at higher temperatures. The finest (Ti,Nb)(C,N) have the highest Nb content. These particles also seem to bear Mo and V in a minor amount. It is assumed, that the coarser particles are inactive in inhibiting recrystallization.

The bainitic/martensitic transformation occurs in a temperature region from 500-350°C (for the polygonal microstructure), depending on the cooling rate. This is high enough to self-anneal the martensite. A precipitation of small VC or NbC particles has not been observed after quenching.

During an annealing to 620°C, further iron carbides are precipitated and spherodize-annealed and small ($<$10nm) VC are precipitated. The annealing leads to fractures that do not follow the path of highest stress (separations), that are for this steel suspected to be caused by the carbide films at the GBs. The VC lead to the occurrence of a yield point and a raise in yield strength, that has been amounted to be around 200MPa.

When modeling the mechanical properties from the measured microstructural features, a yield strength of 1130MPa is the result. Some aberration is present, that is majorly seen to be caused by the estimation of the dislocation density, while the values given by solute strengthening, the ferrite strength and the lath boundaries seem to be more reliable. An estimate based on measured data also showed significant deviations, what is seen to be caused by the measurement method in the dilatometer. A combination of

both approaches promises results that are more accurate and reliable.

Bibliography

[ABJ83] M. G. Akben, B. Bacroix, and J. J. Jonas. Effect of vanadium and molybdenum addition on high temperature recovery, recrystallisation and precipitation behaviour of niobium-based microalloyed steels. *Acta Metallurgica*, 31(1):161–174, 1983.

[AFPK06] J. Angeli, E. Füreder, M. Panholzer, and A. Kneissl. Etching techniques for characterizing the phases of low-alloy dual-phase and trip steels. *Prakt. Metallographie*, 43(10):489–503, 2006.

[ASH92] Satoshi Akamatsu, Takehide Senuma, and Mitsuhiro Hasebe. Generalized nb(c, n) precipitation model applicable to extra low carbon steel. *ISIJ International*, 32(3):275–282, 1992.

[BdH83] H. Baumgardt, H. deBoer, and F. Heisterkamp. Überblick über herstellung und eigenschaften von grobblech aus mikrolegierten stählen - legieren, walzen, wärmebehandeln. *Thyssen Technische Berichte*, 1:24–39, 1983.

[BH06] H. K. D. H. Bhadeshia and R. W. K. Honeycombe. *Steels*. Elsevier Ltd., Oxford, GB, 3 edition, 2006.

[Bha81a] H.K.D.H Bhadeshia. An atom probe study of bainite. In H.K.D.H. Bhadeshia and A. R. Waugh, editors, *Proc. of the International Solid-Solid Phase Transformations Conference*,

pages 993–998. Published by The Metallurgical Society of the A. I. M. E., Warrendale, PA, USA, 1981.

[Bha81b] H.K.D.H Bhadeshia. Bainite: The incomplete reaction phenomenon and the approach to equilibrium. In *Proc. of the International Solid-Solid Phase Transformations Conference*. The Metallurgical Society of the A. I. M. E., Warrendale, PA, USA, H.K.D.H. Bhadeshia, 1981.

[Bha92] H. K. D. H. Bhadeshia. *Bainite in steels*. IOM Communicatons Ltd., London, GB, 1 edition, 1992.

[Bha97] H. K. D. H. Bhadeshia. *Mathematical Modelling of Weld Phenomena III*, chapter Models for the Elementary Mechanical Properties of Steel Welds, pages 229–284. The Institute of Materials, London, GB, 1997.

[Bha98] H. K. D. H Bhadeshia. The bainite transformation: Unresolved issues. *ECOMAT*, 1998. for ICOMAT 98.

[Bha01] H. K. D. H Bhadeshia. *Bainite in steels*. IOM Communicatons Ltd., London, GB, 2 edition, 2001.

[Bha02] H. K. D. H. Bhadeshia. Martensite in steels. Lecture script, 2002.

[Bha08] H. K. D. H Bhadeshia. Properties of fine–grained steels generated by displacive transformation. *Materials Science and Engineering A*, 481-482:36–39, 2008.

[BKC+08] Didier Blavette, Talaat Al Kassab, Emanuel Cadela, Alexander Mackel, François Vurpillot, Mathieu Gilbert, Oana Cojocaru,

and Bernard Deconihout. Laser-assisted atom probe tomography and nanosciences. *Int. J. of Materials Research*, 99(8):454–460, 2008.

[BM80] S. K. Banerji and J. E. Morral, editors. *Boron in Steel*, Warrendale, Pennsylvania, U.S.A., 1980. TMS AIME.

[Bra87] K. Braag. *Elektronenmikroskopische Untersuchungen nach Simulationsversuchen zur TM-Behandlung von Grossrohrstahlblechen*. PhD thesis, RWTH Aachen, 1987.

[BS93] H. K. D. H. Bhadeshia and L. E. Svensson. Model for boron effects in steel welds. In T. Zacharia, editor, *International Conference on Modelling and Control of Joining Processes*, pages 153–160. American Welding Society, 1993.

[BYMJ98] D.Q. Bai, S. Yue, T.M. Maccagno, and J.J. Jonas. Continuous cooling transformation temperatures determined by compression tests in low carbon bainitic grades. *Metallurgical and Materials Transactions A*, 29:989–1001, 1998.

[CCG+07] A. Cerezo, Peter H. Clifton, Mark J. Galtrey, Colin J. Humphreys, Thomas F. Kelly, David J. Larson, Sergio Lozano-Perez, Emmanuelle A. Marquis, Rachel A. Oliverd, Gang Shab, Keith Thompson, Mathijs Zandbergen, and Roger L. Alvis. Atom probe tomography today. *Materials Today*, 10(12):36–42, December 2007.

[CHGB00] A. J. Craven, K. He, L. A. J. Garvie, and T. N. Baker. Complex heterogeneous precipitation in titanium - niobium microalloyed al-killed hsla steels-i. (ti,nb)(c,n) particles. *Acta Materialia*, 48:3857–3868, 2000.

[CM07] F.G. Caballero and M. K. Miller. Solute trapped at defects during the displacive formation of bainitic ferrite. *Microscopy and Microanalysis*, 13(2), 2007.

[CMBS99] A.B. Cota, P.J. Modenesi, R. Barbosa, and D.B. Santos. Determination of cct diagrams by thermal analysis of an hsla bainitic steel submitted to thermomechanical treatment. *Scripta Materialia*, 40(2):165–169, 1999.

[CSMR07] J.M. Cairney, D.W. Saxey, D. McGrouther, and S.P. Ringer. Site-specific specimen preparation for atom probe tomography of grain boundaries. *Physica B*, 394:267–269, 2007.

[CWD+02] P. Cizek, B.P. Wynne, C.H.J. Davies, B.C. Muddle, and P.D. Hodgson. Effect of composition and austenite deformation on the transformation characteristics of low-carbon and ultralow-carbon microalloyed steels. *Metallurgical and Materials Transactions A*, 33:1331–1349, 2002.

[DGN82] J. Daigne, M. Guttmann, and J. P. Naylor. Mechanicl properties of martensite in heat resistant steels. *Materials Science and Engineering A*, 56:1–10, 1982.

[DP03] B. Dutta and E.J. Palmiere. Effect of prestrain and deformation temperature on the recrystallization behavior of steels microalloyed with niobium. *Metallurgical and Materials Transactions A*, 34:1237–1247, 2003.

[DSOR+02] N.H. Vand Dijk, W.G. Bouwman S.E. Offermann, M.Th. Rekveldt, J. Sietsma, S. Van der Zwaag, A. Bodin, and R.K. Heenan. High temperature sans experiments on nb(c,n) and mns

precipitates in hsla steel. *Metallurgical and Materials Transactions A*, 33:1883–1891, 2002.

[FC62] W. Fountain and J. Chipman. Soulubility and precipitation of boron nitride in fe-b alloys. *Transactions TMS-AIME*, 224:599–606, 1962.

[Fle63] R. L. Fleischer. Substitutional solution hardening. *Acta Metallurgica*, 11(3):203–209, March 1963.

[GDCR06] A. Ghosh, S. Das, S. Chatterjee, and P. Ramachandra Rao. Effect of cooling rate on structure and properties of an ultra-low carbon hsla-100 grade steel. *Materials Characterization*, 56:59–65, 2006.

[GMH+07] F. Grimpe, S. Meimeth, C. J. Heckmann, A. Liessem, and A. Gehrke. Development, production and application of heavy plates in grades up to x120. Technical report, Mannesmannroehren Muelheim, 2007.

[Got04] G. Gottstein. *Physical foundations of materials science*. Springer Verlag, 2004.

[Gou64] J. Gouzou. Analysis of the grain/size dependence of the lower yield stress in steel. *Acta Metallurgica*, 12(7):785–795, 1964.

[GT40] A. B. Greninger and A. R. Troiano. Crystallography of austenite decomposition. *Transactions AIMME*, 140:307–336, 1940.

[HBS82] D.J. Hall, H. K. D. H Bhadeshia, and W.M. Stobbs. The incomplete bainite reaction: Possible reasons for the apparent differences in tem and atom probe determination of the austenite carbon content. *Journal de Physique*, 42(12-C4):449–454, 1982.

[HJKP03] S.G. Hong, H.J. Jun, K.B. Kang, and C.G. Park. Evolution of precipitates in the nb–ti–v microalloyed hsla steels during reheating. *Scripta Materialia*, 48:1201–1206, 2003.

[HKP02] S.G. Hong, K.B. Kang, and C.G. Park. Strain-induced precipitation of nbc in nb and nb±ti microalloyed hsla steels. *Scripta Materialia*, 46:163–168, 2002.

[JKS+06] H.J. Jun, J.S. Kang, D.H. Seo, K.B. Kang, and C.G. Park. Effects of deformation and boron on microstructure and continuous cooling transformation in low carbon hsla steels. *Materials Science and Engineering A*, 422:157–162, 2006.

[KB62] H. Klemm and M. Beckert. *Handbuch der Metallographischen Ätzverfahren*. VEB Verlag für die Deutsche Grundstoffindustrie, Leipzig, Germany, 1962.

[KDMS92] Andreas Kern, Joachim Degenkolbe, Bruno Mosgen, and Udo Schriev. Computer modelling for the prediction of microstructure development and mechanical properties of hsla steel plates. *ISIJ International*, 32:387–394, 1992.

[Kie08] AMAT Uni Kiel. http://www.tf.uni-kiel.de/matwis/amat/def_en. webpage, July 2008.

[KKLK02] Y. M. Kim, S. K. Kim, Y. J. Lim, and N. J. Kim. Effect of microstructure on the yield ratio and low temperature toughness of linepipe steels. *ISIJ International*, 42(12):1571–1577, 2002.

[KL00] T. Kelly and D.J. Larson. Local electrode atom probes. *Materials Characterization*, 44:59–85, 2000.

[KM07] T. Kelly and M. K. Miller. Atom probe tomography. *Review of Scientific Instruments*, 78:1–19, 2007.

[Kru] F. Krumreich. http://www.microscopy.ethz.ch/tem_imaging.htm. webpage.

[KW63] A. S. Keh and S. Weissman. *Electron Microscopy and the Strength of Crystals*. Interscience, New York, 1963.

[Lan00] J. I. Langford. *Industrial Applications of X-Ray Diffraction*, volume 1, chapter 33, pages 751–773. Marcel Dekker Inc., New York, Basel, 2000.

[LC69] G. Langford and M. Cohen. Strain hardening of iron by severe plastic deformation. *Transactions ASM*, 62:623, 1969.

[LeP79] F. S. LePera. Improved etching technique for the determination of percent martensite in high-strength dual-phase steels. *Metallography*, 12:263–268, 1979.

[Lle93] D. T. Llewellyn. Boron in steels. *Iron and Steelmaking*, 20(5):338–343, 1993.

[Mel77] A. Melander. The influence of the finite size of inpenetrable obstacles on the critical resolved shear stress. *physica stata solidi a*, 43:223–230, 1977.

[Mil03] M.K. Miller. *Atom probe tomography: analysis at the atomic level*. Kluwer Academic / Plenum Publishers, New York, 2003.

[MRT+07] M. K. Miller, K. Russel, K. Thompson, R. Alvis, and D.J. Larson. Review of atom probe fib-based specimen preparation methods. *Microscopy and Microanalysis*, 13:428–436, 2007.

[MS89] M. K. Miller and G. D. W. Smith. *Atom Probe Analysis: Principles and Applications to Material Problems*. Materials Research Society, Pittsburgh PA, 1989.

[Mül60] E. W. Müller. The field ion microscope. *Advances in Electronics and Electron Physics*, 13:83–179, 1960.

[NPN08] R. Narayanasamy, N. L. Parthasarathi, and C. Sathiya Narayanan. Effect of microstructure on void nucleation and coalescence during forming of three different hsla steel sheets under different stress conditions. *Materials and Design*, Article in Press, 2008.

[OH92] Shuji Okaguchi and Tamotsu Hashimoto. Computer model for prediction of carbonitride precipitation during hot working in nb-ti bearing hsla steels. *ISIJ International*, 32(3):283–290, 1992.

[PBMB04] M. Peet, S. Babu, M. K. Miller, and H. K. D. H. Bhadeshia. Three-dimensional atom probe analysis of carbon distribution in low-temperature bainite. *Scripta Materialia*, 50:1277–1281, 2004.

[PCH01] E.V. Pereloma, B. R. Crawford, and P.D. Hodgson. Strain-induced precipitation behaviour in hot rolled strip steel. *Materials Science and Engineering A*, 299:27–37, 2001.

[Pet53] N. J. Petch. The cleavage strength of polycrystals. *Journal of the Iron and Steel Institute*, 174:25–28, 1953.

[Pet88] B. M. Peters. *Quantitative Zusammenhänge zwischen mechanischen Eigenschaften und metallkundlichen Größen unter besonderer Berücksichtigung der Großrohrstähle.* PhD thesis, RWTH Aachen, 1988.

[PI07] Kioumars Poorhaydari and Douglas G. Ivey. Application of carbon extraction replicas in grain-size measurements of high-

strength steels using tem. *Materials Characterization*, 58:544–554, 2007.

[PL07] J.S. Park and Y.K. Lee. Determination of nb(c, n) dissolution temperature by electrical resistivity measurement in a low-carbon microalloyed steel. *Scripta Materialia*, 56:225–228, 2007.

[PTJM06] E.V. Pereloma, I.B. Timokhina, J. J. Jonas, and M. K. Miller. Fine-scale microstructural investigations of warm rolled low-carbon steels with and without cr, p, and b additions. *Acta Materialia*, 54:4539–4551, 2006.

[SB96] E. Swallow and H.K.D.H Bhadeshia. High resolution observations of displacements caused by bainitic transformation. *Materials Science and Technology*, 12:121–125, 1996.

[SB98] S. Singh and H. K. D. H Bhadeshia. Estimation of bainite plate-thickness in low alloy steels. *Materials Science and Engineering A*, 245:72–79, 1998.

[Sch01] Jörg Schleiwies. *Nanoanalyse höchster Auflösung von metallischen Schichtsystemen*. PhD thesis, Universität Göttingen, 2001.

[SCM+07] D.W. Saxey, J.M. Cairney, D. McGrouther, T. Honma, and S.P. Ringer. Atom probe specimen fabrication methods using a dual fib/sem. *Ultramicroscopy*, 107:756–760, 2007.

[SF] L. Schutz and J. Freudenberger. Physikalische werkstoffeigenschaften, http://www.ifw-dresden.de/institutes/imw/lectures/lectures/pwe. Lecture script.

[SGM04] M. Shome, O.P. Gupta, and O.N. Mohanty. Effect of simulated thermal cycles on the microstructure of the heat-affected zone in hsla-80 and hsla-100 steel plates. *Metallurgical and Materials Transactions A*, 35:985–996, 2004.

[SRM+07] S. Shanmugam, N. K. Ramisetti, R. D. K. Misra, T. Mannering, D. Pandac, and S. Jansto. Effect of cooling rate on the microstructure and mechanical properties of nb-microalloyed steels. *Materials Science and Engineering A*, 460-461:335–343, 2007.

[SRM+08] S. Shanmugama, N. K. Ramisetti, R. D. K. Misra, J.Hartmann, and S. G. Jansto. Microstructure and high strength–toughness combination of a new 700mpa nb-microalloyed pipelinesteel. *Materials Science and Engineering A*, 478:26–37, 2008.

[SSB90] I. Stark, G. D. W. Smith, and H. K. D. H Bhadeshia. The distribution of substitutional alloying elements during the bainite transformation. *Metallurgical Transactions A*, 21(3):837–844, 1990.

[TB90] M. Takahashi and H. K. D. H. Bhadeshia. Model for transition from upper to lower bainite. *Materials Science and Technology*, 1990.

[TKYS07] Jun Takahashi, Kazuto Kawakami, Yukiko Yamaguchi, and Masaaki Sugiyama. Development of atom probe specimen preparation techniques for specific regions in steel materials. *Ultramicroscopy*, 107:744–749, 2007.

[TLL+07] K. Thompson, D. Lawrence, D.J. Larson, J.D. Olson, T. Kelly, and B. Gorman. In situ site-specific specimen preparation for atom probe tomography. *Ultramicroscopy*, 107:131–139, 2007.

[TM02] N. Tsuji and Y. Minamino. Strength and ductility of ultrafine grained aluminum and iron produced by arb and annealing. *Scripta Materialia*, 74:893, 2002.

[TP86] J.A. Todd and P.Li. Microstucture-mechanical property relationships in isothermally transformed vanadium steels. *Metallurgical Transactions A*, 17A:1191–1194, July 1986.

[WC96] David B. Williams and C. Barry Carter. *Transmission Electron Microscopy, a Textbook for Materials Science*. Plenum Press, New York, 1996.

[WG05] D. Wolde-Giorgis. *Korngrenzsegregation in Silber-Nickel und Kupfer-Wismut Legierungen*. PhD thesis, Universität Göttingen, 2005.

[WW86] P.L. Winter and R.L. Woodward. Effect of tempering temperature on the work-hardening rate of five hsla steels. *Metallurgical Transactions A*, 17:307–313, February 1986.

[XBM+03] Q. Xue, D. Benson, M.A. Meyers, V.F. Nesterenko, and E.A. Olevsky. Constitutive response of welded hsla 100 steel. *Materials Science and Engineering A*, pages 166–179, 2003.

[YB94] C. H. Young and H. K. D. H Bhadeshia. Strength of mixtures of bainite and martensite. *Materials Science and Technology*, 10:209–214, 1994.

List of Figures

List of Tables